

1 **Defining RNA oligonucleotides that reverse deleterious phase transitions of RNA-binding**
2 **proteins with prion-like domains**

3
4 Lin Guo^{1,2*^}, Jacob R. Mann^{3,4,5,6*}, Jocelyn C. Mauna^{3,4,5#}, Katie E. Copley^{1,7#}, Hejia Wang^{1#},
5 Jack D. Rubien^{1#}, Hana M. Odeh¹, JiaBei Lin¹, Bo Lim Lee¹, Laura Ganser⁸, Emma Robinson²,
6 Kevin M. Kim², Anastasia C. Murthy⁹, Tapas Paul⁸, Bede Portz¹, Amanda M. Gleixner^{3,4,5},
7 Zamia Diaz¹, Jenny L. Carey², Ashleigh Smirnov¹, George Padilla¹, Ellen Lavorando^{1,10},
8 Carolann Espy^{1,11}, Yulei Shang^{12,13}, Eric J. Huang^{12,13}, Alessandra Chesi¹⁴, Nicolas L. Fawzi⁹,
9 Sua Myong⁸, Christopher J. Donnelly^{3,4,5,6,15^}, and James Shorter^{1,7,10,11^§}.

10
11 ¹Department of Biochemistry and Biophysics, ⁷Neuroscience Graduate Group, ¹⁰Biochemistry
12 and Molecular Biophysics Graduate Group, ¹¹Pharmacology Graduate Group, ¹⁴Department of
13 Pathology and Laboratory Medicine, Perelman School of Medicine, University of Pennsylvania,
14 Philadelphia, PA 19104. U.S.A.

15
16 ²Department of Biochemistry and Molecular Biology, Thomas Jefferson University,
17 Philadelphia, PA 19107. U.S.A.

18
19 ³Department of Neurobiology, ⁴Live Like Lou Center for ALS Research, ⁵Center for
20 Neuroscience at the University of Pittsburgh, ⁶Center for Protein Conformational Diseases,
21 ¹⁵Pittsburgh Institute for Neurodegeneration, University of Pittsburgh School of Medicine,
22 Pittsburgh, PA 15213. U.S.A.

23
24 ⁸Department of Biophysics, Johns Hopkins University, Baltimore, MD 21218. U.S.A.

25
26 ⁹Department of Molecular Biology, Cell Biology, and Biochemistry, Brown University,
27 Providence, RI 02912, U.S.A.

28
29 ¹²Eli and Edythe Broad Center of Regeneration Medicine and Stem Cell Research, ¹³Department
30 of Pathology, University of California, San Francisco, CA 94143. U.S.A.

31
32
33 *Co-first authors. #Co-second authors.

34
35 ^Co-corresponding authors: lin.guo@jefferson.edu
36 cjdon25@pitt.edu
37 jshorter@pennmedicine.upenn.edu

38
39 §Lead contact
40

41 **Summary**

42 RNA-binding proteins with prion-like domains, such as FUS and TDP-43, condense into
43 functional liquids, which can transform into pathological fibrils that underpin fatal
44 neurodegenerative disorders, including amyotrophic lateral sclerosis (ALS)/frontotemporal
45 dementia (FTD). Here, we define short RNAs (24-48 nucleotides) that prevent FUS fibrillization
46 by promoting liquid phases, and distinct short RNAs that prevent and, remarkably, reverse FUS
47 condensation and fibrillization. These activities require interactions with multiple RNA-binding
48 domains of FUS and are encoded by RNA sequence, length, and structure. Importantly, we
49 define a short RNA that dissolves aberrant cytoplasmic FUS condensates, restores nuclear FUS,
50 and mitigates FUS proteotoxicity in optogenetic models and human motor neurons. Another
51 short RNA dissolves aberrant cytoplasmic TDP-43 condensates, restores nuclear TDP-43, and
52 mitigates TDP-43 proteotoxicity. Since short RNAs can be effectively delivered to the human
53 brain, these oligonucleotides could have therapeutic utility for ALS/FTD and related disorders.

54

55 **Introduction**

56 There are no effective therapeutics for several devastating neurodegenerative disorders,
57 including amyotrophic lateral sclerosis (ALS) and frontotemporal dementia (FTD). A common
58 feature of these disorders is the cytoplasmic mislocalization and aggregation of nuclear RNA-
59 binding proteins (RBPs) with prion-like domains (PrLDs), such as TDP-43 or FUS, in
60 degenerating neurons.¹⁻⁷ This cytoplasmic aggregation is driven by PrLDs, which are distinctive
61 low-complexity domains with an amino-acid composition enriched for uncharged polar residues
62 (especially glutamine, asparagine, tyrosine, and serine) and glycine similar to yeast prion
63 domains.¹ Yeast prion domains enable various yeast proteins (e.g. Sup35 and Ure2) to form
64 prions.¹ In the context of TDP-43 and FUS, the PrLD renders these RBPs intrinsically
65 aggregation prone and enables the formation of self-templating, amyloid-like fibrils.^{1,3,8-10}
66 However, the PrLD also enables TDP-43 and FUS to undergo phase separation (PS), where
67 TDP-43 and FUS can spontaneously condense from dispersed states in solution to a separated
68 liquid phase.¹ PS enables TDP-43 and FUS to function in membraneless organelles inside the
69 nucleus.^{1,11-14} TDP-43 and FUS can also undergo PS in the cytoplasm during recruitment to
70 stress granules and during formation of alternative cytoplasmic condensates.^{1,11,12,15,16} If TDP-43
71 or FUS dwell in liquid states for too long, especially in the cytoplasm, then they can transition
72 into amyloid-like fibrils.^{11,15,16} This switch from a liquid to pathological fibrils in the context of
73 disease is termed an aberrant phase transition, which can be accelerated by ALS-linked
74 mutations in TDP-43 or FUS.^{11,15} A deleterious event in ALS/FTD occurs when TDP-43 or FUS
75 become depleted from the nucleus and trapped in cytoplasmic aggregates.^{1,12,15}

76
77 A key therapeutic innovation for ALS/FTD would be to develop agents that reverse the aberrant
78 cytoplasmic aggregation of TDP-43 and FUS, and return these proteins to native form and
79 nuclear function.¹ Such agents would simultaneously eliminate two malicious problems
80 associated with cytoplasmic TDP-43 or FUS aggregation: **(1)** the toxic gain of function of
81 cytoplasmic aggregated TDP-43 or FUS conformers; and **(2)** the loss of cytoplasmic and nuclear
82 function of soluble TDP-43 or FUS due to sequestration in cytoplasmic aggregates. These two
83 issues likely synergize in the etiology of various forms of ALS/FTD.¹

84

85 A therapeutic disaggregase that dissolves cytoplasmic aggregates and restores TDP-43 or FUS
86 back to the nucleus could eradicate these two deleterious phenotypes simultaneously.¹⁷
87 Previously, we have established that engineered versions of yeast Hsp104 and endogenous
88 human nuclear-import receptors can reverse TDP-43 or FUS aggregation and restore the RBPs to
89 the nucleus.^{8,18,19} However, despite exciting advances in AAV technology,²⁰ delivering these
90 agents into the degenerating neurons of ALS/FTD patients remains a significant challenge.

91
92 Here, we define more deliverable therapeutic agents: short RNA oligonucleotides (24-48
93 nucleotides [nts]) that antagonize FUS fibrillization. We uncover two distinct classes of RNA
94 inhibitor. Weak RNA inhibitors prevent FUS fibrillization by promoting liquid states. By
95 contrast, strong RNA inhibitors prevent and reverse FUS condensation and fibrillization. These
96 activities require interactions with multiple RNA-binding domains of FUS and are encoded by
97 RNA sequence, length, and structure. Importantly, we define a short RNA (25nts) that dissolves
98 aberrant FUS condensates, restores FUS to the nucleus, and mitigates FUS proteotoxicity in
99 optogenetic models and in human motor neurons. A distinct short RNA oligonucleotide (34nts)
100 can prevent and reverse TDP-43 PS and fibrillization by engaging the TDP-43 RNA-recognition
101 motifs (RRMs). This RNA dissolves aberrant cytoplasmic TDP-43 condensates, restores TDP-43
102 to the nucleus, and mitigates TDP-43 toxicity. Thus, we establish an important concept: specific
103 short RNAs can prevent *and* reverse aberrant phase transitions of TDP-43 and FUS to restore
104 nuclear localization and mitigate neurotoxicity. Since short RNA oligonucleotides can be readily
105 delivered to the human brain,²¹ these agents could have therapeutic utility for ALS/FTD and
106 related disorders.

107

108

109 **Results**

110 **Identification of short RNAs that strongly or weakly antagonize FUS assembly**

111 First, we aimed to identify short specific RNAs (24-48nts) that antagonize aberrant FUS
112 assembly. We sought RNAs of this length as they can be readily delivered to the CNS of patients
113 akin to antisense oligonucleotides (ASOs), which are typically 12-30nts.²² While extracting
114 recombinant GST-FUS from *E. coli*, we found that purified GST-FUS was bound to RNA
115 (Figure S1A). Specific removal of the GST tag with TEV protease elicits rapid assembly of
116 tangled FUS fibrils within an hour.^{8,10} By contrast, GST-FUS remains soluble in the absence of
117 TEV cleavage over this timeframe.¹⁰ Strikingly, treating GST-FUS with RNase A to remove
118 RNA strongly increased turbidity in the absence of TEV cleavage (Figure S1B). Hence, RNA
119 promotes GST-FUS solubility.

120

121 We sought to identify enriched RNA motifs in this FUS-bound RNA population as they might
122 antagonize aberrant FUS assembly. The A_{260}/A_{280} ratio of the GST-FUS purified from *E. coli*
123 was ~ 1.8 , indicating $\sim 38\%$ (w/w) nucleic acid in the sample.²³ RNA extraction followed by
124 electrophoresis revealed a population of RNAs with a size range of ~ 50 -100nts. From this RNA
125 population, a cDNA library was constructed and sequenced. We identified 42 enriched motifs
126 between 8-12nts in our library (Table S1). 14 RNA motifs were selected for further testing based
127 on their enrichment and sequence diversity (Table S1, S2). RNA oligonucleotides (oligos)
128 containing 2 or 4 repeats of individual enriched motifs were synthesized and assessed for their
129 ability to inhibit FUS fibrillization (Figure 1A; Table S2). An RNA oligo (RNA C2) that does
130 not bind FUS effectively was used as a negative control (Table S2).²⁴ Indeed, RNA C2 had little
131 effect on FUS fibrillization (Figure 1B). Remarkably, RNA S2 (containing 4 repeats of
132 GAGGUGGCUAUG) diminished FUS fibrillization (Figure 1B). Thus, a short RNA bearing
133 specific motifs that engage FUS can abrogate FUS fibrillization.

134

135 We found seven additional RNAs (RNA W1, W4-W9) that increased the lag time and reduced
136 the extent of FUS assembly more than RNA C2 (Figure S1C, D, Table S2). By contrast, six
137 RNAs (RNA N1-N6) based on enriched motifs from our library were ineffective at inhibiting
138 FUS assembly and did not show a significant difference compared to RNA C2 (Figure S1E, F,

139 Table S2). Thus, the presence of RNA in general is not sufficient to inhibit FUS fibrillization.
140 Rather, specific RNAs likely have different abilities to antagonize FUS fibrillization.

141
142 We next tested whether RNAs that have been reported to bind FUS might also antagonize FUS
143 fibrillization. Eight short RNA sequences that bind FUS (RNA S1, S3-S8, and W3) as well as a
144 (UG)₆-containing RNA (RNA W2) that binds TDP-43 were tested (Table S2).²⁵⁻²⁸ Within this
145 group of RNAs, seven oligos (RNA S1, S3-S8) strongly inhibited FUS fibrillization (Figure 1B).
146 By contrast, RNA W2 and the GGUG-containing RNA (RNA W3) mildly inhibited FUS
147 assembly (Figure S1C, D). Based on these findings, we classified RNAs into three groups: strong
148 inhibitors (RNA S1-S8) that reduced turbidity by more than 90%, weak inhibitors (RNA W1-
149 W9) that reduced turbidity by less than 90% but significantly compared to control RNA C2, and
150 non-effective RNAs (RNA N1-N6) that had no effect beyond control RNA C2 (Figure 1B, S1C-
151 F, Table S2).

152
153 **Strong RNA inhibitors prevent FUS PS and fibrillization, whereas weak RNA inhibitors**
154 **allow FUS PS but prevent fibrillization**

155 Next, we assessed how strong and weak RNA inhibitors affected FUS assembly via
156 sedimentation analysis. Strong RNA inhibitors (RNA S1-S3) promoted accumulation of FUS in
157 the soluble fraction, whereas a weak RNA inhibitor (RNA W1) did not (Figure S1G). Thus,
158 weak RNA inhibitors may allow FUS to assemble into structures that display reduced turbidity
159 compared to large tangles of FUS fibrils. FUS can form liquid droplets that later convert into
160 fibrils.^{11,29} Thus, we wondered whether strong and weak RNA inhibitors might antagonize
161 different stages of this process. We utilized electron microscopy (EM) to visualize FUS
162 assemblies formed in the presence or absence of strong and weak RNA inhibitors. In the absence
163 of RNA, FUS forms large aggregates comprised of tangled fibrils (Figure 1C).^{8,10} FUS
164 fibrillization was unaffected by the negative control RNA C2 (Figure 1C). By contrast, strong
165 inhibitors (RNA S1-S5) greatly reduced the formation of any FUS assemblies (Figure 1C and
166 S1H). Interestingly, a weak RNA inhibitor, RNA W1, inhibited the formation of large tangles of
167 FUS fibrils, but allowed the formation of numerous spherical structures, indicative of phase-
168 separated condensates (Figure 1C). Thus, weak RNA inhibitors may prevent FUS fibrillization
169 by promoting liquid phases.

170

171 To explore this possibility further, we employed Differential Interference Contrast (DIC)
172 microscopy to more closely study the formation and dynamics of FUS droplets in the presence or
173 absence of strong and weak RNA inhibitors. If we do not remove the GST tag, then GST-FUS is
174 initially soluble, but slowly condenses into liquid droplets after several hours.⁸ Indeed, without
175 addition of RNA or in the presence of RNA C2, GST-FUS formed dynamic droplets that
176 exhibited classic liquid-like behavior such as fusion and surface wetting (Figure 1D).^{8,11} Strong
177 RNA inhibitors abolished formation of FUS droplets (Figure 1D and Figure S1I), whereas weak
178 RNA inhibitors had no effect on FUS droplet formation (Figure 1D and Figure S1I, RNA W1
179 and W2). Thus, strong RNA inhibitors prevent FUS PS and fibrillization, whereas weak RNA
180 inhibitors allow FUS PS but prevent fibrillization.

181

182 **Strong RNA inhibitors reverse FUS PS and fibrillization**

183 Next, we assessed whether short RNAs could reverse the formation of preformed FUS droplets.
184 The weak RNA inhibitors, RNA W1-W4, and control RNA C2 had no effect on preformed FUS
185 droplets (Figure 1E, Movie S1). Remarkably, strong RNA inhibitors (RNA S1-S3) rapidly
186 dissolved preformed FUS droplets (Figure 1E, Movie S2-S4). Thus, strong RNA inhibitors can
187 reverse FUS PS, whereas weak RNA inhibitors cannot.

188

189 We next tested whether RNA inhibitors could disassemble preformed FUS fibrils (Figure 1F).
190 Addition of solvent or RNA C2 had little effect on FUS fibrils (Figure 1F, G). By contrast,
191 strong RNA inhibitors rapidly disassembled preformed FUS fibrils within 20 minutes (Figure
192 1F). Among the strong RNA inhibitors, RNA S2 disassembled FUS fibrils most rapidly, whereas
193 RNA S1 showed the most complete disaggregation (Figure 1F). Thus, remarkably, strong RNA
194 inhibitors can rapidly disassemble preformed FUS fibrils.

195

196 Interestingly, when other strong RNA inhibitors (RNA S3-S8) were added to FUS fibrils, we
197 observed an initial rapid disassembly followed by slow recovery of turbidity upon further
198 incubation (Figure 1F). EM revealed that 20 minutes after addition of RNAs, when turbidity is at
199 the lowest point, all strong RNA inhibitors effectively disassembled FUS fibrils (Figure 1G and
200 S2A). However, 2 hours after addition of RNAs, when turbidity increased again, dense FUS

201 condensates were observed for samples treated with RNA S3, RNA S4, and RNA S5 (Figure 1G,
202 S2A). These dense FUS condensates exhibited porous architecture resembling a hydrogel (Figure
203 S2A).⁸ DIC microscopy revealed that these FUS condensates were spherical but did not fuse,
204 indicating a gel-like phase (Figure S2B). Thus, a subset of strong RNA inhibitors disassembles
205 FUS fibrils initially, but FUS then transforms into dense gel-like condensates. By contrast, RNA
206 S1 and S2 are unusual in that they effectively dissolve FUS fibrils and do not transform FUS into
207 another condensate.

208
209 Most weak RNA inhibitors (i.e., RNA W1, W4-W9) had no effect on preformed FUS fibrils
210 beyond the negative control RNA C2 (Figure S2C). By contrast, RNA W2 and W3 initially
211 reduced turbidity, but turbidity then returned to levels observed with RNA C2, indicating a lack
212 of a sustained effect (Figure S2C). The non-effective RNAs (Table S2) did not have any effect
213 on preformed FUS fibrils beyond RNA C2 (Figure S2D). Thus, the disassembly of FUS fibrils is
214 due to binding to specific RNA sequences. Our findings suggest that RNA S1 and S2 possess an
215 unusual ability to dissolve FUS liquids and fibrils. RNA S1 is a natural FUS-binding RNA
216 (CUAGGAUGGAGGUGGGGAAUGGUAC) found in the 3'UTR of the BDNF gene.²⁶ By
217 contrast, RNA S2 is a synthetic RNA comprised of four repeats of an RNA motif
218 (GAGGUGGCUAUG) found to engage FUS during purification from *E. coli*. Thus, both native
219 and designed RNA sequences that engage FUS can reverse FUS PS and fibrillization.

220

221 **RNA S1 prevents and reverses assembly of ALS-linked FUS mutants.**

222 Mutations in FUS are an established cause of ALS.³⁰ Thus, we next tested whether RNA S1
223 could also antagonize assembly of ALS-linked FUS variants, including FUS^{P525L}, FUS^{R521G},
224 FUS^{R244C}, and FUS^{R216C}. Importantly, RNA S1 inhibited (Figure S2E) and reversed fibrillization
225 of these disease-linked FUS variants (Figure S2F-I). Thus, RNA S1 can prevent and reverse
226 fibrillization of FUS as well as several ALS-linked FUS variants.

227

228 **RNA length, sequence, and structure determine ability to antagonize FUS fibrillization**

229 We next investigated what features determined whether an RNA was a strong or weak inhibitor.
230 Strong RNA inhibitors were typically longer than weak inhibitors (Table S2, Figure S2J). Most
231 weak RNA inhibitors or non-effective RNAs were 24-28nts, whereas most strong inhibitors were

232 39-48nts (Figure S2J, Table S2). The two exceptions were RNA S1 and S7 (Table S2), which
233 were 24-25nts (Table S2). To examine how RNA length affected the ability of RNA oligos to
234 antagonize FUS assembly, we selected a strong inhibitor RNA S2, which is 4 repeats of the
235 enriched motif GAGGUGGCUAUG, and synthesized RNA S2/2, which contains 2 repeats of the
236 same enriched motif (Table S2, Figure 2A). Shortening the length of strong inhibitor RNA S2
237 reduced its ability to prevent FUS assembly (Figure 2B). This effect was more pronounced for
238 reversing FUS fibrillization. Thus, RNA S2 effectively reversed FUS fibrillization, whereas
239 RNA S2/2 had no effect beyond the negative control RNA C2 (Figure 2C). Thus, increasing
240 RNA length from 24 to 48nts can enable more effective prevention and reversal of FUS
241 fibrillization.

242
243 To further determine the effect of RNA length on activity, we next focused on potentiating the
244 weak inhibitor RNA W1, which contains two repeats of enriched motif UCAGAGACAUCA.
245 We synthesized RNA W1*2, which doubles the length of RNA W1 and contains 4 repeats of the
246 enriched motif (Figure 2D). Doubling the length of RNA W1 increased its ability to prevent FUS
247 assembly (Figure 2E). RNA W1*2 was also more effective than RNA W1 in reversing FUS
248 fibrillization in the initial 20min of the reaction (Figure 2F), but turbidity increased at later times
249 (Figure 2F). Nonetheless, increasing RNA length from 24 to 48nts can enable more effective
250 prevention and reversal of FUS assembly. Indeed, strong inhibitors were typically longer than
251 weak inhibitors (Figure S2J).

252
253 RNA S2 and RNA W1*2 are the same length (48nt), but RNA S2 prevents and reverses FUS
254 assembly more effectively than RNA W1*2 (Figure 2B, E). RNA S2 contains four consensus
255 FUS-binding motifs, i.e., GGUG,²⁴ whereas these FUS-binding motifs are absent from RNA
256 W1*2 (Figure 2A). Thus, the precise RNA sequence is also important for activity. Strong RNA
257 inhibitors tend to have more GGU and GG sequences than weak RNA inhibitors (Figure S2K,
258 Table S2). Notably, the two strongest inhibitors RNA S1 and S2 have AUGGAGGUGG in their
259 sequence. To further explore how sensitive sequence requirements might be, we introduced a
260 single A to U mutation in RNA S2/2 (to yield RNA S2/2 (A-U)), which creates overlapping
261 GUGG FUS-binding motifs (Table S2, Figure 2A).²⁸ This single mutation reduced the ability of
262 RNA S2/2 (A-U) to prevent FUS assembly (Figure 2A, B). RNA S2/2 and RNA S2/2 (A-U)

263 have similar predicted secondary structures (Table S2). Thus, specific RNA sequences can
264 encode more effective inhibition of FUS fibrillization.

265

266 We next considered whether RNA structure might also contribute to preventing and reversing
267 FUS assembly. Thus, we employed single molecule Förster Resonance Energy Transfer
268 (smFRET) to study the conformation of RNA and the interaction between FUS and RNA.³¹
269 Here, we examined an unstructured RNA (U50) and a strong RNA inhibitor with similar length
270 (RNA S2). RNA U50 is predicted to be unstructured, whereas RNA S2 is predicted to adopt a
271 stem-loop structure with folding energy of -16.40 kcal/mol (Figure 2G). Unstructured RNA U50
272 was a weak RNA inhibitor that reduced FUS assembly (Figure 2H) but did not affect FUS PS
273 (Figure 2I). For smFRET, RNA U50 or RNA S2 was immobilized onto a PEG-passivated quartz
274 slide via an 18-bp duplex and biotin-neutravidin interaction (Figure 2J, K).^{31,32} Cy3 and Cy5
275 were attached to either end of each RNA to report on the conformational status of RNA and the
276 change induced by FUS binding (Figure 2J, K). The FRET value for U50 in the absence of FUS
277 is ~0.2, consistent with an unstructured RNA.³¹ Conversely, the FRET value for RNA S2 is ~0.8,
278 indicating a stable, folded RNA conformation (Figure 2K), consistent with MFold predictions.

279

280 Addition of FUS to the RNA resulted in FRET changes which report on how FUS binding
281 affects RNA conformation (Figure 2J, K). For U50, addition of low FUS concentration (5nM)
282 immediately shifted the low FRET (~0.2) to a single high FRET peak (~0.8) with single
283 molecule traces displaying a stable high FRET signal (Figure 2J).³¹ Thus, FUS induces a tight
284 compaction of the long, unstructured U50 RNA (Figure 2J). As FUS concentration increased
285 (50 and 500nM), the high FRET population diminished, and a broad mid FRET peak (~0.5)
286 emerged with smFRET traces showing increased fluctuations (Figure 2J).³¹ The mid FRET peak
287 indicates an extended RNA structure, which allows dynamic interaction between FUS multimers
288 and a single RNA (Figure 2J).³¹ This finding is consistent with U50 allowing FUS droplets to
289 form (Figure 2I). Thus, the highly dynamic interaction between U50 and FUS (50 and 500nM) is
290 consistent with the dynamic nature of FUS liquid droplets.

291

292 By contrast, addition of FUS to RNA S2 did not yield dynamic FRET fluctuations (Figure 2K),
293 indicating formation of a static complex. FUS binding to RNA S2 induced a lower (~0.6) FRET

294 population, suggesting that FUS partially unfolds RNA S2 upon binding (Figure 2K). The FUS-
295 bound peak is wider than the free RNA peak, indicating that the conformation of RNA S2 is
296 more heterogeneous when bound to FUS (Figure 2K). Nonetheless, unlike U50, the structured
297 nature of RNA S2 restricted FUS to a static complex that precluded the formation of dynamic
298 FUS multimers (Figure 2K, right panel). Thus, RNA S2 eliminates FUS PS and fibrillization by
299 restricting FUS to a static complex.

300

301 **Strong RNA inhibitors engage the FUS RRM to antagonize FUS assembly**

302 We next assessed how the individual RNA-binding domains of FUS enable short RNAs to exert
303 their effects. The FUS RRM, Zinc finger domain, and RGG domains can all contribute to RNA
304 binding.³³ We selected the three RNAs with the strongest *in vitro* activities (i.e., RNA S1, RNA
305 S2, and RNA S3) and one weak inhibitor (RNA W1) for further analysis. Strong RNA inhibitors
306 bind to FUS tightly (RNA S1: $K_D \sim 40.8$ nM; RNA S2: $K_D \sim 105$ nM; RNA S3: $K_D \sim 102$ nM) (Figure
307 3A), whereas RNA W1 binds to FUS, but with a K_D greater than 3μ M (value could not be
308 determined via fluorescence anisotropy). Thus, tighter binding may enable the activity of strong
309 RNA inhibitors.

310

311 To assess the contribution of the FUS RRM to binding RNA S1, S2, and S3, we employed
312 FUS_{4F-L} where four conserved phenylalanines (F305, F341, F359, and F368) in the RRM are
313 mutated to leucine, which greatly reduces RNA binding.³⁴ FUS_{4F-L} exhibited ~ 2.8 - 7.3 -fold
314 reduced binding affinity to strong RNA inhibitors (RNA S1: $K_D \sim 113$ nM; RNA S2: $K_D \sim 769$ nM;
315 RNA S3: $K_D \sim 297$ nM) (Figure 3A). Thus, FUS_{4F-L} can still bind RNA S1, S2, and S3, but with
316 reduced affinity, indicating an important role for the FUS RRM in engaging these RNAs.

317

318 We next assessed whether strong (S1-S3) and weak (W1-W3) RNA inhibitors could prevent and
319 reverse FUS_{4F-L} fibrillization. FUS_{4F-L} formed tangled fibrils, but these assembled more slowly
320 than FUS (Figure 1B, 3B, S3A). None of the short RNAs tested here could prevent FUS_{4F-L}
321 fibrillization (Figure 3B, S3A, B). Likewise, RNAs S1-S3 and W1-W3 were ineffective at
322 reversing FUS_{4F-L} fibrillization (Figure 3C, S3C). Although turbidity was reduced in the first
323 20min by RNAs S1-S3, this effect was not sustained, and turbidity returned to initial levels

324 (Figure 3C). Thus, strong RNA inhibitors must engage the FUS RRM to effectively prevent and
325 reverse FUS fibrillization.

326

327 FUS_{4F-L} fibrillization could not be antagonized by RNAs S1 or S2. However, these RNAs could
328 still bind to FUS_{4F-L}, albeit with reduced affinity. To assess which other FUS domains might
329 engage these RNAs, we used nuclear magnetic resonance (NMR) spectroscopy. Since the FUS
330 PrLD does not bind to RNA,³⁵ we employed FUS₂₆₉₋₄₅₄, which lacks the N-terminal PrLD, but
331 contains the RRM (residues 285-370), an RGG domain (residues 371-421), and the Zinc Finger
332 (ZnF) domain (residues 422-453). FUS₂₆₉₋₄₅₄ binds various RNAs robustly.³³ We conducted 2D
333 ¹H,¹⁵N-HSQC experiments in the presence or absence of RNA S1, S2, W1, or C2. Addition of
334 each RNA caused NMR chemical shifts in the RRM, RGG, and ZnF regions of FUS, consistent
335 with RNA binding to all three domains (Figure S3D). Extensive NMR resonance broadening and
336 low peak intensity in the spectra of FUS₂₆₉₋₄₅₄ is observed in the presence of RNA S1 or S2
337 (Figure S3D). This effect is much more pronounced for RNA S1 and S2 than for RNA W1 and
338 C2, particularly in the resonances of residues 290-360, which map to the RRM (Figure S3D).
339 These observations suggest that FUS complexed with RNA S1 or RNA S2 exchange
340 conformations (i.e., RNA binding/unbinding k_{ex}) on the intermediate NMR chemical shift
341 timescale or form higher order complexes. Either of these possibilities is consistent with higher
342 affinities of RNA S1 and S2 for the RNA-binding domains than RNA W1 and C2. Thus, while
343 the overall binding sites between FUS and the RNAs are similar, the affinities for the RNA-
344 binding domains are likely different. Specifically, RNA S1 and S2 engage with higher affinity.

345

346 **Weak RNA inhibitors engage the FUS ZnF to antagonize FUS assembly**

347 Since the RNA inhibitors engage multiple FUS domains (Figure S3D), we next investigated how
348 RNA interactions with the ZnF domain might contribute to their ability to antagonize FUS
349 assembly. Thus, we generated a FUS^{C428A:C433A:C444A:C447A} (FUS_{4C-A}) mutant, which contains four
350 cysteine to alanine substitutions that disrupt the C4-type Zinc coordination scheme, which enable
351 RNA binding (Figure 3A, D).³⁶ FUS_{4C-A} formed fibrils with similar kinetics to FUS (Figure 1B,
352 3D, E). Strong RNA inhibitors S1-S3 effectively prevented and reversed formation of FUS_{4C-A}
353 fibrils (Figure 3D, S3E). Thus, disrupting the ZnF domain has little effect on the activity of
354 strong RNA inhibitors. Consistent with this result, the binding affinities of strong RNA inhibitors

355 to FUS_{4C-A} were not significantly different from their binding affinities to FUS (RNA S1:
356 $K_D \sim 25\text{nM}$; RNA S2: $K_D \sim 136\text{nM}$; RNA S3: $K_D \sim 59\text{nM}$) (Figure 3A). In striking contrast, weak
357 RNA inhibitors could neither prevent nor reverse FUS_{4C-A} assembly (Figure 3E and S3F). Thus,
358 the ZnF domain may play a critical role in enabling weak RNA inhibitors to antagonize FUS
359 assembly but is less important for strong RNA inhibitors.

360

361 **FUS_{371X} is refractory to RNA inhibitors**

362 In addition to the RRM and ZnF regions, our NMR studies revealed that a FUS RGG domain
363 also interacted with various RNA inhibitors (Figure S3D). To assess how these interactions
364 might contribute to RNA inhibitor activity, we created a FUS construct consisting of the N-
365 terminal PrLD and RRM (FUS_{371X}). As expected, after deleting the RGG domains that enable
366 rapid FUS assembly,^{10,37} FUS_{371X} formed fibrils much more slowly than FUS, taking up to 24
367 hours to assemble (Figure S3G). Deletion of the C-terminal RGG domains and ZnF affected
368 binding of RNA inhibitors to varying extents (RNA S1: $K_D \sim 107\text{nM}$; RNA S2: K_D could not be
369 determined; RNA S3: $K_D \sim 124\text{nM}$) (Figure 3A). For example, the most pronounced change was
370 for RNA S2, where we could not saturate binding to determine a K_D , though RNA binding still
371 occurred (Figure 3A). The K_D of RNA S1 increased from $\sim 41\text{nM}$ for FUS to 107nM for FUS_{371X}.
372 By contrast, the K_D of RNA S3 for FUS and FUS_{371X} were similar.²⁷ Importantly, FUS_{371X}
373 fibrillization could not be inhibited or reversed with RNA S1, S2, or W1 (Figure 3F, G). By
374 contrast, RNA S3 could inhibit FUS_{371X} assembly by $\sim 50\%$ but was unable to reverse FUS_{371X}
375 fibrillization (Figure 3F, G). These findings suggest that the C-terminal RNA-binding domains of
376 FUS (RGG domains and ZnF) enable strong RNA inhibitors to exert their maximal effects in
377 preventing and reversing FUS fibrillization.

378

379 **Weak RNA inhibitor W1 displays greater co-operativity than strong RNA inhibitors S1-S3**

380 Next, we assessed the dose dependence of inhibition of FUS assembly by RNA S1, S2, S3, and
381 W1. As expected, the strong RNAs were more effective inhibitors with half maximal inhibitory
382 concentrations (IC_{50}) ranging from $\sim 3\text{-}8\mu\text{M}$, whereas the IC_{50} of RNA W1 was $\sim 65\mu\text{M}$ (Figure
383 3H-K). If RNA binding to multiple FUS domains were required to reduce assembly, one would
384 expect to observe cooperativity in RNA inhibition. Indeed, both strong and weak RNA inhibitors
385 exhibited cooperativity with Hill coefficients (h) ranging from ~ -1.3 to ~ -4.1 (Figure 3H-K).

386 Strong RNA inhibitors S1, S2, and S3 had less steep dose-response slopes with h values from ~-
387 1.3 to ~-2, whereas the weak RNA inhibitor W1 had a steeper dose-response slope with an h
388 value of ~-4.1. Thus, weak RNA inhibitor W1 displays greater cooperativity than strong RNA
389 inhibitors S1-S3, which may reflect the requirement for a functional RRM and ZnF domain for
390 RNA W1 to be effective. Overall, our findings suggest that short RNAs must engage multiple
391 RNA-binding domains of FUS for maximal inhibition of assembly.

392

393 **The FUS RRM and ZnF domains cooperate to maintain FUS solubility in human cells**

394 Injecting RNase into the nucleus causes FUS to aggregate, indicating that endogenous RNAs
395 promote FUS solubility.³⁸ However, whether specific, short RNAs can be introduced as agents to
396 prevent and reverse aberrant phase separation of FUS in cells is unclear. To investigate how the
397 RNA-binding domains of FUS might contribute to FUS solubility in human cells, we established
398 an optogenetic system to control FUS phase separation in response to blue light. Thus, we
399 adapted the Corelet system which has been used to map intracellular phase behavior of the FUS
400 PrLD and other intrinsically disordered regions (IDRs) in response to blue light.³⁹ Corelet is a
401 two-module system that relies on the light-based dimerization between an improved light-
402 induced dimer (iLID) domain on a ferritin heavy chain (FTH1) protein core (which forms
403 24mers) and an SspB domain on the molecule of interest, in this case FUS.³⁹ We first generated
404 FUS constructs (amino acids 1-453) containing wild-type RNA-binding regions, mutated RRM
405 (4FL), mutated ZnF domain (4CA), or double RRM and ZnF mutants (4FL/4CA) with C-
406 terminal SspB peptide tags (Figure 4A). We omitted the C-terminal RGG domain and PY-NLS
407 to prevent spontaneous phase separation of full-length FUS proteins with mutated RNA-binding
408 regions,³⁴ and also to reduce interaction with the nuclear-import receptor, Karyopherin- β 2, which
409 can prevent FUS phase separation.^{8,40-43}

410

411 We exposed cells co-expressing FUS-SspB constructs and photo-activatable seeds (iLID-EGFP-
412 FTH1)³⁹ to acute (30 second) blue light activation sequences and assessed FUS condensate
413 formation and dissolution (Figure 4B). Interestingly, mutations within the RRM region (4FL, red
414 trace) led to enhanced formation of light-induced FUS-SspB condensates compared to wild-type
415 (WT) FUS₁₋₄₅₃ (black trace), whereas mutations within the ZnF domain (4CA, blue trace) only
416 mildly increased light-induced phase separation (LIPS) (Figure 4B, C). However, when ZnF

417 mutations were combined with RRM mutations (4FL/4CA, purple trace), a further enhancement
418 of FUS-SspB condensate formation was observed when compared to either RRM or ZnF
419 mutations alone (Figure 4B, C). Thus, the FUS RRM and ZnF cooperate to prevent FUS
420 condensation, with the RRM playing a larger role than the ZnF.

421

422 A similar pattern was observed when we next examined LIPS as a function of FUS-SspB
423 expression level (Figure 4D, E). Here, ZnF mutations (4CA) slightly reduced the threshold
424 protein concentration (C_{thresh}) required for condensate formation, whereas RRM (4FL) and dual
425 RRM and ZnF (4FL/4CA) mutations greatly reduced C_{thresh} (Figure 4D, E). Following light
426 removal, RRM and dual RRM and ZnF mutations caused decelerated dissolution of light-
427 induced condensates compared to WT and ZnF-only mutants (Figure 4F), which indicates
428 increased stability of these condensates. Together, these results suggest that endogenous RNA
429 contacts with the FUS RRM play a critical role in preventing aberrant phase transitions within
430 the intracellular milieu, but the FUS ZnF domain also contributes.

431

432 **An optogenetic model of FUS proteinopathy recapitulates ALS-FUS phenotypes**

433 Next, to determine whether short RNA oligonucleotides can prevent and reverse aberrant FUS
434 condensation in human cells, we developed a light-inducible model of FUS proteinopathy based
435 on a previous model developed to control TDP-43 aggregation.¹⁵ Specifically, we generated a
436 doxycycline-inducible optogenetic Cry2-FUS (optoFUS) construct to selectively induce FUS
437 proteinopathy under the spatiotemporal control of light stimulation (Figure S4A, B). We utilized
438 Cry2olig as the tag, which is a variant of the Photolyase-Homologous Region (PHR) of the
439 Cryptochrome 2 protein from *Arabidopsis thaliana* that undergoes reversible homo-
440 oligomerization (within ~5 min) in response to blue light.⁴⁴

441

442 We first tested whether Cry2olig-mediated increases in focal intracellular concentrations of
443 optoFUS protein can seed intracellular FUS proteinopathy upon chronic light exposure. Human
444 cells treated with 10ng/mL doxycycline to express optoFUS protein were exposed to 8 hours of
445 blue light (~0.1-0.3mW/cm², 465nm) or darkness, and were then examined by
446 immunofluorescence (Figure S4B). Interestingly, cells expressing optoFUS that were exposed to
447 blue light exhibited a significant depletion of nuclear optoFUS signal and enhanced formation of

448 cytoplasmic inclusions relative to optoFUS-expressing cells kept in the dark (Figure S4A-E).
449 Fluorescence recovery after photo-bleaching (FRAP) analysis of light-induced, cytoplasmic
450 optoFUS inclusions revealed minimal recovery after photo-bleaching, indicating that optoFUS
451 inclusions had solid-like properties with limited dynamics indicative of an aberrant phase
452 transition (Figure S4F). Sedimentation analysis confirmed that light-induced optoFUS inclusions
453 were detergent-insoluble and increased the amount of insoluble endogenous FUS relative to cells
454 kept in darkness (Figure S4G). Thus, our optoFUS system recapitulates the cytoplasmic
455 aggregation and nuclear depletion of FUS observed in ALS-FUS or FTD-FUS.

456
457 To determine whether optoFUS inclusions more closely resembled ALS-FUS or FTD-FUS
458 pathology observed in postmortem patient tissues, we performed immunofluorescence analysis
459 to assess common pathological hallmarks of ALS-FUS or FTD-FUS. OptoFUS inclusions did
460 not colocalize with FET proteins EWSR1 and TAF15 (Figure S4H), two RBPs with PrLDs that
461 typically co-deposit with FUS inclusions in FTD but not in ALS patients.⁴⁵ Moreover, optoFUS
462 inclusions were recognized by the 9G6 monoclonal antibody that recognizes methylated FUS,
463 which is more consistent with ALS-FUS pathology (Figure S4I).⁴⁶⁻⁴⁸ In addition, optoFUS
464 inclusions do not co-localize with stress granule marker G3BP1 or TDP-43 (Figure S4J, K). This
465 immunocytochemical profile was also observed when optoFUS inclusions were induced in
466 human ReNcell VM neurons (Figure S4L, M), indicating consistent results across human cell
467 and neuronal models. Thus, light-activated optoFUS inclusions exhibit the hallmarks of FUS
468 pathology observed in ALS.

469 470 **RNA S1 prevents aberrant phase transitions of FUS in human cells**

471 We next tested whether the strong and weak RNA inhibitors isolated *in vitro* can prevent the
472 formation of intracellular FUS inclusions in the optoFUS system (Figure 5A). We found that 5'-
473 fluorescein-labeled RNA S1 accumulated predominantly in the cytoplasm of human cells ~2
474 hours after transfection (Figure S5A-C). Importantly, introducing RNA S1 did not alter the
475 nuclear localization of endogenous FUS (Figure S5D, E). Next, we pre-treated optoFUS-
476 expressing human cells for two hours with strong RNA inhibitors RNA S1 or RNA S2, which
477 can prevent and reverse FUS fibrillization *in vitro*, weak inhibitor RNA W1, or RNA C2, which
478 is ineffective *in vitro* (Figure 5A). After the two-hour pretreatment, blue light was applied, and

479 we monitored the formation of optoFUS inclusions. OptoFUS formed abundant cytoplasmic
480 inclusions in cells treated with RNA C2 (Figure 5B, C, S5F). Likewise, RNA W1 was ineffective
481 in preventing optoFUS inclusion formation (Figure S5F). Interestingly, despite being effective *in*
482 *vitro*, RNA S2 only slightly prevented optoFUS inclusion formation in human cells (Figure S5F).
483 Remarkably, however, pre-treatment with RNA S1 resulted in a dose-dependent reduction in
484 optoFUS inclusion formation when compared to treatment with RNA C2 (Figure 5B, C). Thus,
485 RNA S1, which is similar in length to therapeutic ASOs,²² can prevent aberrant phase transitions
486 of FUS *in vitro* and in human cells.

487
488 RNA oligos can be quickly digested by ribonucleases in cells. Thus, we also designed RNA
489 analogues with greater intracellular stability to test in our optoFUS model. Using RNA S1 as a
490 template, we designed RNA analogues with 2'OMe modifications to test both *in vitro* and in
491 cells (Table S1). 2'OMe-modified RNA S1 and unmodified RNA S1 exhibited similar ability to
492 prevent and reverse FUS fibrillization *in vitro* (Figure S5G, H). Importantly, 2'OMe-modified
493 RNA S1 exhibited slightly enhanced inhibition of optoFUS inclusion formation compared to
494 unmodified RNA S1 (Figure 5D-F). Thus, 2'OMe-modifications of RNA S1 could help stabilize
495 the oligo in cells without impairing its ability to antagonize FUS aggregation.

496 497 **RNA S1 reverses aberrant phase transitions of FUS in human cells**

498 We next determined whether treatment with RNA inhibitors could reverse formation of
499 preformed optoFUS inclusions. Thus, optoFUS-expressing cells were first subjected to chronic
500 light stimulation to induce optoFUS aggregates prior to RNA treatment and doxycycline washout
501 to eliminate further optoFUS expression during a 6-hour dark “disassembly” period (Figure 5G).
502 The control RNA C2 had little effect on preformed optoFUS inclusions (Figure 5H).
503 Remarkably, RNA S1 and 2'OMe-modified RNA S1 oligonucleotides significantly reduced
504 optoFUS inclusion burden toward levels observed in optoFUS-expressing cells kept in darkness
505 throughout the experiment (Figure 5H-I). This effect was confirmed by sedimentation analysis of
506 optoFUS cell lysates collected following the same light induction and treatment paradigm
507 (Figure 5J-K). Thus, RNA S1 and 2'OMe-modified RNA S1 can reverse aberrant FUS phase
508 transitions in human cells.

509

510 Next, we explored the kinetics of optoFUS inclusion dissolution by RNA S1 (Figure 5G).
511 Remarkably, RNA S1 reduced cytoplasmic optoFUS inclusion size within 2-3h of treatment,
512 whereas RNA C2 had no effect (Figure 5L, M). Indeed, cells treated with RNA C2 displayed
513 persistent cytoplasmic optoFUS inclusions and exhibited reduced survival after ~6-12h (Figure
514 5L, N). By contrast, cells treated with RNA S1 cleared cytoplasmic optoFUS inclusions and
515 restored nuclear FUS, which was accompanied by increased survival (Figure 5L, N). Thus, RNA
516 S1 clears cytoplasmic FUS inclusions, restores nuclear FUS, and mitigates toxicity.

517

518 **RNA S1 prevents FUS phase separation and mitigates toxicity in iPSC-derived FUS^{R521G}** 519 **motor neurons**

520 Next, we tested whether RNA S1 can prevent and reverse aberrant FUS aggregation in human
521 motor neurons. Thus, we employed iPSC-derived motor neurons (iMNs) harboring ALS-linked
522 FUS^{R521G} (Figure 6A). RNA S1 effectively prevents and reverses FUS^{R521G} fibrillization (Figure
523 S2E, I). Upon differentiation, iMNs harboring ALS-linked FUS^{R521G} exhibited increased FUS
524 mislocalization to the cytoplasm, compared to control iMNs harboring WT FUS (Figure 6B, C).
525 FUS^{R521G}-iMNs treated with RNA S1 showed partial restoration of FUS^{R521G} nuclear
526 localization, whereas control C2 RNA had no effect (Figure 6B, C). Moreover, upon sodium
527 arsenite treatment, FUS^{R521G} iMNs exhibited formation of FUS-positive stress granules, whereas
528 FUS-positive stress granules were less abundant in control iMNs (Figure 6D, E). Importantly,
529 FUS^{R521G} iMNs treated with RNA S1 but not RNA C2 exhibited a reduction in FUS-positive
530 stress granules, indicating that RNA S1 prevented FUS recruitment into these phase-separated
531 structures (Figure 6E). Moreover, RNA S1 reduced stress granule number and area in FUS^{R521G}
532 iMNs, indicating that FUS^{R521G} was likely driving stress granule assembly (Figure 6F, G).
533 Treatment of control or FUS^{R521G} iMNs with a proteotoxic stressor, tunicamycin, reduced iMN
534 viability (Figure 6H, I).⁴⁹ Remarkably, RNA S1 but not RNA C2 mitigated toxicity in FUS^{R521G}
535 iMNs, but not control iMNs (Figure 6H, I). Thus, RNA S1 is neuroprotective under proteotoxic
536 conditions in iMNs expressing ALS-linked FUS^{R521G}.

537

538 **A short, specific RNA, Clip34, directly prevents and reverses aberrant TDP-43 phase** 539 **separation**

540 In addition to FUS, cytoplasmic aggregation of other RBPs with PrLDs has been reported in
541 patient postmortem tissue in ALS/FTD and related disorders, including TAF15, EWSR1,^{45,50,51}
542 hnRNPA1, hnRNPA2,⁵²⁻⁵⁴ and TDP-43.^{3,4,7} Previously, we established that Clip34, a 34nt RNA
543 derived from the 3'UTR of the *TARDBP* gene (Table S2), which binds to TDP-43,^{13,55-58} can
544 prevent aberrant phase transitions of TDP-43 in optogenetic neuronal models and mitigate
545 associated neurotoxicity.¹⁵ At physiological concentrations and buffer conditions, purified TDP-
546 43 spontaneously phase separates.^{13,59} We now establish that Clip34 prevents (IC₅₀~0.31μM) and
547 reverses (EC₅₀~0.6μM) TDP-43 PS directly in a dose-dependent manner, whereas a control RNA
548 oligo, (AC)₁₇, which does not bind TDP-43 has no effect on TDP-43 PS (Figure S6A-F). The
549 ability of Clip34 to prevent and reverse TDP-43 PS required interaction with the TDP-43 RRM, as
550 PS by the TDP-43 mutant, TDP-43^{5FL}, which bears F147L, F149L, F194L, F229L, and F231L
551 mutations in the RRM that impair RNA binding,²⁵ was unaffected by Clip34 (Figure S6A-F).
552
553 Purified TDP-43 can also rapidly assemble in fibrillar structures.^{8,9,12,15} Importantly, Clip34 also
554 prevented TDP-43 fibrillization (IC₅₀~0.62μM), whereas (AC)₁₇ was ineffective (Figure S6G-J).
555 By contrast, Clip34 was unable to prevent or reverse TDP-43^{5FL} fibrillization (Figure S6K-M).
556 Remarkably, Clip34 but not (AC)₁₇, could partially reverse aggregation of TDP-43 (Figure 7A-
557 C). Thus, Clip34 engages the TDP-43 RRM to prevent *and* reverse TDP-43 PS and aggregation.
558 Our findings suggest that short, specific RNAs might be broadly applicable to antagonize
559 aberrant phase transitions of disease-linked RBPs with PrLDs.

560

561 **A short, specific RNA, Clip34, reverses aberrant TDP-43 phase separation in human cells**

562 We next investigated whether Clip34 could reverse aberrant TDP-43 phase separation in human
563 cells. Thus, we developed a new optogenetic model of full-length TDP-43 aggregation based
564 upon the Corelet system.³⁹ Cytoplasmic iLID-FTH1 cores were co-expressed with full-length
565 TDP-43 that was N-terminally tagged with mCherry-SspB (ssTDP43) under the control of the
566 doxycycline-inducible Tet3G promoter (Figure 7D). Human (HEK293) cells expressing these
567 constructs were exposed to 10ng/mL doxycycline treatment and chronic blue light activation
568 (~0.3-1mW/cm², 465nm) or darkness for 8h (Figure 7E, F) to induce TDP-43 condensation.
569 Automated light activation and live-cell imaging (Figure S7A-F) revealed significant
570 accumulation of ssTDP43 condensates in cells exposed to chronic blue light but not cells kept in

571 the darkness (Figure 7E, F). Importantly, cells expressing ssTDP43 alone (without iLID cores)
572 exposed to the same light activation conditions did not form ssTDP43 condensates (Figure 7E,
573 F). Thus, ssTDP-43 condensates form due to a specific effect of light-induced Corelet
574 association rather than by a non-specific effect of blue light exposure (Figure 7E, F).

575
576 We next determined the effect of increased light exposure on TDP-43 dynamics within the
577 induced ssTDP43 condensates. FRAP analysis was performed on human cells expressing iLID
578 cores and ssTDP43 both before light exposure and on ssTDP43 assemblies in response to
579 increasing lengths of blue light activation (~ 0.1 - 0.3 mW/cm², 465nm) (Figure 7G). Initial
580 assemblies of ssTDP43 formed in response to 30 minutes of blue light displayed nearly full
581 fluorescence recovery following bleaching, suggesting a dynamic or liquid-like state of these
582 condensates (Figure 7G). However, a progressive decrease in recovery was observed of
583 condensates exposed to increasing lengths of blue light activation, indicating arrested dynamics
584 of these structures over time that remain stable for at least 12 hours following light removal
585 (Figure 7G). Thus, much like *in vitro* reactions,⁵⁹⁻⁶¹ light-induced ssTDP43 aggregate formation
586 in a cellular context begins with an initial liquid-like stage followed by maturation of these
587 condensates into solid-phase inclusions over time. Furthermore, the aberrant, solid TDP-43
588 assemblies formed after chronic (8 hour) blue light activation bore the pathological hallmarks of
589 hyperphosphorylation (Figure 7H) and colocalization with p62 (Figure 7I). These phenotypes are
590 commonly observed with TDP-43 inclusions in ALS/FTD postmortem patient tissue.⁴

591
592 Next, we tested whether Clip34 affects endogenous TDP-43 localization or function. Ideally,
593 Clip34 would not perturb endogenous TDP-43 localization or splicing activity. Indeed, Clip34
594 treatment did not change the nuclear localization of endogenous TDP-43 (Figure S7G, H).
595 Moreover, using a CFTR minigene assay to assess TDP-43 splicing activity, we found that the
596 splicing function of TDP-43 was not affected by Clip34 treatment (Figure S7I-K). Thus, Clip34
597 does not affect endogenous TDP-43 localization or splicing activity.

598
599 To test whether Clip34 could reverse TDP-43 aggregation within human cells, we induced the
600 formation of ssTDP43 inclusions with 10 hours of chronic blue light activation (~ 0.1 -
601 0.3 mW/cm², 465nm) (Figure 7J). Doxycycline was then washed out to switch off ssTDP-43

602 expression, and cells were treated with control RNA C2 or Clip34 and imaged for 10 hours
603 (Figure 7J). Remarkably, treatment with Clip34 resulted in a significant decrease in TDP-43
604 inclusion size over time when compared to control RNA C2-treated cells along with a restoration
605 of nuclear TDP-43 (Figure 7K, L). Indeed, TDP-43 inclusions were cleared, and TDP-43 was
606 restored to the nucleus (Figure 7K, L). Importantly, Clip34 significantly extended survival in
607 cells containing TDP43 inclusions at the onset of imaging (Figure 7M). Thus, preformed TDP-43
608 and FUS inclusions can be reversed by short, specific RNAs in human cells to mitigate toxicity.
609 Since short RNA oligonucleotides can be effectively delivered to the human brain, these agents
610 could have therapeutic utility for ALS/FTD and related disorders.
611

612 **Discussion**

613 An important innovation for ALS/FTD treatment will be the advent of deliverable therapeutic
614 agents that reverse the aberrant cytoplasmic aggregation of TDP-43 and FUS, and return these
615 proteins to native form and nuclear function.¹ These agents would be able to counter any toxic
616 gain of function of cytoplasmic aggregated TDP-43 or FUS conformers, as well as any toxic loss
617 of TDP-43 or FUS function.¹ Here, we have identified short RNAs (25-34 nts) that can prevent
618 and, remarkably, reverse aberrant phase transitions of FUS and TDP-43 *in vitro* and in human
619 cells. Short RNA oligonucleotides of this length can be readily delivered to the CNS.²¹ Hence,
620 these agents could have therapeutic utility for ALS/FTD and related disorders.

621
622 Our most potent RNA for FUS is RNA S1 (Table S2), a 25mer containing GGUG and GGU
623 FUS-binding motifs, which is derived from the 3'UTR of the *BDNF* gene.²⁶ RNA S1 directly
624 prevents and reverses condensation and fibrillization of purified FUS and ALS-linked FUS
625 variants. RNA S1 engages the RRM to prevent and reverse FUS fibrillization. Accordingly,
626 mutating the FUS RRM to an RNA-binding deficient form induced cytoplasmic FUS
627 aggregation in human cells in our optogenetic model. However, RNA S1 binding to the RRM is
628 not sufficient as RNA S1 was unable to antagonize fibrillization of FUS_{371X}, which harbors the
629 RRM but lacks the C-terminal RGG domains and ZnF. Since RNA S1 could prevent and reverse
630 fibrillization of a FUS ZnF mutant, FUS_{4C-A}, these findings suggest that RNA S1 must engage
631 the FUS RRM and RGG regions to antagonize FUS fibrillization. Indeed, NMR revealed that
632 RNA S1 can engage the FUS RRM and a RGG domain tightly. These binding events likely elicit
633 a conformational change in FUS, which promotes FUS solubilization regardless of whether FUS
634 is trapped in a liquid condensate or a solid fibril. This hypothesis is supported by our smFRET
635 observations where another strong RNA inhibitor, RNA S2, locks FUS in a conformation that is
636 averse to the dynamic multimerization. We suggest that these short RNAs enforce a FUS
637 conformation that limits the multivalency that underpins PS and fibrillization.

638
639 We found several short RNAs (S1-S8; Table S2) that strongly inhibited FUS PS and
640 fibrillization. However, RNAs S1 and S2 were unusual in their ability to prevent and reverse
641 FUS PS and fibrillization. Moreover, not any FUS-binding RNA can antagonize FUS PS and
642 fibrillization. We uncovered several short RNAs that engage FUS (e.g., W1; Table S2) that allow

643 FUS PS but reduce FUS fibrillization. We also found several short RNAs (N1-N6) that had no
644 effect on FUS PS and fibrillization. Overall, our findings suggest that RNA sequence, length, and
645 structure encode the ability to prevent and reverse FUS PS and fibrillization. Effective RNAs
646 engage multiple RNA-binding domains of FUS to elicit these effects.

647

648 Even though RNA S1, S2, and W1 can prevent FUS fibrillization at the pure protein level, only
649 RNA S1 was effective in human cells and motor neurons at antagonizing aberrant FUS assembly
650 and toxicity. We employed unmodified forms of these RNAs, which may limit their stability in
651 cells. Nonetheless, RNA S1 was effective in cells as an unmodified RNA and was also effective
652 *in vitro* and in cells as a 2'OMe-modified version to increase stability in cells. It will be
653 important to determine the precise features of short RNAs that enable activity in a neuronal
654 context. Importantly, RNA S1 prevented and reversed the formation of aberrant cytoplasmic
655 FUS condensates in optogenetic models of FUS proteinopathy. Here, RNA S1 also promoted
656 nuclear localization of FUS. Moreover, RNA S1 prevented cytoplasmic FUS phase separation,
657 promoted nuclear FUS localization, and mitigated proteotoxicity in human iPSC-derived
658 FUS^{R521G} motor neurons.

659

660 Our lead RNA for TDP-43 is Clip34 (Table S2), a 34mer that is derived from the 3'UTR of the
661 *TARDBP* gene. We establish that Clip34 can effectively and directly prevent and reverse TDP-43
662 PS, even at substoichiometric concentrations. Clip34 can also effectively and directly prevent
663 aggregation of purified TDP-43 and can even partially solubilize preformed TDP-43 aggregates.
664 Not any short RNA can exert these effects, which requires Clip34 to specifically engage the
665 TDP-43 RRM. Importantly, in an optogenetic model of TDP-43 proteinopathy in human cells,
666 Clip34 dissolves aberrant cytoplasmic TDP-43 condensates, restores nuclear TDP-43, and
667 mitigates TDP-43 proteotoxicity.

668

669 It is interesting to note that our lead RNAs for FUS and TDP-43 emerge from 3'UTR
670 sequences.^{26,55,62} This finding might indicate an unusual ability of specific 3'UTR sequences to
671 influence aberrant phase separation of RBPs with PrLDs. Moreover, it appears that TDP-43 and
672 FUS inclusions may be susceptible to dissolution by specific short RNAs, which raises the
673 possibility that cells may even regulate TDP-43 or FUS assembly in this way. Indeed, amyloid-

674 like forms of TDP-43 are utilized for beneficial purposes as in myogranules that promote skeletal
675 muscle development and regeneration.⁶³ It may be possible for cells to harness these stable TDP-
676 43 structures if mechanisms are readily available to promote their dissolution, which could
677 include specific short RNAs and nuclear-import receptors (NIRs).^{8,19}

678

679 A possible concern with employing short RNAs in this way is that they might remain too stably
680 bound to TDP-43 or FUS and thus interfere with essential RNA-processing reactions. However,
681 we find that RNA S1 and Clip34 are not toxic to human cells in culture and do not affect the
682 endogenous nuclear localization of FUS or TDP-43. Moreover, these short RNAs localize
683 primarily to the cytoplasm where they would not interfere with nuclear functions of FUS and
684 TDP-43. Indeed, Clip34 does not affect the ability of TDP-43 to function in specific pre-mRNA
685 splicing reactions. In ALS/FTD, cytoplasmic TDP-43 inclusions are relatively devoid of RNA,¹⁵
686 which could render aggregated conformers more susceptible to targeting with short RNAs.
687 Furthermore, once FUS or TDP-43 are solubilized by the short RNA they would then engage
688 their cognate NIR for transport to the nucleus. When NIRs engage their RBP cargo they cause
689 the RBP to release any RNA, such that an apo form of the RBP is transported back to the
690 nucleus.^{40,42} Thus, the short RNA would be recycled for further rounds of RBP disaggregation in
691 the cytoplasm and would not affect nuclear RBP function.

692

693 We suggest that these short RNAs are attractive therapeutic candidates for further development
694 since they could mitigate gain of toxic function and loss of function toxicity in ALS/FTD
695 connected with TDP-43 or FUS proteinopathy. Indeed, it will be of great interest to assess
696 whether these short RNAs can mitigate neurodegeneration in mouse models of TDP-43 and FUS
697 proteinopathy. Moreover, oligonucleotides of this size can be effectively delivered to the CNS of
698 patients as with several therapeutic ASOs.^{21,22,64} ASOs are also being pursued against FUS,
699 ataxin 2, and TDP-43 as potential therapeutics for ALS/FTD with promising results in model
700 systems and progression to clinical trials.⁶⁵⁻⁶⁷ Nonetheless, this strategy runs the risk of
701 promoting loss of function toxicity due to knockdown of these targets, which may be particularly
702 problematic for TDP-43.⁶⁸ By contrast, our short RNAs would restore RBPs to native structure
703 and function thereby eliminating toxicity due to gain and loss of function, which could yield
704 more powerful therapeutic effects. Our strategy could be applied broadly to other RBPs with

705 PrLDs, including hnRNPA1, hnRNPA2, TAF15, and EWSR1, which also accumulate in
706 cytoplasmic aggregates in ALS/FTD and related degenerative disorders,³⁰ as well as other RBPs
707 with intrinsically-disordered regions, such as tau which forms cytoplasmic fibrils in various
708 tauopathies, including Alzheimer's disease.⁶⁹
709

710 **Acknowledgments**

711 We thank Edward Barbieri, Linamarie Miller, and Miriam Linsenmeier for critical reading of the
712 manuscript, and Frederic Allain and Fionna Loughlin for NMR assignments. L. G. was
713 supported by Dr. Ralph and Marian Falk Medical Research Trust, Frick Foundation for ALS
714 Research, and NIH grants R35GM138109 and RF1NS121143. J.R.M. was supported by a
715 fellowship from the Center for Protein Conformational Diseases at the University of Pittsburgh.
716 A.M.G. was supported by the Milton Safenowitz Postdoctoral Fellowship from the ALS
717 Association and NIH grant T32NS086749. K.E.C. is supported by NIH grants T32GM132039
718 and F31NS129101. H.M.O. is supported by an AstraZeneca Post-Doctoral Fellowship, an
719 Alzheimer's Association Research Fellowship, and the Johnson Foundation. J.L. is supported by
720 an Alzheimer's Association Research Fellowship and a Warren Alpert Distinguished Scholar
721 Award. B.P. was supported by American Heart Association and BrightFocus Post-Doctoral
722 Fellowships. A.C.M. was supported in part by NIH grant T32GM007601 and NSF graduate
723 fellowship. N.L.F. was supported by NIH grants R01GM147677 and R01NS116176. C.J.D. is
724 supported by NIH grants R01NS105756, R21AG064940, and R01NS127187, Target ALS, and
725 the Robert Packard Center for ALS Research. J.S. is supported by grants from The Packard
726 Center for ALS Research at Johns Hopkins, Target ALS, The Association for Frontotemporal
727 Degeneration, the Amyotrophic Lateral Sclerosis Association, the Office of the Assistant
728 Secretary of Defense for Health Affairs through the Amyotrophic Lateral Sclerosis Research
729 Program (W81XWH-20-1-0242).

730

731 **Author Contributions**

732 Conceptualization: L.G., J.R.M, K.E.C., H.W., J.D.R., H.M.O., J.L., B.L.L., Y.S., E.J.H., A.C.,
733 N.L.F., S.M., C.J.D., and J.S. Methodology: L.G., J.R.M, J.C.M., K.E.C., H.W., J.D.R., H.M.O.,
734 J.L., B.L.L., La.G., A.C.M., T.P., A.M.G., Z.D., A.C., N.L.F., S.M., C.J.D., and J.S. Validation:
735 L.G., J.R.M, J.C.M., K.E.C., H.W., J.D.R., H.M.O., J.L., B.L.L., La.G., E.R., K.M.K., A.C.M.,
736 T.P., B.P., A.M.G., Z.D., J.L.C., A.S., G.P., E.L., C.E., Y.S., E.J.H., A.C., N.L.F., S.M., C.J.D.,
737 and J.S. Formal analysis: L.G., J.R.M, J.C.M., K.E.C., H.W., J.D.R., La.G., A.C.M., T.P., A.C.,
738 N.L.F., S.M., C.J.D., and J.S. Investigation: L.G., J.R.M, J.C.M., K.E.C., H.W., J.D.R., H.M.O.,
739 J.L., B.L.L., La.G., E.R., K.M.K., A.C.M., T.P., B.P., A.M.G., Z.D., J.L.C., A.S., G.P., E.L.,
740 C.E., A.C., C.J.D. Resources: L.G., J.R.M, J.C.M., K.E.C., J.D.R., H.M.O., J.L., B.L.L., La.G.,

741 A.C.M., T.P., B.P., Z.D., A.S., G.P., E.L., C.E., A.C., N.L.F., S.M., C.J.D., and J.S. Data
742 Curation: L.G., J.R.M, J.C.M., K.E.C., J.D.R., La.G., A.C.M., T.P., A.C., N.L.F., S.M., C.J.D.,
743 and J.S. Writing – Original Draft: L.G., J.R.M, K.E.C., J.D.R., La.G., N.L.F., S.M., C.J.D., and
744 J.S. Writing - Review & Editing: L.G., J.R.M, J.C.M., K.E.C., H.W., J.D.R., H.M.O., J.L.,
745 B.L.L., La.G., E.R., K.M.K., A.C.M., T.P., B.P., A.M.G., Z.D., J.L.C., A.S., G.P., E.L., C.E.,
746 Y.S., E.J.H., A.C., N.L.F., S.M., C.J.D., and J.S. Visualization: L.G., J.R.M, J.C.M., K.E.C.,
747 J.D.R., La.G., A.C.M., T.P., N.L.F., S.M., C.J.D., and J.S. Supervision: L.G., A.C., N.L.F., S.M.,
748 C.J.D., and J.S. Project administration: L.G., A.C., N.L.F., S.M., C.J.D., and J.S. Funding
749 acquisition: L.G., J.R.M, K.E.C., H.M.O., J.L., A.C.M., B.P., A.M.G., N.L.F., C.J.D., and J.S.
750

751 **Declarations of Interests**

752 The authors have no conflicts, except for: J.S. is a consultant for Dewpoint Therapeutics, ADRx,
753 and Neumora. J.S. a shareholder and advisor at Confluence Therapeutics. C.J.D. is a scientific
754 founder, advisor, and shareholder of Confluence Therapeutics. J.R.M. is a consultant for
755 Confluence Therapeutics.

756

757 **STAR Methods**

758 **KEY RESOURCES TABLE**

REAGENT or RESOURCE	SOURCE	IDENTIFIER
Antibodies		
goat MAP2	Phosphosolutions	Cat# 1099 RRID:AB_2752241
mouse G3BP1	Santa Cruz Biotechnology	Cat# sc-365338 RRID:AB_10846950
rabbit FUS	Proteintech	Cat# 11570-1-AP RRID:AB_2247082
Alexa Fluor-647 donkey anti-goat	Jackson ImmunoResearch	Cat# 705-605-003 RRID:AB_2340436
Alexa Fluor-594 donkey anti-mouse	Jackson ImmunoResearch	Cat# 715-585-150 RRID:AB_2340854
Alexa Fluor-488 donkey anti-rabbit	Jackson ImmunoResearch	Cat# 711-545-152 RRID:AB_2313584
Bacterial and Virus Strains		
<i>E. coli</i> BL21 DE3 (RIL) cells	Agilent	Cat# 230245
<i>E. coli</i> One Shot™ BL21 Star™ (DE3) cells	Thermo Fisher	Cat# C601003
Chemicals, Peptides, and Recombinant Proteins		
EDTA-free Protease Inhibitor Cocktail	Roche	Cat# 11873580001
Lysozyme	Sigma-Aldrich	Cat# L6876
mTeSR+	StemCell Technologies	5825
DMEM:F12	Corning	15090CV
Neurobasal	Gibco	12348017
NEAA	Gibco	11-140-050

Glutamax	Gibco	35050061
N2	Gibco	17502048
B27	Gibco	17504044
SB431542	StemCell Technologies	72234
LDN-193189	Sigma-Aldrich	SML0559
Retinoic Acid (RA)	Sigma-Aldrich	R2625
Smoothened-Agonist (SAG)	Cayman Chemical	11914
SU5402	Cayman Chemical	13182-5
DAPT	Cayman Chemical	13197
TrypLE	Gibco	12604013
DNaseI	Invitrogen	18-047-019
BDNF	PeproTech	450-02
GDNF	PeproTech	450-10
CNTF	PeproTech	450-13
Ascorbic acid	Sigma-Aldrich	A4403
Lipofectamine RNAiMAX	Invitrogen	13-778-075
OptiMEM	Gibco	51-985-091
Sodium Arsenite	Sigma-Aldrich	1062771000
Tunicamycin	Sigma-Aldrich	T7765
DMSO	Sigma-Aldrich	D4540
PBS	Gibco	10010023
32% PFA	Electron Microscopy Sciences	15714-S
Donkey Serum	Jackson ImmunoResearch	017-000-121
Triton x-100	Sigma-Aldrich	T8787
Prolong Glass mounting media	Invitrogen	P36981
Bovine Growth Serum	Cytiva HyClon	SH30541.03HI
DMEM, high glucose, pyruvate, no glutamine	Gibco	10313039
GlutaMAX™ Supplement	Gibco	35050061
Heparin sodium salt	Sigma-Aldrich	H3149-10KU
Animal-Free Recombinant Human EGF	PeproTech	AF-100-15
RNasin® Ribonuclease Inhibitor	Promega	N2111
Recombinant Human FGF-basic (154 a.a.)	PeproTech	100-18B

GST-FUS	This paper	N/A
GST-FUS ^{C428A:C433A:C444A:C447A}	This paper	N/A
GST-FUS ^{F305L:F341L:F359L:F368L}	This paper	N/A
GST-FUS ^{371X}	This paper	N/A
GST-FUS ^{P525L}	This paper	N/A
GST-FUS ^{R244C}	This paper	N/A
GST-FUS ^{R216C}	This paper	N/A
pHis-TEV	This paper	N/A
His-FUS ₂₆₉₋₄₅₄	This paper	N/A
TDP-43-MBP-his	This paper	N/A
TDP-43 ^{5FL} -MBP-his	This paper	N/A
Critical Commercial Assays		
CellTiter-Glo kit	Promega	G7570
QuikChange Site-Directed Mutagenesis Kit	Agilent	Cat# 210518
NEBNext® Small RNA Library Prep Set for Illumina®	New England Biolabs	Cat# E7330S
Experimental Models: Cell Lines		
HEK293 cells	ATCC	293 [HEK-293] CRL-1573
ReNcell® VM Human Neural Progenitor Cell Line	Millipore	SCC008
FUS R521G iPSC line	Cedars-Sinai RMI iPSC Core	CS37iALS-FUSn2
CS06 iPSC line	Cedars-Sinai RMI iPSC Core	CS06iCTR-n2
Oligonucleotides		
See Table S2 for RNA oligonucleotides	Horizon Discovery Ltd or IDT	N/A
Recombinant DNA		
GST-FUS	Sun et al. ¹⁰	N/A
GST-FUS ^{C428A:C433A:C444A:C447A}	This Paper	N/A
GST-FUS ^{F305L:F341L:F359L:F368L}	This Paper	N/A
GST-FUS ^{371X}	This Paper	N/A
GST-FUS ^{P525L}	Sun et al. ¹⁰	N/A
GST-FUS ^{R244C}	This Paper	N/A
GST-FUS ^{R216C}	This Paper	N/A
pHis-TEV	Cupo and Shorter ⁷⁰	N/A

Tet-On 3G Inducible Expression System	Takarabio	631168
ssTDP-43	This Paper	N/A
optoFUS	This Paper	N/A
pHR:SFFVp:TDP43C:mCherry:SspB	Bracha et al. ³⁹	Addgene: 122669
pHR:SFFVp:iLid:eGFP:FTHi	Bracha et al. ³⁹	Addgene: 122149
pJ4M/TDP-43 plasmid	Wang et al. ⁵⁹	Addgene 104480
Software and Algorithms		
ImageJ	NIH	https://imagej.nih.gov/ij/ ; RRID: SCR_003073
GraphPad Prism	GraphPad Software Inc	https://www.graphpad.com/scientific-software/prism/ ; RRID: SCR_002798
Bowtie	Johns Hopkins University	https://bowtie-bio.sourceforge.net/index.shtml
HOMER	UCSD	http://homer.ucsd.edu/homer/motif/
Nikon Elements	Nikon	NIS-Elements

759

760 **RESOURCE AVAILABILITY**

761 ***Lead contact***

762 Further information and requests for resources and reagents should be directed to and will be
763 fulfilled by the lead contact, James Shorter (jshorter@penncmedicine.upenn.edu).

764

765 ***Materials availability***

766 Plasmids newly generated in this study will be made readily available to the scientific
767 community. We will honor requests in a timely fashion. Material transfers will be made with no

768 more restrictive terms than in the Simple Letter Agreement or the Uniform Biological Materials
769 Transfer Agreement and without reach through requirements.

770

771 ***Data and code availability***

772 Any additional information required to reanalyze the data reported in this paper is available from
773 the lead contact upon request.

774

775 **EXPERIMENTAL MODEL AND SUBJECT DETAILS**

776 **HEK293 cell culture**

777 HEK293 cells (female, purchased from ATCC) were maintained at 37°C and 5% CO₂ in DMEM
778 (high glucose, pyruvate) (Thermo Fisher Scientific) supplemented with GlutaMAX (Thermo
779 Fisher Scientific) and 10% Bovine Growth Serum (Cytiva HyClon). Transfections were
780 performed using Lipofectamine 3000 (Thermo Fisher Scientific) according to manufacturer's
781 instructions following cell seeding onto coverslips or culture plates coated with 50mg/mL
782 collagen (Gibco) and overnight incubation at 37°C/5% CO₂.

783

784 **ReNcell[®] VM human neural progenitor cell culture**

785 ReNcell[®] VM human neural progenitor cells (male, purchased from Millipore) were maintained
786 at 37°C and 5% CO₂ in DMEM/F12 (Gibco) supplemented with GlutaMAX, B27 (Gibco),
787 2ng/mL heparin (Sigma-Aldrich), 20ng/mL bFGF (PeproTech) and 20ng/mL hEGF
788 (PeproTech). Neuronal differentiation was performed as previously described¹⁵ and
789 differentiated neurons were maintained at 37°C and 5% CO₂/5% O₂ prior to lentiviral
790 transduction.

791

792 **Induced pluripotent stem cell (iPSC) culture**

793 Induced Pluripotent Stem Cell lines CS37iALS-FUSn2 (female, 37 years old at time of
794 collection) and CS06iCTR-n2 (female, 82 years old at the time of collection) were obtained from
795 the Cedars-Sinai RMI iPSC Core, cultured in Matrigel (Corning) and mTeSR+ (StemCell
796 Technologies) and kept in a humidified chamber with regulated levels of CO₂ (5%) and
797 temperature (37°C). All procedures for iPSC culture maintenance and differentiation were
798 performed as described.⁷¹⁻⁷³

799 **iPSC differentiation**

800 For differentiation, 1×10^6 iPSCs were plated in 6 well plates. Once cells reached ~90%
801 confluency media was changed from mTeSR+ to N2B27 media (50% DMEM:F12, 50%
802 Neurobasal, plus NEAA, Glutamax, N2 and B27; all from Gibco) plus $10 \mu\text{M}$ SB431542
803 (StemCell Technologies), 100 nM LDN-193189 (Sigma-Aldrich), $1 \mu\text{M}$ RA (Sigma-Aldrich) and
804 $1 \mu\text{M}$ Smoothened-Agonist (SAG, Cayman Chemical). Media was changed daily for a total of 6
805 days. Cells were then switched to N2B27 including $1 \mu\text{M}$ RA, $1 \mu\text{M}$ SAG, $4 \mu\text{M}$ SU5402 (Cayman
806 Chemical) and $5 \mu\text{M}$ DAPT (Cayman Chemical) and media was changed daily until day 13.
807 Neurons were dissociated at day 14 using TrypLE and DNaseI, plated in Matrigel-coated 24-
808 well plates with glass coverslips for confocal imaging studies and Matrigel-coated 96-well white
809 plates for viability assays. Cells were fed every 2 days and maintained for 13 additional days in
810 Neurobasal media + NEAA, Glutamax, N2, B27, plus 10 ng/mL BDNF, GDNF, CNTF (all from
811 PeproTech) and $0.2 \mu\text{g/ml}$ Ascorbic acid (Sigma-Aldrich).

812

813 **METHOD DETAILS**

814 **Cloning**

815 QuikChange Site-Directed Mutagenesis Kit (Agilent) was used to generate mutant plasmids (i.e.,
816 GST-FUS¹⁻²¹⁴, GST-FUS^{C428A:C433A:C444A:C447A}, GST-FUS^{F305L:F341L:F359L:F368L}, GST-FUS^{371X},
817 GST-FUS^{P525L}, GST-FUS^{R244C}, GST-FUS^{R521G} and GST-FUS^{R216C}) according to the
818 manufacturer's instructions. All GST-FUS constructs have a TEV cleavage site between GST
819 and FUS as described.¹⁰ Mutations were verified by DNA sequencing.

820

821 pJ4M/TDP-43 encoding TDP-43-MBP-his with a TEV cleavage site between TDP-43 and MBP
822 was from Addgene.⁵⁹ The 5FL (F147L:F149L:F194L:F229L:F231L) mutant was generated via
823 QuikChange Multi Site-directed Mutagenesis (Agilent) and verified via Sanger sequencing.

824

825 All doxycycline-inducible expression constructs, including FUS-SspB mutants, optoFUS and
826 ssTDP43, were generated through Gibson Assembly (HiFi DNA Assembly Master Mix, NEB) of
827 PCR-generated fragments inserted at the NotI/EcoRI restriction enzyme sites of a Tet3G base
828 vector (synthesized by GeneWiz). Synthesized gBlocks (IDT) containing 4FL and 4CA point
829 mutations were used as templates for PCR of fragments used to assembly FUS-SspB mutants.

830 Plasmids containing MBP-tagged FUS (Plasmid #98651, Addgene) were used as templates to
831 generate WT FUS-SspB and optoFUS constructs. Previous-generation optoTDP43 constructs¹⁵
832 containing TDP-43 coding sequences were used as PCR templates to generate ssTDP43
833 constructs. For generation of lentiviral transfer vectors, PCR-generated fragments were inserted
834 at the BsrGI/BamHI restriction enzyme sites by Gibson Assembly of a third-generation base
835 lentiviral vector described previously¹⁵ for human synapsin promoter-driven expression of target
836 proteins.

837

838 **Purification of TEV protease**

839 TEV protease was purified as described.⁷⁰

840

841 **Purification of GST-FUS**

842 GST-FUS, GST-FUS¹⁻²¹⁴, GST-FUS^{C428A:C433A:C444A:C447A}, GST-FUS^{F305L:F341L:F359L:F368L}, GST-
843 FUS^{371X}, GST-FUS^{P525L}, GST-FUS^{R244C}, and GST-FUS^{R216C} were purified as described.¹⁰

844 Briefly, N-terminally tagged GST-FUS was overexpressed in BL21(DE3)RIL *E. coli*. The *E. coli*
845 cells were then lysed by sonication on ice in PBS and protease inhibitors (cOmplete, EDTA-free,
846 Roche Applied Science). The protein was purified over Glutathione Sepharose 4 Fast Flow beads
847 (GE Healthcare) and eluted from the beads using FUS assembly buffer (50mM Tris-HCl pH 8,
848 200mM trehalose, 1mM DTT, and 20mM reduced glutathione).

849

850 **Purification of his-tagged FUS₂₆₉₋₄₅₄ for NMR experiments**

851 His-tagged FUS₂₆₉₋₄₅₄ was expressed BL21*(DE3) (Life Technologies) in M9 minimal media
852 with ¹⁵N ammonium chloride for isotopic labeling. Cultures were grown at 37°C until an OD₆₀₀
853 of 0.6-1 and induced with 1mM IPTG for 4h and cells were harvested by centrifugation. FUS<sub>269-
854 454</sub> was purified as described.³³ Briefly, bacterial pellets were resuspended in 20mM sodium
855 phosphate, 1M NaCl, 10mM imidazole pH 7.4 with protease inhibitor tablets (Pierce A32963).
856 The lysate was clarified by centrifugation at 20,000rpm for 1h at 4°C, filtered, and applied to a
857 5mL HisTrap column. The protein was eluted with a gradient of 10-300mM imidazole. The His-
858 tag was cleaved by TEV protease containing a histidine tag, and the protein was dialyzed
859 overnight into 20mM sodium phosphate, 1M NaCl, 10mM imidazole pH 7.4. The protein was
860 filtered and applied to a 5mL HisTrap column to remove the His-tag and TEV protease.

861 **Bacterial growth and recombinant protein purification for TDP-43-MBP-his utilized in PS**
862 **assays**

863 Wild-type (WT) and 5FL TDP-43-MBP-his expression plasmids were transformed into *E. Coli*
864 One Shot™ BL21 Star™ (DE3) cells (ThermoFisher). Transformed *E. coli* were grown at 37°C
865 in 1L of LB media supplemented with 0.2% dextrose and 50µg/mL kanamycin until OD₆₀₀=0.5-
866 0.6. Cells were then incubated at 4°C for 30-45min. Protein expression was induced with
867 addition of 1mM IPTG and then bacterial cultures were incubated for 16h at 16°C. Cells were
868 collected by centrifugation. Cell pellets were resuspended in 1M NaCl, 20mM TrisHCl (pH 8.0),
869 10mM imidazole, 10% glycerol, and 2.5mM 2-mercaptoethanol and supplemented with
870 cOmplete, EDTA-free protease inhibitor cocktail tablets (Roche), then lysed via sonication. Cell
871 lysates were centrifuged at 48,384rcf at 4°C for 1h. Filtered lysate was purified via FPLC using a
872 XK 50/20 column (Cytiva) packed with Ni-NTA agarose beads (Qiagen), which were
873 equilibrated in the resuspension buffer. Protein was recovered via a 0-80% gradient elution using
874 1M NaCl, 20mM TrisHCl (pH 8.0), 10mM imidazole, 10% glycerol and 2.5mM 2-
875 mercaptoethanol as the base buffer and 1M NaCl, 20mM TrisHCl (pH 8.0), 500mM imidazole,
876 10% glycerol and 2.5mM 2-mercaptoethanol as the elution buffer. Eluted protein was
877 concentrated using Amicon Ultra-15 centrifugal filters, MWCO 50kDa (Millipore), filtered and
878 further purified with size-exclusion chromatography using a 26/600 Superdex 200 pg column
879 (Cytiva) equilibrated with 300mM NaCl, 20mM TrisHCl (pH 8.0) and 1mM DTT. The second
880 out of three peaks, as evaluated by absorbance at 280nm, was collected,⁵⁹ spin concentrated as
881 above, aliquoted, flash frozen in liquid nitrogen, and stored at -80°C until further use.

882
883 **Bacterial growth and recombinant protein purification for TDP-43-MBP-his utilized in**
884 **aggregation assays**

885 TDP-43-MBP-his was purified as described.¹³ WT and 5FL TDP-43 expression plasmids were
886 transformed into *E. Coli* BL21-CodonPlus (DE3)-RIL competent cells (Agilent). Transformed *E.*
887 *coli* were grown in small cultures in LB with kanamycin (50µg/mL) and chloramphenicol
888 (34µg/mL) at 37°C for approximately 4h. The cultures were then transferred to 1L of LB media
889 supplemented with both antibiotics and glucose (0.2% w/v) and grown at 37°C until OD₆₀₀~0.5.
890 Protein expression was induced with addition of 1mM IPTG and then bacterial cultures were
891 incubated for 16h at 16°C. Cells were harvested by centrifugation, resuspended in

892 resuspension/wash buffer (20mM Tris-HCl pH 8.0, 1M NaCl, 10mM imidazole, 10% glycerol,
893 1mM DTT, 5 μ M Pepstatin A, 100 μ M PMSF, and cOmplete, EDTA-free, Roche Applied
894 Science protease inhibitors), and lysed by lysozyme (1 mg/mL) and sonication. Cell lysates were
895 centrifuged at 30,966rcf at 4°C for 20min. The protein was purified over Ni-NTA resin
896 (QIAGEN) and eluted from the resin using elution buffer (wash buffer except with 300mM
897 imidazole rather than 10mM imidazole). The protein was further purified over amylose resin
898 (NEB) and eluted with 20mM Tris-HCl pH 8.0, 1M NaCl, 10mM imidazole, 10% glycerol, 1mM
899 DTT, 5 μ M Pepstatin A, 100 μ M PMSF, and 10mM maltose. The protein was concentrated using
900 Amicon Ultra-15 centrifugal filters, MWCO 50kDa (Millipore), aliquoted, flash frozen in liquid
901 nitrogen, and stored at -80°C until further use.

902

903 **RNA-Seq**

904 RNA that was bound to GST-FUS during protein purification was extracted by adding DNase I
905 and then Proteinase K to the sample followed by phenol-chloroform extraction, and precipitation
906 in 100% ethanol with 70% ethanol wash. For preparing cDNA libraries for high-throughput
907 sequencing, we used the NEBNext® Small RNA Library Prep Set for Illumina® and followed
908 the manufacturer's instructions. Library quality was checked with the Agilent 2100 BioAnalyzer.
909 The sample was sequenced on the Illumina HiSeq2000 platform. The resulting sequences were
910 aligned to human genome and *E. coli* genome using Bowtie and the annotated peaks were
911 analyzed by a program HOMER for motif finding.^{74,75}

912

913 **RNA oligonucleotides**

914 RNA and fluorescein labeled RNA were purchased from Horizon Discovery Ltd or Integrated
915 DNA Technologies (IDT) (Table S2).

916

917 **FUS fibril assembly**

918 For GST-FUS, GST-FUS^{C428A:C433A:C444A:C447A}, and GST-FUS^{F305L:F341L:F359L:F368L}, GST-
919 FUS^{P525L}, GST-FUS^{R244C}, GST-FUS^{R216C}, and GST-FUS^{R521G} fibrillization was initiated by
920 addition of TEV protease to GST-FUS (5 μ M) in FUS assembly buffer (50mM Tris-HCl pH 8,
921 200mM trehalose, 1mM DTT, 0.2U/ μ L RNasin® [Promega], and 20mM glutathione) in the
922 presence or absence of 20 μ M RNA.^{10,50,51} For the dose-response curves in Figure 3H-K, RNA

923 was dosed from 0.01-1000 μ M. Fibrillization reactions were incubated at 25°C for 100 min
924 without agitation. FUS^{371X} took longer to fibrillize, and its fibrillization was initiated by addition
925 of TEV protease to GST-FUS^{371X} (10 μ M) in the presence or absence of 40 μ M RNA at 25°C for
926 24h with agitation at 1200rpm.

927

928 Turbidity was used to assess fibrillization by measuring absorbance at 395nm. Turbidity of
929 FUS+buffer without TEV condition was subtracted and the resulting absorbance was then
930 normalized to the maximum turbidity of FUS aggregation without RNA to determine the relative
931 extent of fibrillization. For sedimentation analysis, reactions were centrifuged at 16,100g for
932 10min at 4°C. Supernatant and pellet fractions were then resolved by sodium dodecyl sulfate
933 polyacrylamide gel electrophoresis (SDS-PAGE) and stained with Coomassie Brilliant Blue, and
934 the amount in either fraction (% total) was determined by densitometry in comparison to known
935 quantities of the RBP in question. For electron microscopy, fibrillization reactions (10 μ l) were
936 absorbed onto glow-discharged 300-mesh Formvar/carbon coated copper grids (Electron
937 Microscopy Sciences) and stained with 2% (w/v) aqueous uranyl acetate. Excess liquid was
938 removed, and grids were allowed to air dry. Samples were viewed by a JEOL 1010 transmission
939 electron microscope.

940

941 **FUS fibril disassembly**

942 Fibrils were assembled as above and used for disassembly reactions. 20 μ M RNA were added to
943 preformed GST-FUS, GST-FUS^{C428A:C433A:C444A:C447A}, GST-FUS^{F305L:F341L:F359L:F368L}, GST-
944 FUS^{P525L}, GST-FUS^{R244C}, GST-FUS^{R216C}, or GST-FUS^{R521G} fibrils and 40 μ M RNA were added
945 to preformed GST-FUS^{371X} fibrils to disassemble fibrils. Turbidity, sedimentation analysis, and
946 EM were used to monitor the progress of disaggregation. For turbidity, the absorbance was
947 normalized to that of the fully assembled FUS fibrils before addition of RNA to determine the
948 relative extent of disaggregation. Sedimentation analysis and EM were performed as above.

949

950 **FUS droplet formation**

951 FUS droplets were formed by incubating GST-FUS at indicated concentration in FUS assembly
952 buffer (50mM Tris-HCl pH 8, 200mM trehalose, 1mM DTT, 0.2U/ μ L RNasin®, and 20mM

953 glutathione) for 2-4h at room temperature ($\sim 23^{\circ}\text{C} \pm 2^{\circ}\text{C}$). Protein samples were then spotted onto
954 a coverslip and imaged by Differential interference contrast (DIC) microscopy.

955

956 **Single molecule FRET**

957 For smFRET measurements, the details of instrumentation and PEGylated slide preparation were
958 as described.^{32,76} Briefly, the microfluidic sample chamber was created between the plasma-
959 cleaned slide and the coverslip coated with polyethylene glycol (PEG) and biotin-PEG. Annealed
960 RNA molecules were immobilized on the PEG-passivated surface via biotin-neutravidin
961 interaction. All smFRET measurements were carried out in imaging buffer containing an oxygen
962 scavenger system to stabilize fluorophores (10mM Tris-HCl, pH 7.5, 100mM KCl, 10mM
963 trolox, 0.5% (w/v) glucose, 1mg/mL glucose oxidase and 4g/ml catalase).⁷⁶ All smFRET assays
964 were performed at room temperature ($\sim 23^{\circ}\text{C} \pm 2^{\circ}\text{C}$). Wide-field prism-type total internal
965 reflection fluorescence (TIRF) microscopy was used with a solid-state 532nm diode laser to
966 generate an evanescent field of illumination to excite the fluorophores (Cy3 or Cy5) at the
967 sample chamber. Fluorescence signals from Cy3 (donor) and Cy5 (acceptor) were
968 simultaneously collected using a water immersion objective and sent to a charge-coupled device
969 (CCD) camera after passing through the dichroic mirror (cut off = 630nm). Movies were
970 recorded over different regions of the imaging surface with a time resolution of 100ms as a
971 stream of imaging frames. FRET histograms were built by collecting FRET values from over
972 5000 molecules in 20 different fields of view (21 frames of 20 short movies). Long movies (1200
973 frames, i.e., 120s) were recorded to look through the molecular behavior using MATLAB script.

974

975 **NMR spectroscopy methods**

976 NMR experiments were recorded on a Bruker Avance 850 MHz ^1H Larmor frequency
977 spectrometer with HCN TCl z-gradient cryoprobe. All experiments were carried out at 310K.
978 Data were processed using NMRPipe software package⁷⁷ and then visualized using NMRFAM-
979 Sparky.⁷⁸ For NMR experiments, the protein was dialyzed into 20mM NaPi (pH 6.75), 150mM
980 NaCl. Assignments were kindly provided by Frederic Allain and Fiona Loughlin.³³
981 Experiments were conducted in 20mM NaPi (pH 6.75), 150mM NaCl, 10% $^2\text{H}_2\text{O}$ in the presence
982 of 60 μM FUS₂₆₉₋₄₅₄ with 60 μM RNA (i.e., 1:1).

983

984 **Fluorescence anisotropy**

985 Fluorescein-labeled RNAs (8nM) were added into GST-FUS, GST-FUS^{C428A:C433A:C444A:C447A},
986 GST-FUS^{F305L:F341L:F359L:F368L}, or GST-FUS^{371X} at indicated concentration in FUS assembly
987 buffer (50mM Tris-HCl pH 8, 200mM trehalose, 1mM DTT, and 20mM glutathione) in the
988 presence of RNasin®. Anisotropy (excitation 470 nm, emission 520 nm) was measured in 96-
989 well plate using an Infinite M1000 plate reader (Tecan). The change in anisotropy was calculated
990 by subtracting the anisotropy of 8nM fluorescein-labeled RNA and the binding curve was fitted
991 using Prism to obtain the K_D .

992

993 ***In vitro* TDP-43 PS inhibition assay**

994 RNA, TDP-43-MBP-his, and TEV protease were thawed on ice. TDP-43-MBP-his was
995 centrifuged at 16,000rcf for 10min at 4°C. RNA was diluted into PS buffer (150mM NaCl,
996 20mM HEPES pH 7.4) and TDP-43 and TEV were diluted into PS buffer supplemented with
997 1mM DTT. Equal volumes of TDP-43-MBP-his and RNA were mixed and incubated at room
998 temperature for 15min before adding an equal volume of TEV protease, for final concentrations
999 of 4µM TDP-43, and 0.01 mg/mL TEV protease in PS buffer with 0.67mM DTT and variable
1000 amounts of RNA. An Infinite M1000 or Safire2 plate reader (Tecan) was used to scan samples in
1001 a UV-transparent half-area 96-well plate (Greiner) at 350nm, once per minute, for 2h at ~25-
1002 30°C. Initial readings (T=0min) were subtracted from final readings (T=120min) then
1003 normalized to the “no RNA” controls.

1004

1005 ***In vitro* TDP-43 PS reversal assay**

1006 Equal volumes of TDP-43-MBP-his and TEV protease, and TDP-43 and buffer (negative
1007 control) were mixed at room temperature (~23°C±2°C) for final concentrations of 4.3µM TDP-
1008 43, and 0.011mg/mL TEV protease in PS buffer with 1mM DTT, then incubated at room
1009 temperature (~23°C±2°C) for 1.5h to allow for TDP-43 PS. After 1.5h, this solution was
1010 transferred to wells in a UV-transparent half-area 96-well plate (Greiner) and scanned once at
1011 350nm in the plate reader. RNAs or Buffer were added to the wells, for final concentrations of
1012 4µM TDP-43, 0.01mg/mL TEV protease in PS buffer with 0.93mM DTT and then the samples
1013 were scanned at 350 nm, once per minute for 1h at ~25-30°C. Background subtraction was
1014 performed by subtracting average readings for negative controls (TDP-43 with buffer, no TEV

1015 protease) from sample readings at T=0h (no RNA added) and at T=1h. Each sample reading at
1016 T=1h was normalized to its own T=0h reading, and then samples were normalized again to the
1017 “no RNA” controls.

1018

1019 ***In vitro* TDP-43 aggregation inhibition assay**

1020 TDP-43-MBP-his was thawed on ice and centrifuged for 10min at 21,300rcf at 4°C. TDP-43-
1021 MBP-his was buffer exchanged into 166.66mM NaCl, 22.22mM HEPES-NaOH pH 7.0,
1022 1.11mM DTT (Bio-Rad Micro Bio-Spin Chromatography Columns, following manufacturer’s
1023 instructions) and concentration was determined via NanoDrop, $e_{280}=114250 \text{ cm}^{-1}\text{M}^{-1}$. TDP-43-
1024 MBP-his and RNA (or water for controls without RNA) were added to buffer to achieve final
1025 concentrations of 5 μM TDP-43, 150mM NaCl, 20mM HEPES-NaOH pH 7.0, 1mM DTT, and
1026 the indicated RNA concentration. Samples were incubated at room temperature ($\sim 23^{\circ}\text{C} \pm 2^{\circ}\text{C}$) for
1027 15min, after which TEV protease was added at a final concentration of 2.5 $\mu\text{g}/\text{mL}$ (TEV protease
1028 elution buffer was added for the No TEV control) to remove the MBP-his tag. An Infinite
1029 M1000 Tecan plate reader was used to assess turbidity once per minute at 395 nm in a
1030 nonbinding 96-well plate (Greiner) over 16h at $\sim 25\text{-}30^{\circ}\text{C}$. The data was standardized by
1031 subtracting out the initial reading at t=1min from each respective condition. Data was then
1032 normalized to the respective No RNA control. Area under the curve analysis was used to
1033 compare the extent of aggregation for each condition (GraphPad Prism).

1034

1035 ***In vitro* TDP-43 aggregation reversal assay**

1036 TDP-43-MBP-his was thawed on ice and centrifuged for 10min at 21,300rcf at 4°C. TDP-43-
1037 MBP-his was buffer exchanged into 150mM NaCl, 20mM HEPES-NaOH pH 7.0, 1mM DTT
1038 (Bio-Rad Micro Bio-Spin Chromatography Columns, following manufacturer’s instructions) and
1039 concentration was determined via NanoDrop, $e_{280}=114250 \text{ cm}^{-1}\text{M}^{-1}$. TDP-43-MBP-his was
1040 diluted into buffer to achieve a final concentration of 4 μM TDP-43, 150mM NaCl, 20mM
1041 HEPES-NaOH pH 7.0, 1mM DTT. TEV protease was added at a final concentration of
1042 2.5 $\mu\text{g}/\text{mL}$ for WT TDP-43 to remove the MBP-his tag. Due to slower aggregation kinetics, to
1043 achieve preformed aggregates in an equivalent timeframe, TEV protease was added at a final
1044 concentration of 10 $\mu\text{g}/\text{mL}$ for 5FL TDP-43. An Infinite M1000 Tecan plate reader was used to
1045 assess turbidity once per minute at 395nm in a nonbinding 96 well plate (Greiner) over 6h at

1046 ~25-30°C. After 6h, turbidity readings were paused. RNA (or water for controls without RNA)
1047 was added to samples, resulting in final concentrations of 40µM RNA (for samples with RNA),
1048 3.648µM TDP-43, 136.8mM NaCl, 18.24mM HEPES-NaOH pH 7.0, 0.912mM DTT.
1049 Sedimentation was performed by taking samples at the end timepoint. Input samples were taken
1050 directly from the sample. Samples were centrifuged for 10min at 21,300rcf at RT. The
1051 supernatant of these centrifuged samples was taken as the supernatant sample, while the pellet
1052 was resuspended in buffer (136.8mM NaCl, 18.24mM HEPES-NaOH pH 7.0, 0.912mM DTT)
1053 for the pellet samples. 3x sample buffer with 2-mercaptoethanol was added to samples, which
1054 were boiled at 95°C for 5min. Samples were run on 4-20% Tris-HCl PAGE gels and stained with
1055 Coomassie Brilliant Blue. Quantification of bands was performed with Image Studio Lite Ver
1056 5.2. Samples at the end timepoint were also imaged by brightfield microscopy with 100x
1057 objective (EVOS M5000)

1058

1059 **iPSC neuronal culture treatment and immunostaining analyses**

1060 Oligo treatments started on day 13 after plating (DIV27) and lasted 24h. 2'OMe_RNA oligos
1061 were transfected using Lipofectamine RNAiMAX (Invitrogen) according to manufacturer's
1062 instructions. Briefly, each oligo was diluted in OptiMEM (Gibco) and combined with 1µl
1063 Lipofectamine/well, the mixture was incubated at RT for 10min and then added dropwise to the
1064 cells to a final concentration of 500nM. Neurons were always fixed at day 14 after plating
1065 (DIV28). For SG studies, oligo treatment was started on day 13, and then sodium arsenite
1066 (Sigma-Aldrich) was added 23h later at a final concentration of 0.5mM, incubated at 37°C for
1067 45min, fixed and stained.

1068

1069 For viability studies, a tunicamycin dose/response curve was performed to determine a
1070 concentration that would reduce viability significantly (reduction of >10% compared to vehicle
1071 treated) in control neurons. Tunicamycin was dissolved in DMSO (both Sigma-Aldrich), serial
1072 dilutions were made in OptiMEM, added dropwise to each well and incubated at 37°C for 24h.
1073 Cell viability was measured using the CellTiter-Glo kit (Promega). For oligo experiments,
1074 tunicamycin was used at doses of 25µM and 50µM, treatment was started 1h after oligo
1075 transfection, incubated for 24h at 37°C and cell viability measured using CellTiter-Glo.

1076 For immunofluorescence studies, cells were washed once in PBS (Gibco) and fixed in 4% PFA
1077 (Electron Microscopy Sciences) immediately after treatments ended. Cells were kept on PFA for
1078 20min, then washed 3 times in PBS and blocked with 5% Donkey Serum (Jackson
1079 ImmunoResearch) plus 0.3% TX-100 (Sigma-Aldrich) in PBS for 30min at room temperature
1080 ($\sim 23^{\circ}\text{C} \pm 2^{\circ}\text{C}$). Primary antibodies (goat MAP2 1:1000, Phosphosolutions; mouse G3BP1 1:100,
1081 Santa Cruz; rabbit FUS 1:300, Proteintech) were diluted in blocking solution and incubated
1082 overnight at 4°C . Secondary antibodies (donkey Alexa Fluor, Jackson ImmunoResearch) were
1083 used at 1:1000 dilution in blocking solution and incubated for 60min at 30min at room
1084 temperature ($\sim 23^{\circ}\text{C} \pm 2^{\circ}\text{C}$). All treatments/cell lines were treated and probed simultaneously to
1085 decrease variability. Coverslips were mounted in Prolong Glass (Invitrogen).

1086

1087 Images were acquired (10/group) using an A1R Nikon Confocal Microscope and fields of view
1088 (FOV) were processed for analyses using Nikon NIS Elements Software. Briefly, SG signal on
1089 untreated control neurons was thresholded using a binary layer for 594nm channel (G3BP1) and
1090 settings were kept consistent across treatments. Within each FOV, total number of neurons
1091 (DAPI+/MAP2+) and SG+ neurons (neurons where G3BP1 signal met the binary thresholding
1092 requirements) were counted and percentage of cells with SGs over total number of cells was
1093 obtained per each image. SGs per cell values were obtained using the counting tool in NIS
1094 Elements only on neurons that were determined to be SG+. SG area and FUS signal intensity
1095 was obtained after the binary layer was applied to each image. iPSC image quantifications were
1096 analyzed by two-way ANOVA test with FUS genotype (WT and mutant) and Oligo treatment
1097 (vehicle, RNA C2 and RNA S1) as variables. Viability assay was analyzed by one-way
1098 ANOVA. Significance was set at 0.05 and post-hoc pairwise comparisons with the Bonferroni
1099 correction were used for analysis of specific differences in any cases where interactions were
1100 significant.

1101

1102 **Detergent solubility fractionation**

1103 For assessment of relative optoFUS and ssTDP43 detergent solubility, cell lysate fractionation
1104 was performed as described¹⁵ with minor modifications. Briefly, cells were first lysed with RIPA
1105 buffer (25mM Tris-HCl pH 7.6, 150mM NaCl, 2mM EDTA, 1% NP-40, 1% sodium
1106 deoxycholate, 0.1% SDS) supplemented with cOmplete Protease Inhibitor Cocktail (Roche) and

1107 phosphatase inhibitor cocktails 2/3 (Sigma-Aldrich) following one wash in ice-cold PBS. After
1108 brief sonication (five 3s pulses at 30% amplitude), lysates were then centrifuged at 17,000g at
1109 4°C for 45min and the resulting supernatant was collected as the RIPA-soluble fraction. Protein
1110 concentration was determined using the Pierce BCA assay (Thermo Fisher Scientific). Pellets
1111 were then washed in RIPA buffer prior to re-centrifugation at 17,000g at 4°C for 45min. The
1112 resulting supernatants were then discarded, and pellets were re-suspended in urea buffer (30mM
1113 TrisHCl pH 8.5, 7M urea, 2M thiourea, 4% CHAPS) supplemented with cOmplete Protease
1114 Inhibitor Cocktail (Roche) and phosphatase inhibitor cocktails 2/3 (Sigma-Aldrich) and
1115 sonicated briefly prior to centrifugation at 17,000g at room temperature ($\sim 23^{\circ}\text{C} \pm 2^{\circ}\text{C}$). The
1116 resulting supernatant was then collected as the RIPA-insoluble, urea soluble fraction and samples
1117 were separated by SDS-PAGE prior to western blot analysis.

1118

1119 **SDS-PAGE/Western blotting**

1120 Prior to SDS-PAGE, samples were first diluted in 4X Laemmli sample buffer (Bio-Rad)
1121 supplemented with 2-mercaptoethanol (Bio-Rad) and heated at 70°C for 10-15min. Samples
1122 were then loaded into 12% or 4-20% Mini-PROTEAN TGX Precast gels (Bio-Rad) and
1123 separated by SDS-PAGE. Separated samples were next transferred to PVDF membranes (Bio-
1124 Rad) prior to washing (TBS) and blocking with Odyssey Blocking Buffer (Li-Cor). Membranes
1125 were then incubated with primary antibodies diluted in Odyssey Blocking Buffer supplemented
1126 with 0.2% Tween-20 overnight at 4°C. Primary antibody dilutions consisted of: mouse anti-
1127 mCherry (Novus Biologicals, 1:1000), rabbit anti-mCherry (Abcam, 1:1000), rabbit anti-FUS
1128 (Proteintech, 1:1000), rabbit anti-TDP43 (Proteintech, 1:1000), mouse anti- α -tubulin (Sigma,
1129 1:10000). The next day, membranes were washed with TBS-T (0.1% Tween-20) and incubated
1130 with secondary antibodies (Li-Cor, IRDye 680/800, 1:10000) for 1h at room temperature
1131 ($\sim 23^{\circ}\text{C} \pm 2^{\circ}\text{C}$) prior to TBS-T washes and imaging (Odyssey CLx imaging system).

1132

1133 **Immunofluorescence**

1134 For immunofluorescent characterization of optoFUS and ssTDP43 inclusions, cells seeded onto
1135 collagen-coated coverslips (Thermo Fisher, 50 $\mu\text{g}/\text{mL}$) were first fixed for 15min at room
1136 temperature ($\sim 23^{\circ}\text{C} \pm 2^{\circ}\text{C}$) in 4% PFA following one PBS wash. Three additional PBS washes
1137 were then performed prior to a 1h incubation in blocking buffer (0.3% TX-100/5% NDS in PBS)

1138 at room temperature ($\sim 23^{\circ}\text{C} \pm 2^{\circ}\text{C}$). Cells were then incubated overnight at 4°C with primary
1139 antibodies diluted in blocking buffer at the following concentrations: rabbit anti-TAF15/TAFII68
1140 (Bethyl Labs, 1:500), mouse anti-EWSR1 (Santa Cruz, 1:200), rat anti-methylated TLS/FUS
1141 (Clone 9G6, Sigma-Aldrich, 1:100), guinea pig anti-MAP2 (Synaptic Systems, 1:1000), rabbit
1142 anti-G3BP1 (Proteintech, 1:500), rat anti-phospho-TDP43 (S409/410) (Clone 1D3, Biolegend,
1143 1:200), rabbit anti-SQSTM1/p62 (Abcam, 1:500). The following day, primary antibodies were
1144 removed, and cells were exposed to three PBS washes prior to a 1h incubation with secondary
1145 antibodies (AlexaFluor 488/594/647, 1:1000) diluted in blocking buffer at room temperature
1146 ($\sim 23^{\circ}\text{C} \pm 2^{\circ}\text{C}$). Three additional PBS washes were then performed prior to mounting coverslips
1147 onto slides using ProLong Diamond Antifade Mountant with DAPI (Invitrogen). Slides were
1148 allowed to cure overnight prior to visualization by confocal microscopy.

1149

1150 **Live-cell imaging**

1151 Live-cell imaging experiments were performed on a Nikon Eclipse Ti2 inverted microscope
1152 equipped with an X-Light V2 (CrestOptics) spinning disk unit using CFI Plan Apo Lambda 40X
1153 dry or CFI Plan Apo VC 60X water immersion objectives (Nikon) and a Prime 95B CMOS
1154 camera (Photometrics). Cells were maintained at 37°C and 5% CO_2 in a Tokai HIT STX
1155 stagetop incubator throughout the imaging process. For chronic stimulation paradigms, wells
1156 were illuminated ($\sim 0.1\text{-}0.3\text{mW}$, 465nm) using custom-built 6-well, 24-well, 96-well LED panels
1157 designed to sit atop the plates in between image acquisition periods using a 5V analog output
1158 from a Texas Instruments BNC-2110 triggering device as described.¹⁵ For acute LIPS
1159 experiments, cells expressing iLID cores along with FUS-mCh-SspB mutants were first imaged
1160 using only the 594nm laser line to establish baseline FUS-SspB fluorescence intensity and
1161 spontaneous condensate assembly. Acute activation sequences (30s or less) were then achieved
1162 through dual-channel imaging with the 594nm and 488nm (75% power) laser lines, followed by
1163 post-activation image sequences for up to 10min acquired using only 594nm lasers to avoid
1164 further activation.

1165

1166 **Fluorescence recovery after photo-bleaching (FRAP) imaging and analysis**

1167 For FRAP analysis of optoFUS and ssTDP43 assemblies, cells expressing these constructs were
1168 first imaged prior to light activation of optogenetic proteins to acquire baseline fluorescence

1169 recovery rates due to diffusion. Cells were then exposed to light activation for the indicated times
1170 and relative dynamics of light-induced condensates/inclusions were determined by FRAP. All
1171 imaging was performed on a Nikon A1 laser-scanning confocal microscope utilizing a 60X oil
1172 immersion objective (Nikon, CFI Plan Apo Lambda 60X Oil) and Tokai HIT stagetop incubator
1173 to maintain cells at 37°C and 5% CO₂. In brief, 2µm diameter bleaching regions-of-interest
1174 (ROIs) were drawn within nuclear compartments (for dark or pre-activation conditions) or
1175 around light-induced assemblies. 2-3 baseline images were then acquired prior to photo-
1176 bleaching within bleaching ROIs using the 488nm laser line (500ms, 50% power). Post-
1177 bleaching image sequences were then acquired for up to five minutes and fluorescence recovery
1178 within bleaching ROIs was measured over time. Fluorescence intensity values were normalized
1179 to intensities within reference ROIs of the same size drawn in non-bleached cells to control for
1180 fluorescence loss resulting from post-bleach imaging. These values were then normalized to each
1181 ROI's minimum and maximum intensities and were plotted as mean recovery rates per condition.

1182

1183 **Automated image analysis**

1184 All automated image analysis was performed in NIS-Elements Advanced Research software
1185 (Nikon) using built-in analysis packages. For analysis of FUS-SspB condensate formation
1186 following acute light activation protocols, individual ROIs were first drawn around all cells
1187 expressing both iLID cores and FUS-SspB mutant constructs in each field-of-view. Baseline
1188 FUS-SspB fluorescence intensity was determined in frames prior to light activation. Automated
1189 Spot Detection was then used to identify and quantify the number of FUS-SspB droplets within
1190 each ROI during and following light activation sequences and the Time Measurement tool was
1191 used to export the number of objects per cell over time to Microsoft Excel. Object number values
1192 were then normalized to baseline values (prior to light activation), weighted based on baseline
1193 FUS-SspB fluorescence intensity (compared to population mean), and plotted over time. For
1194 graphs comparing threshold FUS-SspB concentrations required for LIPS, baseline fluorescence
1195 values were plotted against the maximum number of objects observed in each individual cell
1196 over the time-course of the experiment. C_{thresh} values were determined by calculating the mean
1197 baseline fluorescence intensity of the five lowest-expressing cells in each mutant condition that
1198 underwent LIPS (defined as the formation of >10 condensates in response to light activation).
1199 For quantification of condensate dissociation kinetics, the number of objects identified in each

1200 individual cell in the first frame following light removal (T_0) was set at 100% and values in each
1201 successive frame were normalized as a percentage of initial T_0 values and mean dissociation
1202 values were plotted over time. One-phase exponential decay curves were then fit and $T_{1/2}$ values
1203 for each FUS-SspB mutant were determined using Graphpad Prism 8 software.

1204

1205 For automated analysis of optoFUS normalized aggregation area, individual z-stacks were
1206 acquired in 9-16 randomized fields-of-view and maximum intensity projections were generated
1207 for analysis. First, binaries for cell nuclei and optoFUS inclusions were generated through
1208 fluorescence intensity thresholding of DAPI and mCherry signals respectively (Figure S7A-H).
1209 Binary subtraction operations were then performed to generate a new binary layer consisting of
1210 mCherry signal with nuclear signal subtracted to remove confounding nuclear optoFUS signal
1211 from analysis. The total area of this resulting binary layer (optoFUS inclusions only) was then
1212 calculated and normalized to total optoFUS cell area (determined by cell masks based upon
1213 mCherry fluorescence) and was presented as normalized aggregation area. Mean aggregation
1214 area values were then determined across fields-of-view and plotted as fold-change from control.

1215

1216 For automated quantification of light-induced formation of ssTDP43 inclusions, maximum
1217 intensity projections were first generated from z-stacks acquired over at least 6 individual fields-
1218 of-view per condition. Automated Spot Detection was then utilized to identify and quantify the
1219 number of light-induced condensates per field-of-view over time. These values were then
1220 normalized to baseline (prior to light activation) values and plotted as mean increase from
1221 baseline over the course of light stimulation. For quantification of ssTDP43 and optoFUS
1222 inclusion disassembly, individual inclusions from 6-8 fields-of-view were identified and tracked
1223 over time. Here, baseline inclusion area was first determined through automatically or manually
1224 drawn ROIs in the first frame acquired following RNA treatments (T_0). ROI areas were then
1225 determined for subsequent frames every 2h for up to 10h, normalized to baseline values and
1226 presented as fold change from T_0 over time. Survival of these inclusion-bearing cells was also
1227 manually tracked, and Graphpad Prism 8 was used to generate and compare Kaplan–Meier
1228 survival curves between treatment groups. All above analyses were performed blinded.

1229

1230 **Minigene and splicing assays**

1231 For monitoring of TDP-43 splicing function, the CFTR exon 9 minigene assay was performed as
1232 previously described⁷⁹ with minor modifications. In brief, HEK293 cells transfected with the
1233 CFTR minigene plasmid were treated with siRNA (25nM) or RNA inhibitor oligonucleotides
1234 (2.5µM) for 72h prior to cell lysis and RNA extraction using the miRNA Easy Kit (Qiagen). The
1235 iScript cDNA Synthesis Kit (Bio-Rad) was then used to generate cDNA from RNA samples and
1236 PCR reactions were then performed using cDNA templates and primers flanking exon 9 of the
1237 CFTR minigene⁷⁹ prior to separation on a 1% agarose gel. Primer sequences are as follows: Fwd:
1238 5'-CAACTTCAAGCTCGTAAGCCACTGC-3'; Rev: 5'-
1239 TAGGATCCGGTCACCAGGAAGTTGGTTAAATCA-3'. Bands were then visualized and
1240 imaged using the Chemidoc MP Imaging System (Bio-Rad).

1241

1242 **QUANTIFICATION AND STATISTICAL ANALYSIS**

1243 Quantification is as described in the figure legends. Statistical analyses were performed using the
1244 GraphPad Prism (GraphPad Software, Inc.; La Jolla, CA, USA) as described in figure legends.

1245

1246 **References**

- 1247 1. Portz, B., Lee, B.L., and Shorter, J. (2021). FUS and TDP-43 Phases in Health and Disease.
1248 *Trends Biochem Sci* 46, 550-563. 10.1016/j.tibs.2020.12.005.
- 1249 2. Huang, E.J., Zhang, J., Geser, F., Trojanowski, J.Q., Strober, J.B., Dickson, D.W., Brown,
1250 R.H., Jr., Shapiro, B.E., and Lomen-Hoerth, C. (2010). Extensive FUS-immunoreactive
1251 pathology in juvenile amyotrophic lateral sclerosis with basophilic inclusions. *Brain Pathol*
1252 20, 1069-1076. 10.1111/j.1750-3639.2010.00413.x.
- 1253 3. Arseni, D., Hasegawa, M., Murzin, A.G., Kametani, F., Arai, M., Yoshida, M., and
1254 Ryskeldi-Falcon, B. (2022). Structure of pathological TDP-43 filaments from ALS with
1255 FTL. *Nature* 601, 139-143. 10.1038/s41586-021-04199-3.
- 1256 4. Neumann, M., Sampathu, D.M., Kwong, L.K., Truax, A.C., Micsenyi, M.C., Chou, T.T.,
1257 Bruce, J., Schuck, T., Grossman, M., Clark, C.M., et al. (2006). Ubiquitinated TDP-43 in
1258 frontotemporal lobar degeneration and amyotrophic lateral sclerosis. *Science* 314, 130-133.
1259 10.1126/science.1134108.
- 1260 5. Vance, C., Rogelj, B., Hortobagyi, T., De Vos, K.J., Nishimura, A.L., Sreedharan, J., Hu,
1261 X., Smith, B., Ruddy, D., Wright, P., et al. (2009). Mutations in FUS, an RNA processing
1262 protein, cause familial amyotrophic lateral sclerosis type 6. *Science* 323, 1208-1211.
1263 10.1126/science.1165942.
- 1264 6. Kwiatkowski, T.J., Jr., Bosco, D.A., Leclerc, A.L., Tamrazian, E., Vanderburg, C.R., Russ,
1265 C., Davis, A., Gilchrist, J., Kasarskis, E.J., Munsat, T., et al. (2009). Mutations in the
1266 FUS/TLS gene on chromosome 16 cause familial amyotrophic lateral sclerosis. *Science*
1267 323, 1205-1208. 10.1126/science.1166066.
- 1268 7. Arseni, D., Chen, R., Murzin, A.G., Peak-Chew, S.Y., Garringer, H.J., Newell, K.L.,
1269 Kametani, F., Robinson, A.C., Vidal, R., Ghetti, B., Hasegawa, M., and Ryskeldi-Falcon,
1270 B. (2023). TDP-43 forms amyloid filaments with a distinct fold in type A FTL. *Nature*.
1271 10.1038/s41586-023-06405-w.
- 1272 8. Guo, L., Kim, H.J., Wang, H., Monaghan, J., Freyermuth, F., Sung, J.C., O'Donovan, K.,
1273 Fare, C.M., Diaz, Z., Singh, N., et al. (2018). Nuclear-Import Receptors Reverse Aberrant
1274 Phase Transitions of RNA-Binding Proteins with Prion-like Domains. *Cell* 173, 677-692
1275 e620. 10.1016/j.cell.2018.03.002.
- 1276 9. Johnson, B.S., Snead, D., Lee, J.J., McCaffery, J.M., Shorter, J., and Gitler, A.D. (2009).
1277 TDP-43 is intrinsically aggregation-prone, and amyotrophic lateral sclerosis-linked
1278 mutations accelerate aggregation and increase toxicity. *J Biol Chem* 284, 20329-20339.
1279 10.1074/jbc.M109.010264.
- 1280 10. Sun, Z., Diaz, Z., Fang, X., Hart, M.P., Chesi, A., Shorter, J., and Gitler, A.D. (2011).
1281 Molecular determinants and genetic modifiers of aggregation and toxicity for the ALS
1282 disease protein FUS/TLS. *PLoS Biol* 9, e1000614. 10.1371/journal.pbio.1000614.

- 1283 11. Patel, A., Lee, H.O., Jawerth, L., Maharana, S., Jahnel, M., Hein, M.Y., Stoykov, S.,
1284 Mahamid, J., Saha, S., Franzmann, T.M., et al. (2015). A Liquid-to-Solid Phase Transition
1285 of the ALS Protein FUS Accelerated by Disease Mutation. *Cell* 162, 1066-1077.
1286 10.1016/j.cell.2015.07.047.
- 1287 12. Gasset-Rosa, F., Lu, S., Yu, H., Chen, C., Melamed, Z., Guo, L., Shorter, J., Da Cruz, S.,
1288 and Cleveland, D.W. (2019). Cytoplasmic TDP-43 De-mixing Independent of Stress
1289 Granules Drives Inhibition of Nuclear Import, Loss of Nuclear TDP-43, and Cell Death.
1290 *Neuron* 102, 339-357 e337. 10.1016/j.neuron.2019.02.038.
- 1291 13. Hallegger, M., Chakrabarti, A.M., Lee, F.C.Y., Lee, B.L., Amaliotti, A.G., Odeh, H.M.,
1292 Copley, K.E., Rubien, J.D., Portz, B., Kuret, K., et al. (2021). TDP-43 condensation
1293 properties specify its RNA-binding and regulatory repertoire. *Cell* 184, 4680-4696 e4622.
1294 10.1016/j.cell.2021.07.018.
- 1295 14. Levone, B.R., Lenzken, S.C., Antonaci, M., Maiser, A., Rapp, A., Conte, F., Reber, S.,
1296 Mechttersheimer, J., Ronchi, A.E., Muhlemann, O., et al. (2021). FUS-dependent liquid-
1297 liquid phase separation is important for DNA repair initiation. *J Cell Biol* 220.
1298 10.1083/jcb.202008030.
- 1299 15. Mann, J.R., Gleixner, A.M., Mauna, J.C., Gomes, E., DeChellis-Marks, M.R., Needham,
1300 P.G., Copley, K.E., Hurtle, B., Portz, B., Pyles, N.J., et al. (2019). RNA Binding
1301 Antagonizes Neurotoxic Phase Transitions of TDP-43. *Neuron* 102, 321-338 e328.
1302 10.1016/j.neuron.2019.01.048.
- 1303 16. Zhang, P., Fan, B., Yang, P., Temirov, J., Messing, J., Kim, H.J., and Taylor, J.P. (2019).
1304 Chronic optogenetic induction of stress granules is cytotoxic and reveals the evolution of
1305 ALS-FTD pathology. *Elife* 8. 10.7554/eLife.39578.
- 1306 17. Shorter, J. (2017). Designer protein disaggregases to counter neurodegenerative disease.
1307 *Curr Opin Genet Dev* 44, 1-8. 10.1016/j.gde.2017.01.008.
- 1308 18. Jackrel, M.E., DeSantis, M.E., Martinez, B.A., Castellano, L.M., Stewart, R.M., Caldwell,
1309 K.A., Caldwell, G.A., and Shorter, J. (2014). Potentiated Hsp104 variants antagonize
1310 diverse proteotoxic misfolding events. *Cell* 156, 170-182. 10.1016/j.cell.2013.11.047.
- 1311 19. Khalil, B., Chhangani, D., Wren, M.C., Smith, C.L., Lee, J.H., Li, X., Puttinger, C., Tsai,
1312 C.W., Fortin, G., Morderer, D., et al. (2022). Nuclear import receptors are recruited by FG-
1313 nucleoporins to rescue hallmarks of TDP-43 proteinopathy. *Mol Neurodegener* 17, 80.
1314 10.1186/s13024-022-00585-1.
- 1315 20. Goertsen, D., Flytzanis, N.C., Goeden, N., Chuapoco, M.R., Cummins, A., Chen, Y., Fan,
1316 Y., Zhang, Q., Sharma, J., Duan, Y., et al. (2022). AAV capsid variants with brain-wide
1317 transgene expression and decreased liver targeting after intravenous delivery in mouse and
1318 marmoset. *Nat Neurosci* 25, 106-115. 10.1038/s41593-021-00969-4.

- 1319 21. Ly, C.V., and Miller, T.M. (2018). Emerging antisense oligonucleotide and viral therapies
1320 for amyotrophic lateral sclerosis. *Curr Opin Neurol* 31, 648-654.
1321 10.1097/WCO.0000000000000594.
- 1322 22. Bennett, C.F., Krainer, A.R., and Cleveland, D.W. (2019). Antisense Oligonucleotide
1323 Therapies for Neurodegenerative Diseases. *Annu Rev Neurosci* 42, 385-406.
1324 10.1146/annurev-neuro-070918-050501.
- 1325 23. Glasel, J.A. (1995). Validity of nucleic acid purities monitored by 260nm/280nm
1326 absorbance ratios. *Biotechniques* 18, 62-63.
- 1327 24. Lerga, A., Hallier, M., Delva, L., Orvain, C., Gallais, I., Marie, J., and Moreau-Gachelin,
1328 F. (2001). Identification of an RNA binding specificity for the potential splicing factor TLS.
1329 *J Biol Chem* 276, 6807-6816. 10.1074/jbc.M008304200.
- 1330 25. Buratti, E., and Baralle, F.E. (2001). Characterization and functional implications of the
1331 RNA binding properties of nuclear factor TDP-43, a novel splicing regulator of CFTR exon
1332 9. *J Biol Chem* 276, 36337-36343. 10.1074/jbc.M104236200.
- 1333 26. Qiu, H., Lee, S., Shang, Y., Wang, W.Y., Au, K.F., Kamiya, S., Barmada, S.J., Finkbeiner,
1334 S., Lui, H., Carlton, C.E., et al. (2014). ALS-associated mutation FUS-R521C causes DNA
1335 damage and RNA splicing defects. *J Clin Invest* 124, 981-999. 10.1172/JCI72723.
- 1336 27. Schwartz, J.C., Wang, X., Podell, E.R., and Cech, T.R. (2013). RNA seeds higher-order
1337 assembly of FUS protein. *Cell Rep* 5, 918-925. 10.1016/j.celrep.2013.11.017.
- 1338 28. Lagier-Tourenne, C., Polymenidou, M., Hutt, K.R., Vu, A.Q., Baughn, M., Huelga, S.C.,
1339 Clutario, K.M., Ling, S.C., Liang, T.Y., Mazur, C., et al. (2012). Divergent roles of ALS-
1340 linked proteins FUS/TLS and TDP-43 intersect in processing long pre-mRNAs. *Nat*
1341 *Neurosci* 15, 1488-1497. 10.1038/nn.3230.
- 1342 29. Murakami, T., Qamar, S., Lin, J.Q., Schierle, G.S., Rees, E., Miyashita, A., Costa, A.R.,
1343 Dodd, R.B., Chan, F.T., Michel, C.H., et al. (2015). ALS/FTD Mutation-Induced Phase
1344 Transition of FUS Liquid Droplets and Reversible Hydrogels into Irreversible Hydrogels
1345 Impairs RNP Granule Function. *Neuron* 88, 678-690. 10.1016/j.neuron.2015.10.030.
- 1346 30. Harrison, A.F., and Shorter, J. (2017). RNA-binding proteins with prion-like domains in
1347 health and disease. *Biochem J* 474, 1417-1438. 10.1042/BCJ20160499.
- 1348 31. Niaki, A.G., Sarkar, J., Cai, X., Rhine, K., Vidaurre, V., Guy, B., Hurst, M., Lee, J.C., Koh,
1349 H.R., Guo, L., et al. (2020). Loss of Dynamic RNA Interaction and Aberrant Phase
1350 Separation Induced by Two Distinct Types of ALS/FTD-Linked FUS Mutations. *Mol Cell*
1351 77, 82-94 e84. 10.1016/j.molcel.2019.09.022.
- 1352 32. Roy, R., Hohng, S., and Ha, T. (2008). A practical guide to single-molecule FRET. *Nat*
1353 *Methods* 5, 507-516. 10.1038/nmeth.1208.

- 1354 33. Loughlin, F.E., Lukavsky, P.J., Kazeeva, T., Reber, S., Hock, E.M., Colombo, M., Von
1355 Schroetter, C., Pauli, P., Clery, A., Muhlemann, O., et al. (2019). The Solution Structure
1356 of FUS Bound to RNA Reveals a Bipartite Mode of RNA Recognition with Both Sequence
1357 and Shape Specificity. *Mol Cell* 73, 490-504 e496. 10.1016/j.molcel.2018.11.012.
- 1358 34. Daigle, J.G., Lanson, N.A., Jr., Smith, R.B., Casci, I., Maltare, A., Monaghan, J., Nichols,
1359 C.D., Kryndushkin, D., Shewmaker, F., and Pandey, U.B. (2013). RNA-binding ability of
1360 FUS regulates neurodegeneration, cytoplasmic mislocalization and incorporation into
1361 stress granules associated with FUS carrying ALS-linked mutations. *Hum Mol Genet* 22,
1362 1193-1205. 10.1093/hmg/dds526.
- 1363 35. Burke, K.A., Janke, A.M., Rhine, C.L., and Fawzi, N.L. (2015). Residue-by-Residue View
1364 of In Vitro FUS Granules that Bind the C-Terminal Domain of RNA Polymerase II. *Mol*
1365 *Cell* 60, 231-241. 10.1016/j.molcel.2015.09.006.
- 1366 36. Iko, Y., Kodama, T.S., Kasai, N., Oyama, T., Morita, E.H., Muto, T., Okumura, M., Fujii,
1367 R., Takumi, T., Tate, S., and Morikawa, K. (2004). Domain architectures and
1368 characterization of an RNA-binding protein, TLS. *J Biol Chem* 279, 44834-44840.
1369 10.1074/jbc.M408552200.
- 1370 37. Bogaert, E., Boeynaems, S., Kato, M., Guo, L., Caulfield, T.R., Steyaert, J., Scheveneels,
1371 W., Wilmans, N., Haeck, W., Hersmus, N., et al. (2018). Molecular Dissection of FUS
1372 Points at Synergistic Effect of Low-Complexity Domains in Toxicity. *Cell Rep* 24, 529-
1373 537 e524. 10.1016/j.celrep.2018.06.070.
- 1374 38. Maharana, S., Wang, J., Papadopoulos, D.K., Richter, D., Pozniakovsky, A., Poser, I.,
1375 Bickle, M., Rizk, S., Guillén-Boixet, J., Franzmann, T.M., et al. (2018). RNA buffers the
1376 phase separation behavior of prion-like RNA binding proteins. *Science* 360, 918-921.
1377 10.1126/science.aar7366.
- 1378 39. Bracha, D., Walls, M.T., Wei, M.T., Zhu, L., Kurian, M., Avalos, J.L., Toettcher, J.E., and
1379 Brangwynne, C.P. (2018). Mapping Local and Global Liquid Phase Behavior in Living
1380 Cells Using Photo-Oligomerizable Seeds. *Cell* 175, 1467-1480.e1413.
1381 10.1016/j.cell.2018.10.048.
- 1382 40. Hofweber, M., Hutten, S., Bourgeois, B., Spreitzer, E., Niedner-Boblenz, A., Schifferer,
1383 M., Ruepp, M.D., Simons, M., Niessing, D., Madl, T., and Dormann, D. (2018). Phase
1384 Separation of FUS Is Suppressed by Its Nuclear Import Receptor and Arginine Methylation.
1385 *Cell* 173, 706-719.e713. 10.1016/j.cell.2018.03.004.
- 1386 41. Qamar, S., Wang, G., Randle, S.J., Ruggeri, F.S., Varela, J.A., Lin, J.Q., Phillips, E.C.,
1387 Miyashita, A., Williams, D., Ströhl, F., et al. (2018). FUS Phase Separation Is Modulated
1388 by a Molecular Chaperone and Methylation of Arginine Cation- π Interactions. *Cell* 173,
1389 720-734.e715. 10.1016/j.cell.2018.03.056.
- 1390 42. Yoshizawa, T., Ali, R., Jiou, J., Fung, H.Y.J., Burke, K.A., Kim, S.J., Lin, Y., Peeples,
1391 W.B., Saltzberg, D., Soniat, M., et al. (2018). Nuclear Import Receptor Inhibits Phase

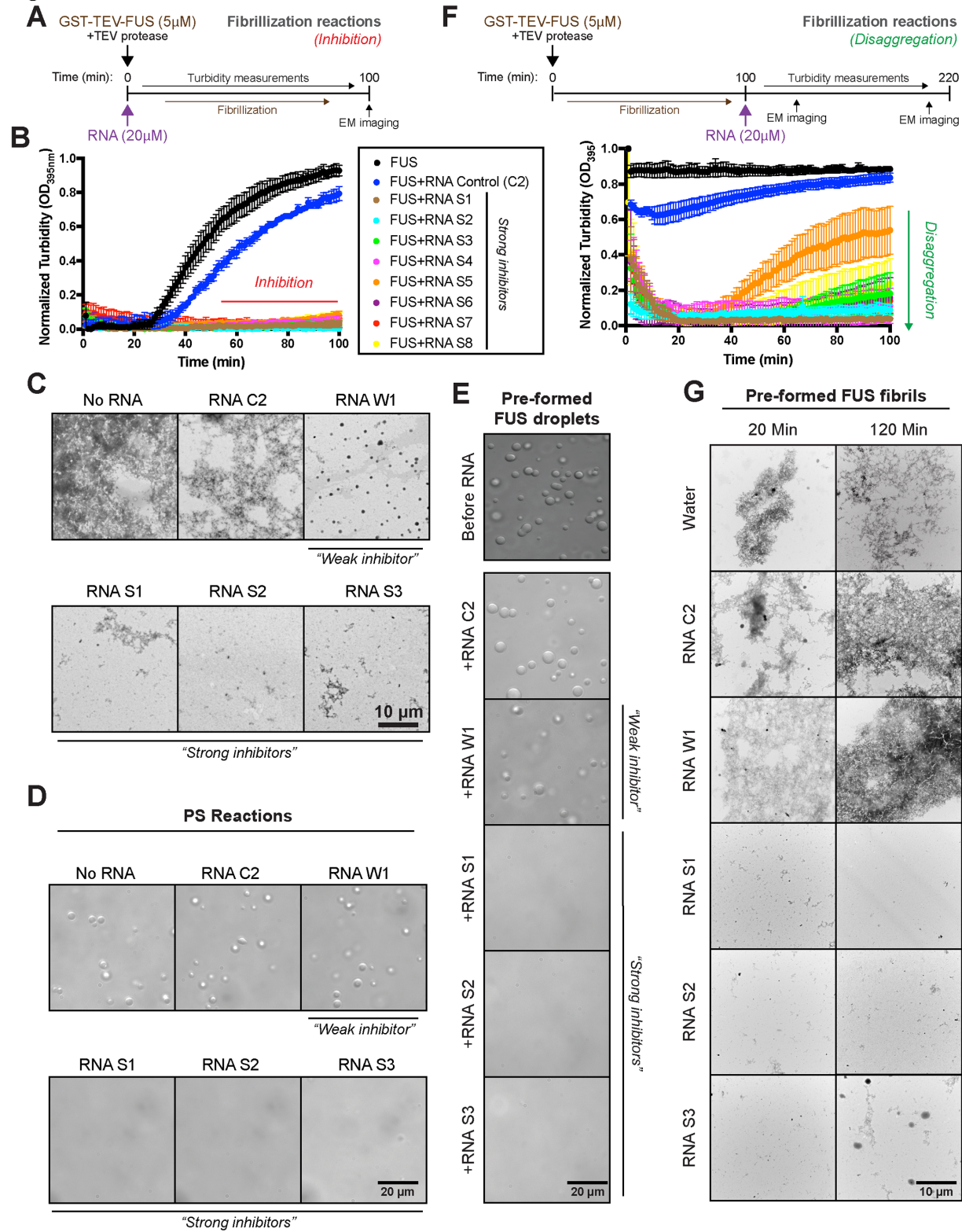
- 1392 Separation of FUS through Binding to Multiple Sites. *Cell* *173*, 693-705.e622.
1393 10.1016/j.cell.2018.03.003.
- 1394 43. Fare, C.M., Rhine, K., Lam, A., Myong, S., and Shorter, J. (2023). A minimal construct of
1395 nuclear-import receptor Karyopherin-beta2 defines the regions critical for chaperone and
1396 disaggregation activity. *J Biol Chem* *299*, 102806. 10.1016/j.jbc.2022.102806.
- 1397 44. Taslimi, A., Vrana, J.D., Chen, D., Borinskaya, S., Mayer, B.J., Kennedy, M.J., and Tucker,
1398 C.L. (2014). An optimized optogenetic clustering tool for probing protein interaction and
1399 function. *Nat Commun* *5*, 4925. 10.1038/ncomms5925.
- 1400 45. Neumann, M., Bentmann, E., Dormann, D., Jawaid, A., DeJesus-Hernandez, M., Ansorge,
1401 O., Roeber, S., Kretzschmar, H.A., Munoz, D.G., Kusaka, H., et al. (2011). FET proteins
1402 TAF15 and EWS are selective markers that distinguish FTLD with FUS pathology from
1403 amyotrophic lateral sclerosis with FUS mutations. *Brain* *134*, 2595-2609.
1404 10.1093/brain/awr201.
- 1405 46. Neumann, M., Valori, C.F., Ansorge, O., Kretzschmar, H.A., Munoz, D.G., Kusaka, H.,
1406 Yokota, O., Ishihara, K., Ang, L.C., Bilbao, J.M., and Mackenzie, I.R. (2012). Transportin
1407 1 accumulates specifically with FET proteins but no other transportin cargos in FTLD-FUS
1408 and is absent in FUS inclusions in ALS with FUS mutations. *Acta Neuropathol* *124*, 705-
1409 716. 10.1007/s00401-012-1020-6.
- 1410 47. Mackenzie, I.R., Rademakers, R., and Neumann, M. (2010). TDP-43 and FUS in
1411 amyotrophic lateral sclerosis and frontotemporal dementia. *Lancet Neurol* *9*, 995-1007.
1412 10.1016/S1474-4422(10)70195-2.
- 1413 48. Dormann, D., Madl, T., Valori, C.F., Bentmann, E., Tahirovic, S., Abou-Ajram, C.,
1414 Kremmer, E., Ansorge, O., Mackenzie, I.R., Neumann, M., and Haass, C. (2012). Arginine
1415 methylation next to the PY-NLS modulates Transportin binding and nuclear import of FUS.
1416 *EMBO J* *31*, 4258-4275. 10.1038/emboj.2012.261.
- 1417 49. Haeusler, A.R., Donnelly, C.J., Periz, G., Simko, E.A., Shaw, P.G., Kim, M.S., Maragakis,
1418 N.J., Troncoso, J.C., Pandey, A., Sattler, R., Rothstein, J.D., and Wang, J. (2014). C9orf72
1419 nucleotide repeat structures initiate molecular cascades of disease. *Nature* *507*, 195-200.
1420 10.1038/nature13124.
- 1421 50. Couthouis, J., Hart, M.P., Erion, R., King, O.D., Diaz, Z., Nakaya, T., Ibrahim, F., Kim,
1422 H.J., Mojsilovic-Petrovic, J., Panossian, S., et al. (2012). Evaluating the role of the
1423 FUS/TLS-related gene EWSR1 in amyotrophic lateral sclerosis. *Hum Mol Genet* *21*, 2899-
1424 2911. 10.1093/hmg/dds116.
- 1425 51. Couthouis, J., Hart, M.P., Shorter, J., DeJesus-Hernandez, M., Erion, R., Oristano, R., Liu,
1426 A.X., Ramos, D., Jethava, N., Hosangadi, D., et al. (2011). A yeast functional screen
1427 predicts new candidate ALS disease genes. *Proc Natl Acad Sci U S A* *108*, 20881-20890.
1428 10.1073/pnas.1109434108.

- 1429 52. Kim, H.J., Kim, N.C., Wang, Y.D., Scarborough, E.A., Moore, J., Diaz, Z., MacLea, K.S.,
1430 Freibaum, B., Li, S., Molliex, A., et al. (2013). Mutations in prion-like domains in
1431 hnRNPA2B1 and hnRNPA1 cause multisystem proteinopathy and ALS. *Nature* *495*, 467-
1432 473. 10.1038/nature11922.
- 1433 53. Beijer, D., Kim, H.J., Guo, L., O'Donovan, K., Mademan, I., Deconinck, T., Van Schil, K.,
1434 Fare, C.M., Drake, L.E., Ford, A.F., et al. (2021). Characterization of HNRNPA1
1435 mutations defines diversity in pathogenic mechanisms and clinical presentation. *JCI*
1436 *Insight* *6*. 10.1172/jci.insight.148363.
- 1437 54. Kim, H.J., Mohassel, P., Donkervoort, S., Guo, L., O'Donovan, K., Coughlin, M., Lornage,
1438 X., Foulds, N., Hammans, S.R., Foley, A.R., et al. (2022). Heterozygous frameshift
1439 variants in HNRNPA2B1 cause early-onset oculopharyngeal muscular dystrophy. *Nat*
1440 *Commun* *13*, 2306. 10.1038/s41467-022-30015-1.
- 1441 55. Ayala, Y.M., De Conti, L., Avendaño-Vázquez, S.E., Dhir, A., Romano, M., D'Ambrogio,
1442 A., Tollervey, J., Ule, J., Baralle, M., Buratti, E., and Baralle, F.E. (2011). TDP-43
1443 regulates its mRNA levels through a negative feedback loop. *EMBO J* *30*, 277-288.
1444 10.1038/emboj.2010.310.
- 1445 56. Polymenidou, M., Lagier-Tourenne, C., Hutt, K.R., Huelga, S.C., Moran, J., Liang, T.Y.,
1446 Ling, S.C., Sun, E., Wancewicz, E., Mazur, C., et al. (2011). Long pre-mRNA depletion
1447 and RNA missplicing contribute to neuronal vulnerability from loss of TDP-43. *Nat*
1448 *Neurosci* *14*, 459-468. 10.1038/nn.2779.
- 1449 57. Tollervey, J.R., Curk, T., Rogelj, B., Briese, M., Cereda, M., Kayikci, M., Konig, J.,
1450 Hortobagyi, T., Nishimura, A.L., Zupunski, V., et al. (2011). Characterizing the RNA
1451 targets and position-dependent splicing regulation by TDP-43. *Nat Neurosci* *14*, 452-458.
1452 10.1038/nn.2778.
- 1453 58. Grese, Z.R., Bastos, A.C., Mamede, L.D., French, R.L., Miller, T.M., and Ayala, Y.M.
1454 (2021). Specific RNA interactions promote TDP-43 multivalent phase separation and
1455 maintain liquid properties. *EMBO Rep* *22*, e53632. 10.15252/embr.202153632.
- 1456 59. Wang, A., Conicella, A.E., Schmidt, H.B., Martin, E.W., Rhoads, S.N., Reeb, A.N., Nourse,
1457 A., Ramirez Montero, D., Ryan, V.H., Rohatgi, R., et al. (2018). A single N-terminal
1458 phosphomimic disrupts TDP-43 polymerization, phase separation, and RNA splicing.
1459 *EMBO J* *37*. 10.15252/emboj.201797452.
- 1460 60. Conicella, A.E., Zerze, G.H., Mittal, J., and Fawzi, N.L. (2016). ALS Mutations Disrupt
1461 Phase Separation Mediated by alpha-Helical Structure in the TDP-43 Low-Complexity C-
1462 Terminal Domain. *Structure* *24*, 1537-1549. 10.1016/j.str.2016.07.007.
- 1463 61. Babinchak, W.M., Haider, R., Dumm, B.K., Sarkar, P., Surewicz, K., Choi, J.K., and
1464 Surewicz, W.K. (2019). The role of liquid-liquid phase separation in aggregation of the
1465 TDP-43 low-complexity domain. *J Biol Chem* *294*, 6306-6317.
1466 10.1074/jbc.RA118.007222.

- 1467 62. Mayr, C. (2019). What Are 3' UTRs Doing? *Cold Spring Harb Perspect Biol* *11*.
1468 10.1101/cshperspect.a034728.
- 1469 63. Vogler, T.O., Wheeler, J.R., Nguyen, E.D., Hughes, M.P., Britson, K.A., Lester, E., Rao,
1470 B., Betta, N.D., Whitney, O.N., Ewachiw, T.E., et al. (2018). TDP-43 and RNA form
1471 amyloid-like myo-granules in regenerating muscle. *Nature* *563*, 508-513. 10.1038/s41586-
1472 018-0665-2.
- 1473 64. Miller, T.M., Cudkowicz, M.E., Genge, A., Shaw, P.J., Sobue, G., Bucelli, R.C., Chiò, A.,
1474 Van Damme, P., Ludolph, A.C., Glass, J.D., et al. (2022). Trial of Antisense
1475 Oligonucleotide Tofersen for SOD1 ALS. *N Engl J Med* *387*, 1099-1110.
1476 10.1056/NEJMoa2204705.
- 1477 65. Becker, L.A., Huang, B., Bieri, G., Ma, R., Knowles, D.A., Jafar-Nejad, P., Messing, J.,
1478 Kim, H.J., Soriano, A., Auburger, G., et al. (2017). Therapeutic reduction of ataxin-2
1479 extends lifespan and reduces pathology in TDP-43 mice. *Nature* *544*, 367-371.
1480 10.1038/nature22038.
- 1481 66. Korobeynikov, V.A., Lyashchenko, A.K., Blanco-Redondo, B., Jafar-Nejad, P., and
1482 Shneider, N.A. (2022). Antisense oligonucleotide silencing of FUS expression as a
1483 therapeutic approach in amyotrophic lateral sclerosis. *Nat Med* *28*, 104-116.
1484 10.1038/s41591-021-01615-z.
- 1485 67. Takeuchi, T., Maeta, K., Ding, X., Oe, Y., Takeda, A., Inoue, M., Nagano, S., Fujihara, T.,
1486 Matsuda, S., Ishigaki, S., et al. (2023). Sustained therapeutic benefits by transient reduction
1487 of TDP-43 using ENA-modified antisense oligonucleotides in ALS/FTD mice. *Mol Ther*
1488 *Nucleic Acids* *31*, 353-366. 10.1016/j.omtn.2023.01.006.
- 1489 68. Mehta, P.R., Brown, A.L., Ward, M.E., and Fratta, P. (2023). The era of cryptic exons:
1490 implications for ALS-FTD. *Mol Neurodegener* *18*, 16. 10.1186/s13024-023-00608-5.
- 1491 69. Lester, E., Ooi, F.K., Bakkar, N., Ayers, J., Woerman, A.L., Wheeler, J., Bowser, R.,
1492 Carlson, G.A., Prusiner, S.B., and Parker, R. (2021). Tau aggregates are RNA-protein
1493 assemblies that mislocalize multiple nuclear speckle components. *Neuron* *109*, 1675-1691
1494 e1679. 10.1016/j.neuron.2021.03.026.
- 1495 70. Cupo, R.R., and Shorter, J. (2020). Expression and Purification of Recombinant Skd3
1496 (Human ClpB) Protein and Tobacco Etch Virus (TEV) Protease from *Escherichia coli*. *Bio*
1497 *Protoc* *10*, e3858. 10.21769/BioProtoc.3858.
- 1498 71. Gleixner, A.M., Verdone, B.M., Otte, C.G., Anderson, E.N., Ramesh, N., Shapiro, O.R.,
1499 Gale, J.R., Mauna, J.C., Mann, J.R., Copley, K.E., et al. (2022). NUP62 localizes to
1500 ALS/FTLD pathological assemblies and contributes to TDP-43 insolubility. *Nat Commun*
1501 *13*, 3380. 10.1038/s41467-022-31098-6.
- 1502 72. Ziller, M.J., Ortega, J.A., Quinlan, K.A., Santos, D.P., Gu, H., Martin, E.J., Galonska, C.,
1503 Pop, R., Maidl, S., Di Pardo, A., et al. (2018). Dissecting the Functional Consequences of

- 1504 De Novo DNA Methylation Dynamics in Human Motor Neuron Differentiation and
1505 Physiology. *Cell Stem Cell* 22, 559-574 e559. 10.1016/j.stem.2018.02.012.
- 1506 73. Ortega, J.A., Daley, E.L., Kour, S., Samani, M., Tellez, L., Smith, H.S., Hall, E.A., Esengul,
1507 Y.T., Tsai, Y.H., Gendron, T.F., et al. (2020). Nucleocytoplasmic Proteomic Analysis
1508 Uncovers eRF1 and Nonsense-Mediated Decay as Modifiers of ALS/FTD C9orf72
1509 Toxicity. *Neuron* 106, 90-107 e113. 10.1016/j.neuron.2020.01.020.
- 1510 74. Langmead, B., Trapnell, C., Pop, M., and Salzberg, S.L. (2009). Ultrafast and memory-
1511 efficient alignment of short DNA sequences to the human genome. *Genome Biol* 10, R25.
1512 10.1186/gb-2009-10-3-r25.
- 1513 75. Heinz, S., Benner, C., Spann, N., Bertolino, E., Lin, Y.C., Laslo, P., Cheng, J.X., Murre,
1514 C., Singh, H., and Glass, C.K. (2010). Simple combinations of lineage-determining
1515 transcription factors prime cis-regulatory elements required for macrophage and B cell
1516 identities. *Mol Cell* 38, 576-589. 10.1016/j.molcel.2010.05.004.
- 1517 76. Paul, T., Ha, T., and Myong, S. (2021). Regeneration of PEG slide for multiple rounds of
1518 single-molecule measurements. *Biophys J* 120, 1788-1799. 10.1016/j.bpj.2021.02.031.
- 1519 77. Delaglio, F., Grzesiek, S., Vuister, G.W., Zhu, G., Pfeifer, J., and Bax, A. (1995).
1520 NMRPipe: a multidimensional spectral processing system based on UNIX pipes. *J Biomol*
1521 *NMR* 6, 277-293. 10.1007/BF00197809.
- 1522 78. Lee, W., Tonelli, M., and Markley, J.L. (2015). NMRFAM-SPARKY: enhanced software
1523 for biomolecular NMR spectroscopy. *Bioinformatics* 31, 1325-1327.
1524 10.1093/bioinformatics/btu830.
- 1525 79. Pagani, F., Buratti, E., Stuani, C., Romano, M., Zuccato, E., Niksic, M., Giglio, L.,
1526 Faraguna, D., and Baralle, F.E. (2000). Splicing factors induce cystic fibrosis
1527 transmembrane regulator exon 9 skipping through a nonevolutionary conserved intronic
1528 element. *J Biol Chem* 275, 21041-21047. 10.1074/jbc.M910165199.
- 1529 80. Gruber, A.R., Lorenz, R., Bernhart, S.H., Neuböck, R., and Hofacker, I.L. (2008). The
1530 Vienna RNA websuite. *Nucleic Acids Res* 36, W70-74. 10.1093/nar/gkn188.
- 1531 81. Zuker, M. (2003). Mfold web server for nucleic acid folding and hybridization prediction.
1532 *Nucleic Acids Res* 31, 3406-3415. 10.1093/nar/gkg595.
- 1533
- 1534

Figure 1



1535

1536

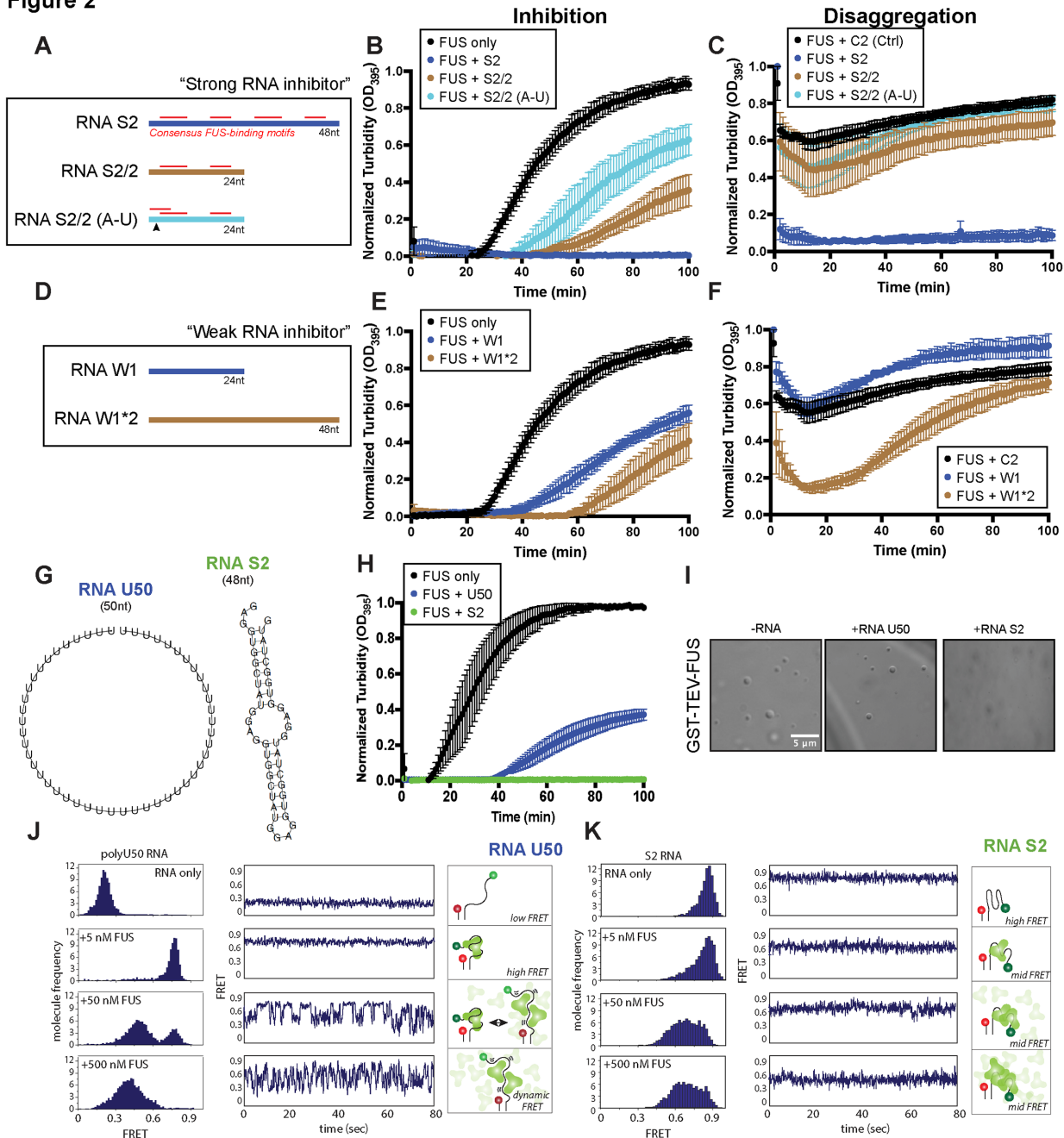
1537

Figure 1. Strong RNA inhibitors inhibit and reverse FUS fibrillization and PS. (A)

Schematic of experiments to test whether RNA oligos inhibit fibrillization. GST-FUS (5 μ M) was

1538 incubated with TEV protease in the presence or absence of RNA oligos (20 μ M) for 0–100min.
1539 Turbidity measurements were taken every minute to assess the extent of fibrillization. Samples
1540 were taken at the end of the reaction to visualize FUS structures via EM. **(B, C)** GST-FUS
1541 (5 μ M) was incubated with TEV protease in the presence or absence of RNA (20 μ M) for 0–
1542 100min. Fibrillization was assessed by turbidity (B) or EM (C). Bar, 10 μ m. Data shown in (B)
1543 are means \pm SEM (n=3). **(D)** GST-FUS (10 μ M) was incubated for 4h in the presence or absence
1544 of the indicated RNA (40 μ M). Droplet formation was assessed by DIC microscopy. Bar, 20 μ m.
1545 **(E)** GST-FUS (10 μ M) droplets were incubated with the indicated RNA (40 μ M) for 10min.
1546 Droplet integrity was assessed by DIC microscopy. Bar, 20 μ m. **(F, G)** Schematic of experiments
1547 to test whether RNA oligos reverse FUS fibrillization. GST-FUS (5 μ M) was incubated with
1548 TEV protease for 100min to form fibrils. At this time, water, or RNA (20 μ M) was added.
1549 Disaggregation was assessed by turbidity (F). Data shown in (F) are means \pm SEM (n=3-4).
1550 Samples were taken after 20min and 120min to visualize FUS structures via EM **(G)**. Bar, 10 μ m.
1551
1552 See also **Figure S1** and **S2**.
1553

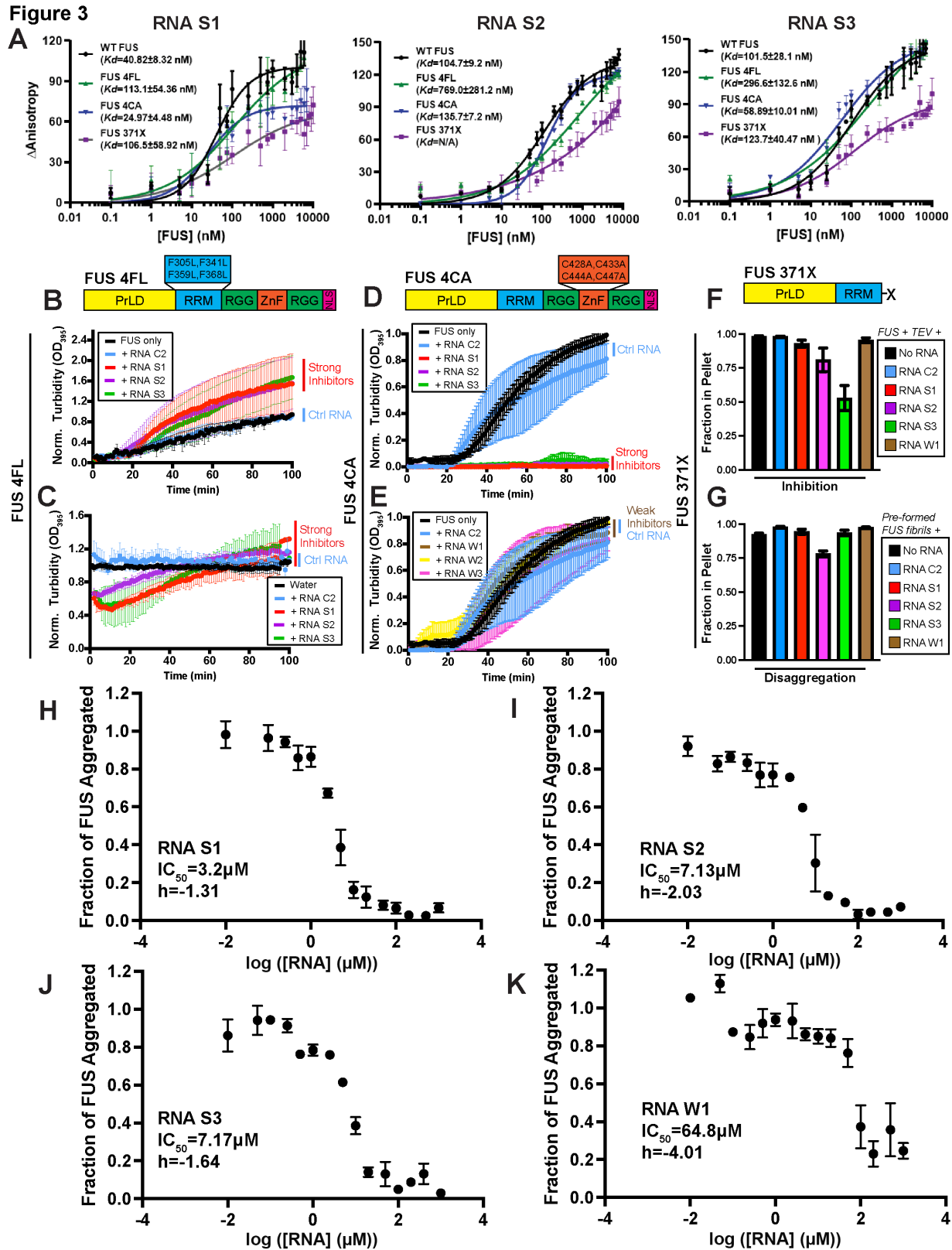
Figure 2



1554

1555 **Figure 2. RNA oligo length, sequence, and structure determine ability to prevent and**
 1556 **reverse FUS fibrillization. (A)** Schematic of strong inhibitor RNA S2, which contains 4 repeats
 1557 of the enriched motif GAGGUGGCUAUG, and RNA S2/2, which contains 2 repeats
 1558 of the same enriched motif. An A to U mutation was introduced in RNAS 2/2 (arrowhead) to evaluate the
 1559 effect of RNA sequence. The red bars represent the consensus FUS-binding motif, which is
 1560 GGUG in RNA S2. The A to U mutation on RNA S2/2 creates overlapping GUGG FUS-binding
 1561 motifs. **(B)** GST-FUS (5 μ M) was incubated with TEV protease in the presence or absence of
 1562 indicated RNA (20 μ M) for 0–100min. Fibrillization was assessed by turbidity. Values are
 1563 means \pm SEM (n=3-4). **(C)** GST-FUS (5 μ M) was incubated with TEV protease for 100min to

1564 form fibrils. At this time, the indicated RNA (20 μ M) was added. Disaggregation was assessed by
1565 turbidity. Values are means \pm SEM (n=3-4). **(D)** Schematic of weak inhibitor RNA W1, which
1566 contains two repeats of enriched motif UCAGAGACAUCA, and RNA W1*2, which doubles the
1567 length of RNA W1 and contains 4 repeats of the enriched motif. **(E)** GST-FUS (5 μ M) was
1568 incubated with TEV protease in the presence or absence of indicated RNA (20 μ M) for 0–
1569 100min. FUS assembly was assessed by turbidity. The FUS only curve was plotted from the
1570 same data set as in (B), since experiments in (B) and (E) were run at the same time. Values are
1571 means \pm SEM (n=3-4). **(F)** GST-FUS (5 μ M) was incubated with TEV protease for 100min to
1572 form fibrils. At this time, the indicated RNA (20 μ M) was added. Disaggregation was assessed by
1573 turbidity. The FUS+C2 curve was plotted from the same data set as in (C), since experiments in
1574 (C) and (F) were run at the same time. Values are means \pm SEM (n=3-5). **(G)** Predicted secondary
1575 structure of U50 and RNA S2 by RNAfold.⁸⁰ **(H)** GST-FUS (5 μ M) was incubated with TEV
1576 protease in the presence or absence of RNA U50 (blue) or RNAS2 (green) (20 μ M) for 0–
1577 100min. FUS assembly was assessed by turbidity. Values are means \pm SEM (n=3). **(I)** GST-FUS
1578 (10 μ M) was incubated for 4 hours in the presence or absence of the indicated RNA (40 μ M).
1579 Droplet formation was assessed by DIC microscopy. Bar, 20 μ m. **(J, K)** smFRET histograms and
1580 representative traces for increasing FUS concentrations (0-500nM) (left) and schematic of the
1581 smFRET experiment in which Cy3 and Cy5 are attached to either end of RNA to report on the
1582 conformational changes induced by FUS binding (right) for RNA U50 (J) and RNA S2 (K).
1583



1584

1585

1586

Figure 3. Strong and weak RNA inhibitors engage multiple RNA-binding domains of FUS to antagonize FUS fibrillization. (A) Change of anisotropy when the indicated fluorescein-

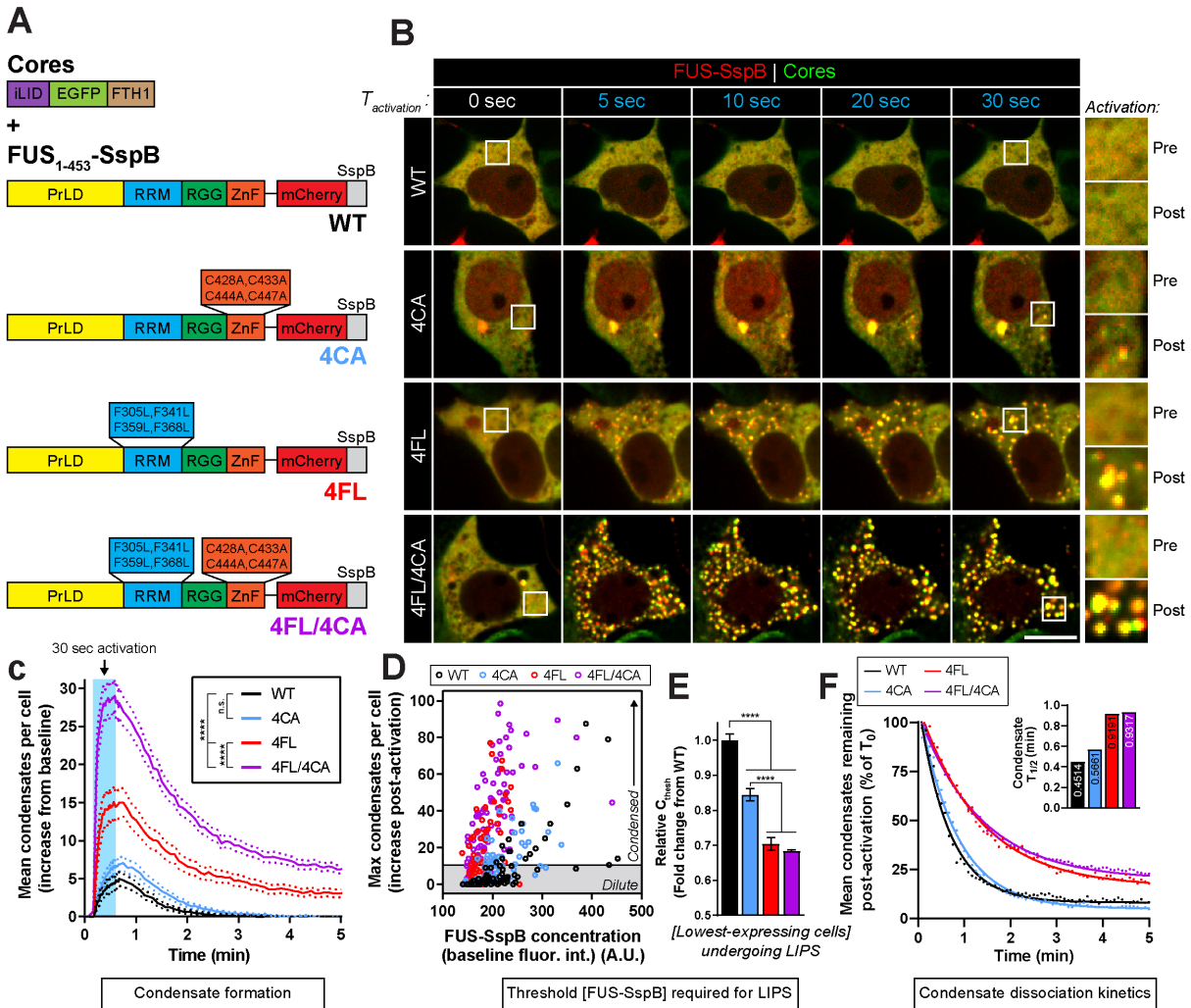
1587 labeled RNA (8nM) binds to GST-FUS, GST-FUS_{4F-L}, GST-FUS_{4C-A}, or GST-FUS_{371X} at the
1588 indicated concentrations. Values represent means±SEM (n=3). Binding curves were fitted by
1589 Prism. Solid line represents the fit and the fitted K_D is listed. **(B)** GST-FUS_{4F-L} (5μM) was
1590 incubated with TEV protease in the presence or absence of strong RNA inhibitors S1, S2, or S3
1591 or the control C2 RNA (20μM) for 0–100min. Fibrillization was assessed via turbidity. Values
1592 represent means±SEM (n=3). **(C)** FUS_{4F-L} fibrils (5μM monomer) were treated with water or the
1593 indicated RNA (20μM). Disaggregation was assessed by turbidity. Values represent
1594 means±SEM (n=2-3). **(D)** GST-FUS_{4C-A} (5μM) was incubated with TEV protease in the
1595 presence or absence of strong RNA inhibitors S1, S2, and S3 or the control C2 RNA (20μM) for
1596 0–100min. Fibrillization was assessed via turbidity. Values represent means±SEM (n=3). **(E)**
1597 GST-FUS_{4C-A} (5μM) was incubated with TEV protease in the presence or absence of weak RNA
1598 inhibitors W1, W2, or W3 or the control C2 RNA (20μM) for 0–100 min. Fibrillization was
1599 assessed via turbidity. The FUS only and RNA C2 curves were plotted from the same data set as
1600 in **(D)**, since experiments in **(D)** and **(E)** were run at the same time. Values represent
1601 means±SEM (n=3). **(F)** GST-FUS_{371X} (10μM) was incubated with TEV protease in the presence
1602 or absence of the indicated RNA (40μM) at 25°C for 24h with agitation at 1200rpm. Aggregated
1603 FUS was quantified by sedimentation assay. Values represent means±SEM (n=3). **(G)** FUS_{371X}
1604 fibrils (10μM monomer) were treated with water or indicated RNA (40μM) for 24h. Aggregated
1605 FUS was quantified by sedimentation assay. Values represent means±SEM (n=3). **(H-K)** GST-
1606 FUS (5μM) was incubated with TEV protease in the presence or absence of **(H)** RNA S1, **(I)**
1607 RNA S2, **(J)** RNA S3, or **(K)** RNA W1 at indicated concentration for 0–100min. Fibrillization
1608 was assessed via turbidity. The dose response curves were fit by Prism using the log(inhibitor)
1609 vs. response -- Variable slope function. Values represent means±SEM (n=3).

1610
1611 See also **Figure S3**.

1612

1613

Figure 4

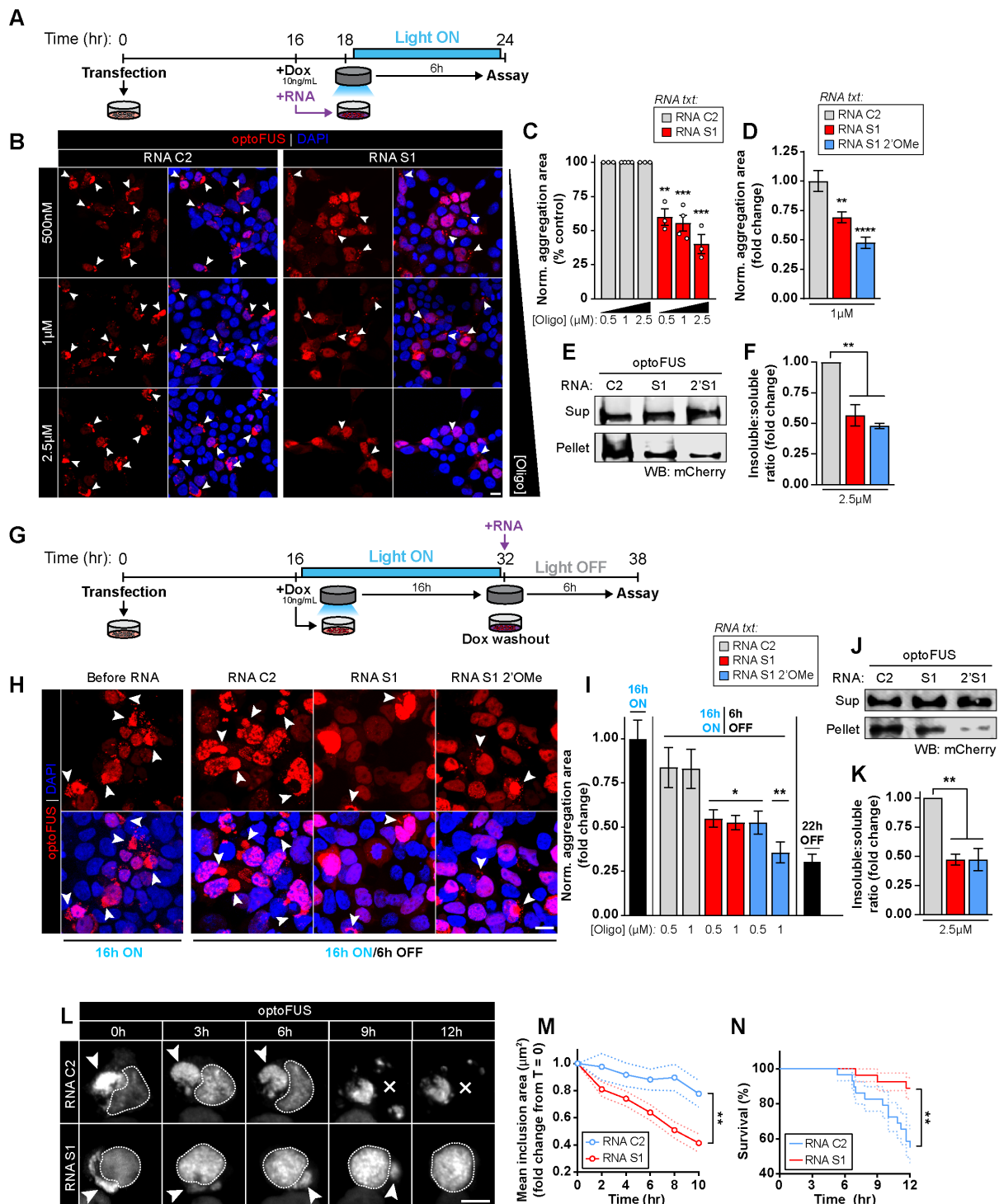


1614

1615 **The FUS RRM and ZnF domains cooperate to maintain FUS solubility in human cells. (A)**
 1616 Schematic of iLID cores and FUS-SspB mutant constructs used in (B-F). **(B)** Representative
 1617 images of HEK293 cells co-expressing iLID cores (green) and the indicated mutant FUS-SspB
 1618 protein (red) prior to and during a 30s light activation protocol (488nm, 75% laser power). Insets
 1619 show the boxed cytoplasmic area at baseline and following 30s activation. Bar, 10 μ m. **(C)**
 1620 Quantification of the average number of FUS-SspB assemblies formed per cell during and
 1621 following a 30s light activation period. $n=68-91$ cells per condition. Data are shown as mean
 1622 (solid lines) \pm SEM (dashed lines). Two-way ANOVA with Tukey's post-hoc test was used to
 1623 compare across groups; ****, $p<0.0001$. **(D)** Graph of maximal light response (number of
 1624 condensates during the activation period) in (C) plotted against baseline FUS-SspB
 1625 concentration. Data points represent individual cells. **(E)** Quantification of representative
 1626 threshold concentrations required for cells to undergo LIPS. $n =$ the lowest-expressing 5 cells
 1627 with >10 condensates post-activation per condition. Values represent means \pm SEM. Fluorescence
 1628 intensity values are normalized to WT and shown as fold-change. One-way ANOVA with
 1629 Tukey's post-hoc test was used to compare across groups; ****, $p<0.0001$. **(F)** Quantification of

1630 FUS condensate dissociation kinetics following conclusion of light activation. Number of
1631 condensates per cell were plotted over time as a percentage of condensates in the first frame
1632 following light removal (T_0). One-phase exponential decay curves were fit and $T_{1/2}$ was
1633 calculated for each condition and plotted in the inset (top right). $n=20-76$ cells per group.
1634

Figure 5



1635
1636
1637
1638

Figure 5. RNA S1 prevents and reverses aberrant phase transitions of FUS in human cells. (A) Schematic of light-activation paradigm used to assess whether RNA inhibitors can prevent optoFUS phase separation used in (B-F). (B) Representative images of optoFUS-expressing

1639 HEK293 cells pre-treated with control RNA C2 (Ctrl) or strong RNA inhibitor (S1) at
1640 concentrations ranging from 500nM-2.5 μ M for 2h prior to exposure to 6h of light activation.
1641 Bar, 10 μ m. Arrows indicate cytoplasmic optoFUS assemblies. **(C)** OptoFUS aggregation area in
1642 light-activated cells pre-treated with RNA C2 (Ctrl) or RNA S1 at the indicated concentrations.
1643 Data points represent individual experiments, $n=3-4$ individual experiments, 620-904 cells across
1644 9 randomized fields-of-view per experiment. Values are normalized to control treatments within
1645 each treatment concentration group and presented as percentage of control per experiment.
1646 Values are means \pm SEM ($n=3-4$). Unpaired Student's t-tests were used to compare RNA C2 and
1647 S1 conditions within each treatment concentration. **, $p<0.01$, ***, $p<0.001$. **(D)** OptoFUS
1648 aggregation area in light-activated cells pre-treated with 1 μ M RNA C2 (Ctrl), RNA S1, or
1649 2'OMe-modified RNA S1 oligonucleotide. $n = 9$ randomized fields-of-view, 144-323 cells per
1650 field. Values are normalized to control treatments and presented as fold-change from control.
1651 Values are means \pm SEM ($n=3$ independent experiments). One-way ANOVA with Tukey's post
1652 hoc test was used to compare across groups. **, $p<0.01$, ****, $p<0.0001$. **(E)** Detergent-
1653 solubility fractionation of cells pre-treated with 2.5 μ M RNA C2 (Ctrl), RNA S1, or 2'OMe-
1654 modified RNA S1 prior to light-activation. **(F)** Quantification of ratios of detergent-insoluble to
1655 detergent-soluble band intensities in each treatment group described in (E). $n=3$ biological
1656 replicates per condition. Values are means \pm SEM ($n=3$ independent experiments). One-way
1657 ANOVA with Tukey's post hoc test was used to compare across groups; **, $p<0.01$. **(G)**
1658 Schematic of light-activation paradigm used to assess whether RNA inhibitors can reverse
1659 optoFUS phase separation used in (H-K). **(H)** Representative images of optoFUS-expressing
1660 HEK293 cells exposed to the light-induction protocol outlined in (G) before addition of RNA
1661 (left panel) and following a 6h treatment with 1 μ M RNA C2 (Ctrl), RNA S1 or 2'OMe-modified
1662 RNA S1 (right panels) in the absence of further light stimulation. Bar, 10 μ m. Arrows indicate
1663 cytoplasmic optoFUS assemblies. **(I)** optoFUS aggregation area prior to (left black bar) and
1664 following treatment (middle bars) with the indicated RNA. Aggregation values from cells kept in
1665 darkness throughout the experiment (22h OFF, black bar) are included for reference. Values are
1666 normalized to groups fixed immediately following light activation and prior to RNA treatment.
1667 $n=9$ randomized fields-of-view, 79-275 cells per field. Comparisons shown are between control
1668 and targeting RNA treatments. Values are means \pm SEM ($n=3$ independent experiments). One-
1669 way ANOVA with Tukey's post hoc test was used to compare across groups. *, $p<0.05$, **,
1670 $p<0.01$. **(J)** Detergent-solubility fractionation of cells treated with 2.5 μ M of the indicated RNA
1671 for 6h in the absence of light following pre-formation of light-induced optoFUS aggregates as in
1672 (G). **(K)** Quantification of ratios of detergent-insoluble to detergent-soluble band intensities in
1673 each treatment group described in (J). $n=3$ biological replicates per condition. Data shown are
1674 means \pm SEM. One-way ANOVA with Tukey's post hoc test was used to compare across groups;
1675 **, $p<0.01$. **(L)** Representative live images of HEK293 cells expressing optoFUS pre-exposed to
1676 10h of blue light stimulation following 2 μ M treatment with the indicated oligonucleotides as in
1677 (H-K). Arrows indicate inclusions and X indicates cell death. Cell nuclei are circled. Bar, 10 μ m.
1678 **(M)** Quantification of mean optoFUS inclusion size over time following treatment with the
1679 indicated oligonucleotides. $n = 26-29$ inclusions per treatment. Data are presented as mean (solid
1680 lines) \pm SEM (dashed lines). Two-way mixed design ANOVA with Sidak's correction was used
1681 to compare across groups; **, $p<0.01$. **(N)** Survival curves of cells containing optoFUS
1682 inclusions at the onset of imaging treated with the indicated oligonucleotides. $n=27-29$ cells per
1683 treatment. Kaplan-Meier estimates were used to generate survival curves (dashed lines represent

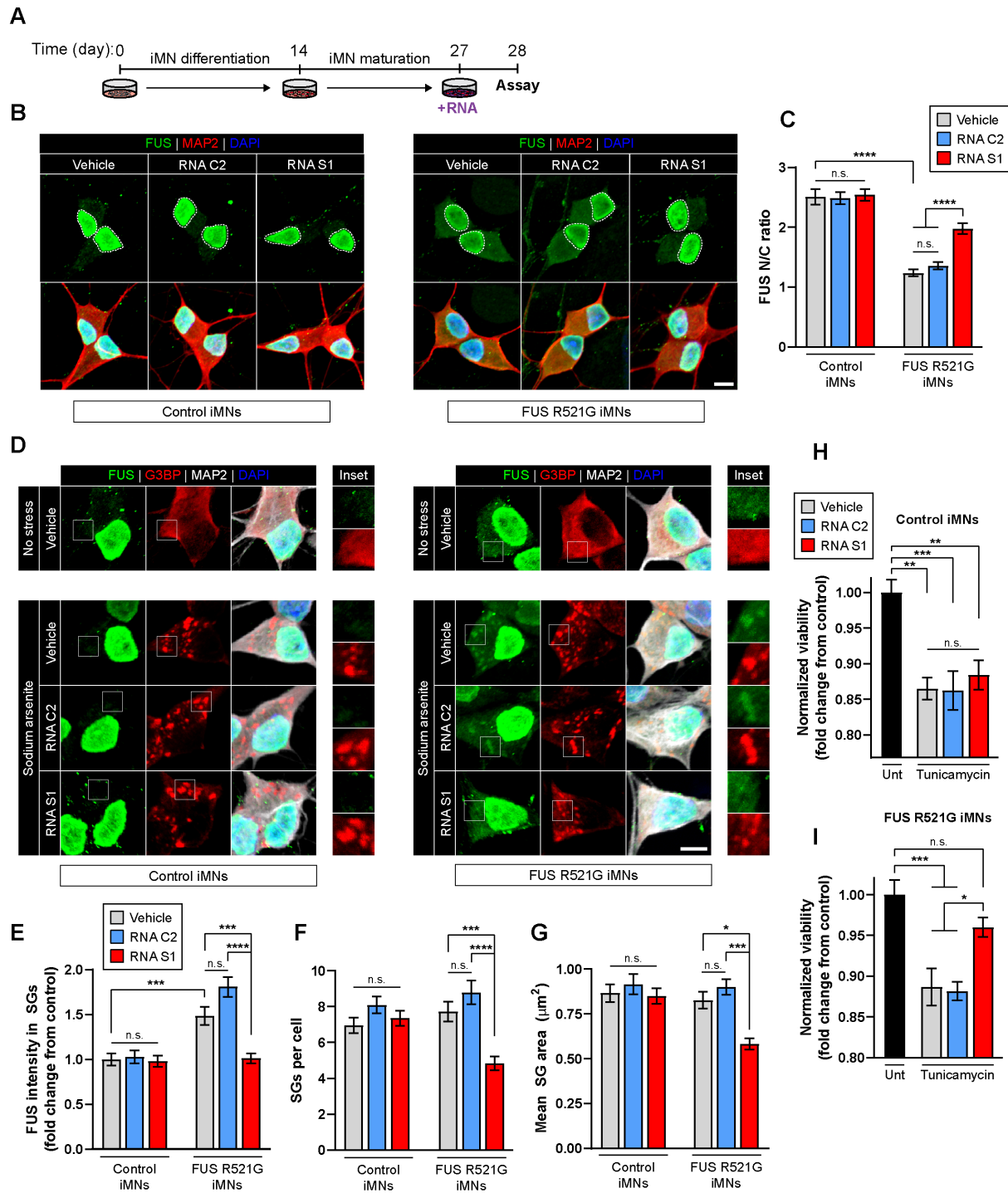
1684 standard error) and Gehan-Breslow-Wilcoxon tests were used to compare across groups, **,
1685 $p < 0.01$.

1686

1687 See also **Figure S4** and **S5**.

1688

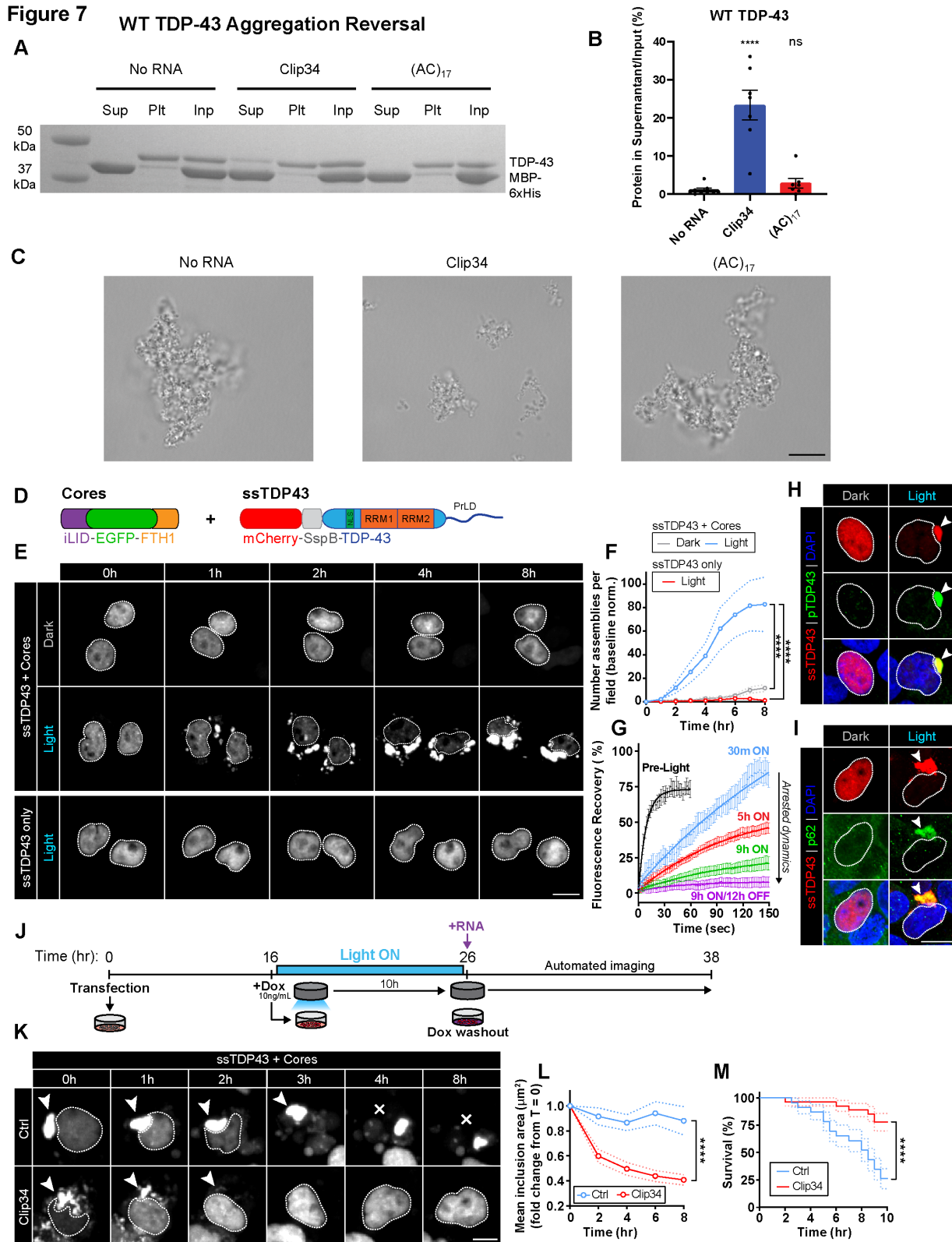
Figure 6



1689
1690
1691
1692
1693
1694

Figure 6. RNA S1 prevents FUS phase separation and mitigates toxicity in iPSC-derived FUS^{R521G} motor neurons. (A) Schematic of motor neuron differentiation and RNA oligonucleotide treatment paradigm used in (B-I). Control iPSC motor neurons (iMNs) or FUS^{R521G} ALS iMNs that harbor a single FUS^{R521G} mutation in the NLS were treated with a control or RNA S1 (500nM for 24h). (B) Representative images of immunostained control and

1695 FUS^{R521G} iMNs revealed enriched cytoplasmic FUS protein in FUS^{R521G} iMNs. **(C)** Graph
1696 depicts means±SEM of FUS nuclear/cytoplasmic (N/C) ratio in FUS^{R521G} ALS iMNs, indicating
1697 a reduced FUS N/C localization in vehicle and control oligonucleotide (RNA C2) treated iMNs
1698 compared to controls. RNA S1 enhanced FUS nuclear localization in FUS^{R521G} ALS iMNs but
1699 not control iMNs (n=81-87 iMNs over 3 differentiations; two-way ANOVA with Bonferroni
1700 correction: ****, p<0.0001). **(D)** Representative images of immunostained SGs (G3BP1; inset)
1701 induced with NaAsO₂ (0.5mM for 45min) in control and FUS^{R521G} iMNs pre-treated with a
1702 vehicle, control oligonucleotide (RNA C2) or RNA S1 (500nM). **(E)** FUS intensity (pixel/μm²)
1703 colocalization with G3BP1 SGs was enhanced in FUS^{R521G} iMNs compared to controls and
1704 reduced by RNA S1 (means±SEM, n=363-509 SGs, over 3 differentiations; two-way ANOVA
1705 with Bonferroni correction: ***, p<0.001; ****, p<0.0001). **(F)** G3PB1+ SG number/cell and
1706 **(G)** mean G3PB1+ SG area were reduced in FUS^{R521G} iMNs upon S1 oligonucleotide treatment
1707 but did not affect control iMNs (means±SEM, n=363-509 SGs, 59-67 iMNs over 3
1708 differentiations; two-way ANOVA with Bonferroni correction: ***, p<0.001; ****, p<0.0001).
1709 **(H-I)** Control and FUS^{R521G} iMNs exhibit reduced viability (as measured by intracellular ATP)
1710 following tunicamycin treatment (25μM for 24h) when compared to untreated iMNs (Utr). RNA
1711 S1 (500nM) treatment enhanced FUS^{R521G} iMN viability compared to vehicle and control
1712 oligonucleotide (RNA C2) treatment. (4 technical replicates per experiment, 3 differentiations
1713 per line; one-way ANOVA with Bonferroni correction: *, p<0.05; **, p<0.01; ****, p<0.001).
1714



1715
1716
1717
1718

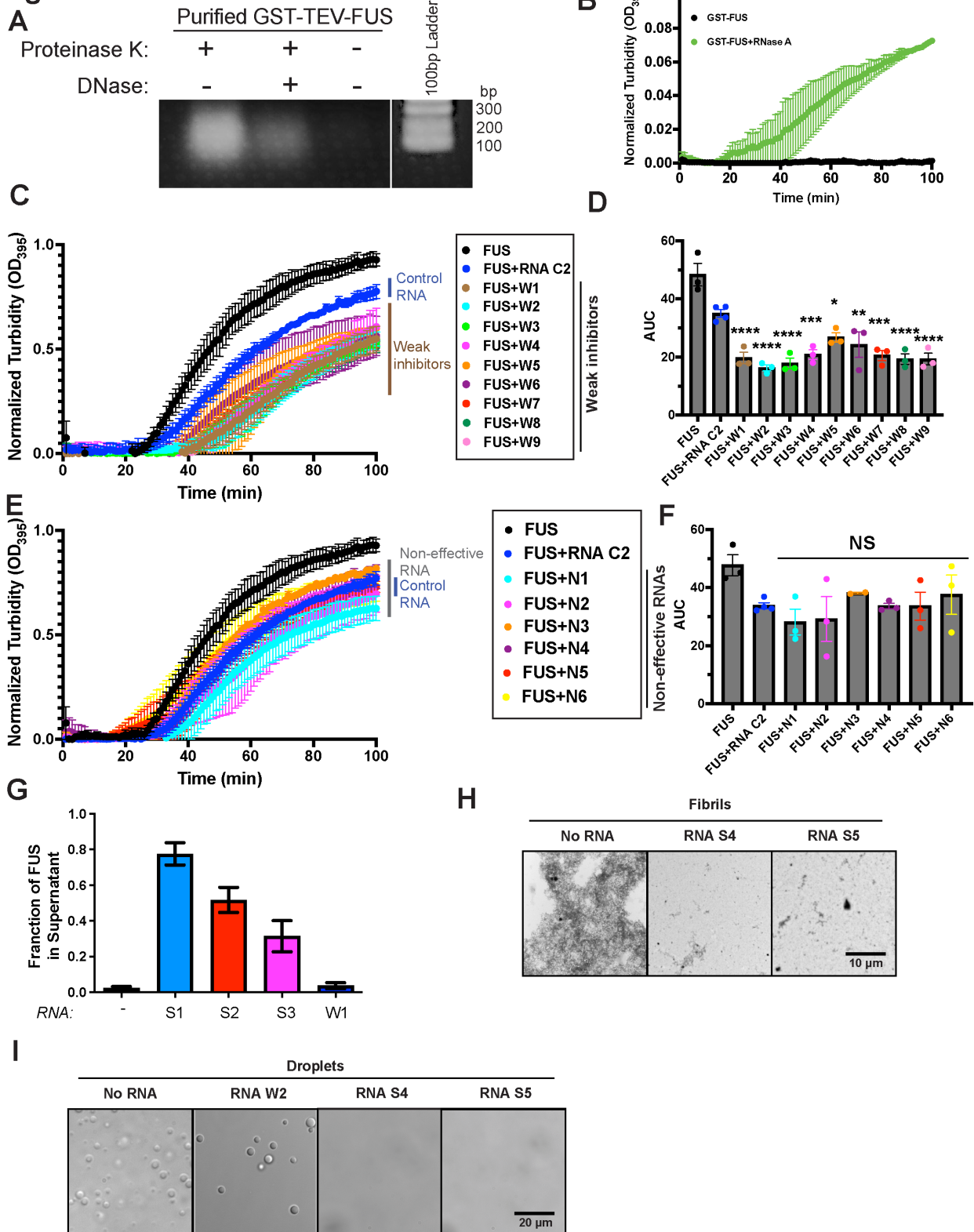
Figure 7. Clip34 reverses aberrant TDP-43 phase separation. (A-C) Preformed TDP-43 aggregates (4μM) were incubated with buffer, Clip34, or (AC)₁₇ (40μM) for 16h. Reactions were processed for sedimentation analysis and the supernatant, pellet, and input (100%) were

1719 fractionated by SDS-PAGE and Coomassie stain (A). The fraction of soluble TDP-43 in the
1720 supernatant was determined by densitometry (B). Values represent means±SEM (n=7). One-way
1721 ANOVA comparing to the No RNA condition; Dunnett's multiple comparisons test; ns: $p>0.05$,
1722 **** p adjusted ≤ 0.0001 . Alternatively (C), reactions were viewed by brightfield microscopy.
1723 Note that large and dense TDP-43 aggregates persist in buffer or after treatment with (AC)₁₇
1724 RNA, whereas Clip34 reduces aggregate size. Bar, 10µm. (D) Schematic of iLID cores and
1725 ssTDP-43 constructs used in (E-M). (E) Representative images of HEK293 cells co-expressing
1726 iLID cores and ssTDP43 (top panels) or ssTDP43 alone (bottom panel) during simultaneous live
1727 imaging and light stimulation. Bar, 10µm. Cell nuclei are circled. (F) Quantification of number
1728 of ssTDP43 assemblies per field-of-view during time course of live imaging. $n=6$ fields-of-view,
1729 171-408 cells per field. Data are shown as means (solid lines) ± SEM (dashed lines). $n=3$
1730 experiments. Two-way ANOVA with Tukey's post hoc test was used to compare across groups;
1731 ****, $p<0.0001$. (G) FRAP analysis of ssTDP43 assemblies formed in HEK293 cells co-
1732 expressing iLID cores over increasing lengths of blue light stimulation (0.1-0.3mW/cm², 465
1733 nm). Values are means±SEM (n=3 experiments). (H, I) Immunofluorescence analysis of co-
1734 localization between ssTDP43 inclusions formed following 8h of blue light stimulation and the
1735 pathological hallmarks phospho-TDP43 (H) and p62 (I). Cell nuclei are circled. Arrows indicate
1736 light-induced inclusions. Bars, 10µm. (J) Schematic of light-activation paradigm used for pre-
1737 formation of ssTDP43 inclusions prior to RNA treatments and live imaging used in (L-M). (K)
1738 Representative live images of HEK293 cells co-expressing iLID cores and ssTDP43 pre-exposed
1739 to 10h of blue light stimulation following treatment with 2µM of RNA C2 (Ctrl) or RNA Clip34.
1740 Arrows indicate inclusions and X indicates cell death. Cell nuclei are circled. Bar, 10µm. (L)
1741 Quantification of mean inclusion size over time following treatment with RNA C2 (Ctrl) or RNA
1742 Clip34. Values shown are normalized to areas of individual inclusions at the onset of imaging
1743 and are presented as fold-change from T₀. $n=25-37$ inclusions per treatment. Data are shown as
1744 means (solid lines) ± SEM (dashed lines). Two-way mixed design ANOVA with Sidak's
1745 correction; ****, $p<0.0001$. (M) Survival curves of cells containing ssTDP43 inclusions at the
1746 onset of imaging treated with the indicated oligonucleotides. $n=23-26$ cells. Kaplan-Meier
1747 estimates were used to generate survival curves (dashed lines represent standard error) and
1748 Gehan-Breslow-Wilcoxon tests were used to compare across groups, **** $p\leq 0.0001$.

1749
1750 See also **Figure S6** and **S7**.

1751

Figure S1



1752
1753
1754

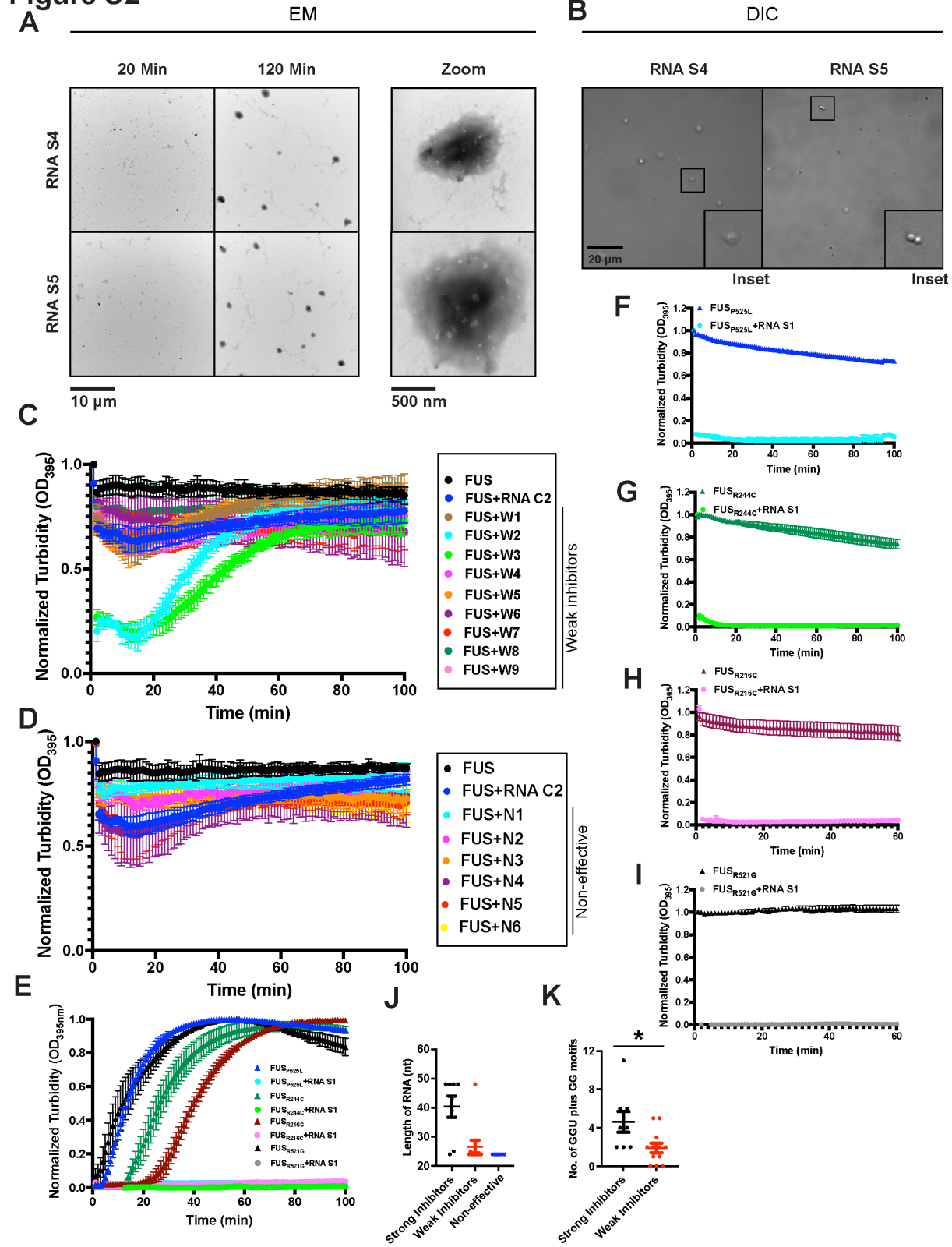
Figure S1. Weak RNA inhibitors inhibit FUS fibrillization but not FUS PS. (A) Agarose gel reveals RNA in GST-FUS purified from *E. Coli*. GST-FUS purified from *E. Coli* was treated at

1755 37°C for one hour with proteinase K, proteinase K and DNase, or left untreated. Samples were
1756 then analyzed by 1% agarose gel and stained with ethidium bromide. **(B)** GST-FUS (5µM) was
1757 incubated without TEV protease in the presence or absence of RNase A. FUS assembly was
1758 monitored by turbidity. Values represent means±SEM (n=2). **(C)** GST-FUS (5µM) was
1759 incubated with TEV protease in the presence or absence of weak RNA inhibitor (RNA W1-W9;
1760 20µM) for 0–100min. Turbidity measurements were taken every minute to assess the extent of
1761 FUS assembly. The FUS only curve and FUS+RNA C2 curve were plotted from the same data
1762 set as in Figure 1B, since experiments in these two figures were run at the same time. Values
1763 represent means±SEM (n=3). **(D)** Area under the curve calculated using Prism for each replicate
1764 summarized in (C) quantifies the extent of FUS assembly. The FUS only curve and FUS+RNA
1765 C2 curve were plotted from the same data set as in Figure 1B, since experiments in these two
1766 figures were run at the same time. Values represent means±SEM (n=3). One-way ANOVA and
1767 Dunnett's test were used to compare to the RNA C2 condition; ns: $p>0.05$, * $p\leq 0.05$, ** $p\leq 0.01$,
1768 *** $p\leq 0.001$, and **** $p\leq 0.0001$. **(E)** GST-FUS (5µM) was incubated with TEV protease in the
1769 presence or absence of indicated RNA (20µM) for 0–100min. Turbidity measurements were
1770 taken every minute to assess the extent of FUS assembly. The FUS only curve and FUS+RNA
1771 C2 curve were plotted from the same data set as in Figure 1B, since experiments in these two
1772 figures were run at the same time. Values represent means±SEM (n=3). **(F)** Area under the
1773 curve calculated using Prism for each replicate summarized in (E) quantifies the extent of
1774 aggregation. Values represent means±SEM (n=3). Non-effective RNAs do not show statistical
1775 difference compared to RNA C2 in inhibiting FUS assembly. One-way ANOVA and Dunnett's
1776 test were used to compare to the RNA C2 condition; ns: $p>0.05$. **(G)** GST-FUS (5µM) was
1777 incubated with TEV protease in the presence or absence of the indicated RNA (20µM) for 0–
1778 90min. At 90min, reactions were processed for sedimentation analysis. Supernatant fractions
1779 were resolved by SDS-PAGE and stained with Coomassie Brilliant Blue. The amount of FUS in
1780 the supernatant fraction was determined by densitometry in comparison to known quantities of
1781 FUS. Values represent means±SEM (n=3). **(H)** GST-FUS (5µM) was incubated with TEV
1782 protease in the presence or absence of strong RNA inhibitor (RNA S4, RNA S5; 20µM) for
1783 100min. Samples were processed for EM at the end of the reaction. Bar, 10µm. **(I)** GST-FUS
1784 (10µM) was incubated for 4h in the presence or absence of the indicated RNA (40µM). Droplet
1785 formation was assessed by DIC microscopy. Bar, 20µm.

1786
1787 Related to **Figure 1**.

1788
1789

Figure S2



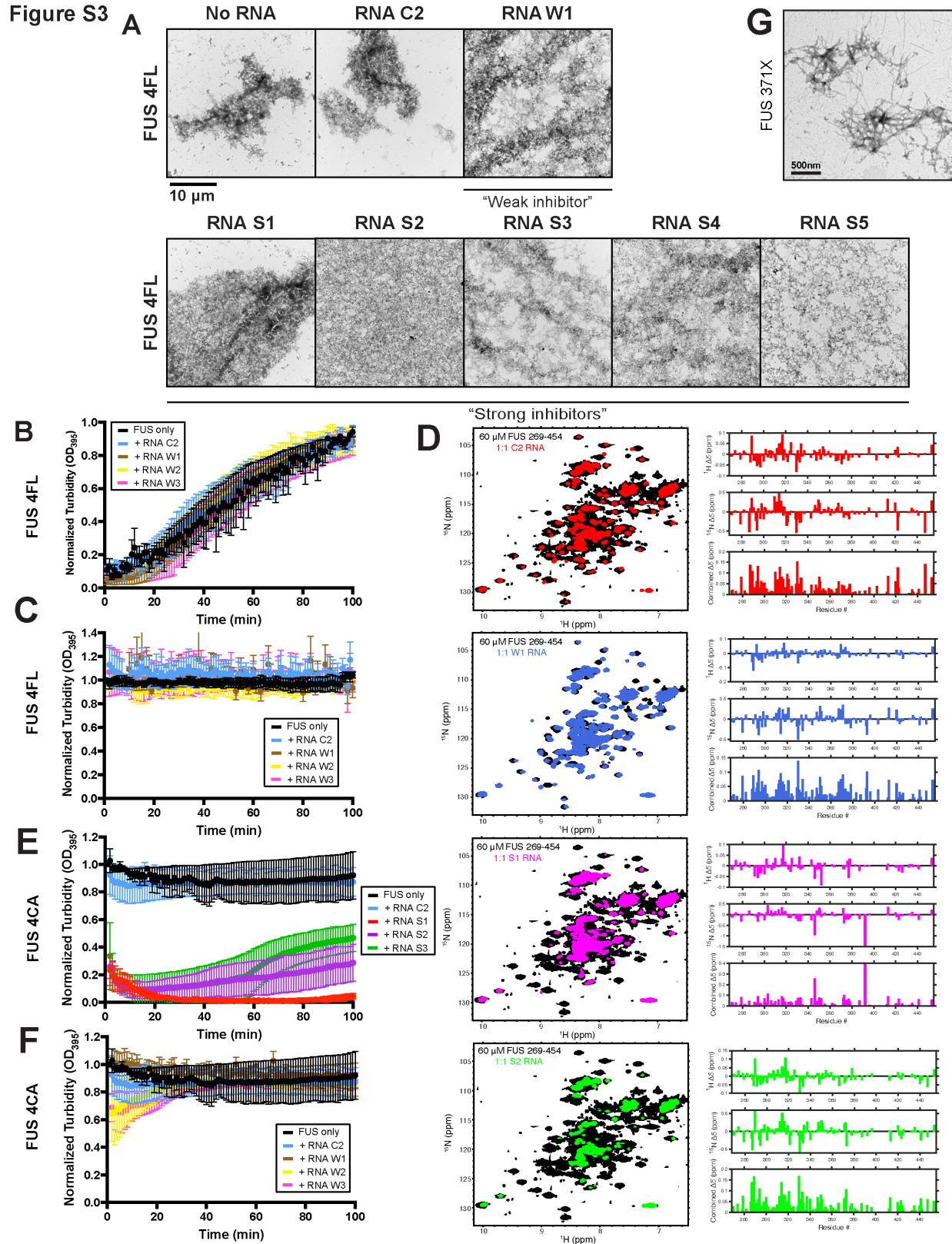
1790
1791
1792

Figure S2. Strong RNA inhibitors prevent and reverse fibrillization of ALS-linked FUS variants. (A) GST-FUS (5 μ M) was incubated with TEV protease for 100min to assemble fibrils.

1793 At the end of the reaction, RNA S4 or S5 (20 μ M) were added to the reaction. Samples were
1794 taken after 20min and 120min to visualize the disaggregation products via EM. Bar, 10 μ m. The
1795 right images show higher magnification of the dense protein phase observed in the middle panel.
1796 Note the porous structure indicative of hydrogel formation. Bar, 500nm. **(B)** DIC images of the
1797 hydrogel sample observed in (A) indicating they are small solid-like drops that do not fuse. Bar,
1798 20 μ m. **(C)** GST-FUS (5 μ M) was incubated with TEV protease for 100min to assemble fibrils. At
1799 the end of the reaction, water or indicated weak RNA inhibitor (20 μ M) was added to the
1800 reaction. Turbidity measurements were taken every minute to assess the extent of disaggregation.
1801 The FUS only curve and FUS+RNA C2 curve were plotted from the same data set as in Figure
1802 1F, since experiments in these two figures were run at the same time. Values represent
1803 means \pm SEM (n=3-4). **(D)** GST-FUS (5 μ M) was incubated with TEV protease for 100min to
1804 assemble fibrils. At the end of the reaction, water or indicated non-effective RNA (20 μ M) was
1805 added to the reaction. Turbidity measurements were taken every minute to assess the extent of
1806 disaggregation. The FUS only curve and FUS+RNA C2 curve were plotted from the same data
1807 set as in Figure 1F, since experiments in these two figures were run at the same time. Values
1808 represent means \pm SEM (n=3-4). **(E)** GST-FUS^{P525L}, GST-FUS^{R244C}, GST-FUS^{R216C} or GST-
1809 FUS^{R521G} (5 μ M) was incubated with TEV protease in the presence or absence of RNA S1
1810 (20 μ M) for 0–100min. Fibrillization was assessed by turbidity. Values represent means \pm SEM
1811 (n=3). **(F-I)** GST-FUS^{P525L} (F), GST-FUS^{R244C} (G), GST-FUS^{R216C} (H), or GST-FUS^{R521G} (I)
1812 (5 μ M) was incubated with TEV protease for 100min to form fibrils. At this time, water, or RNA
1813 S1 (20 μ M) was added to the reaction. Turbidity measurements were taken every minute to assess
1814 the extent of disaggregation. Values represent mean \pm SEM (n=3). **(J)** Length distribution of
1815 strong RNA inhibitors (n=8), weak RNA inhibitors (n=15), and non-effective RNAs (n=8). Bars
1816 represent means \pm SEM. **(K)** Distribution of the number of GGU motifs plus GG motifs in strong
1817 inhibitors (n=8) and weak inhibitors (n=15). Bars represent means \pm SEM. Unpaired Student's t-
1818 tests were used to compare between groups. * $p\leq 0.05$.

1819
1820 Related to **Figure 1**.

1821
1822



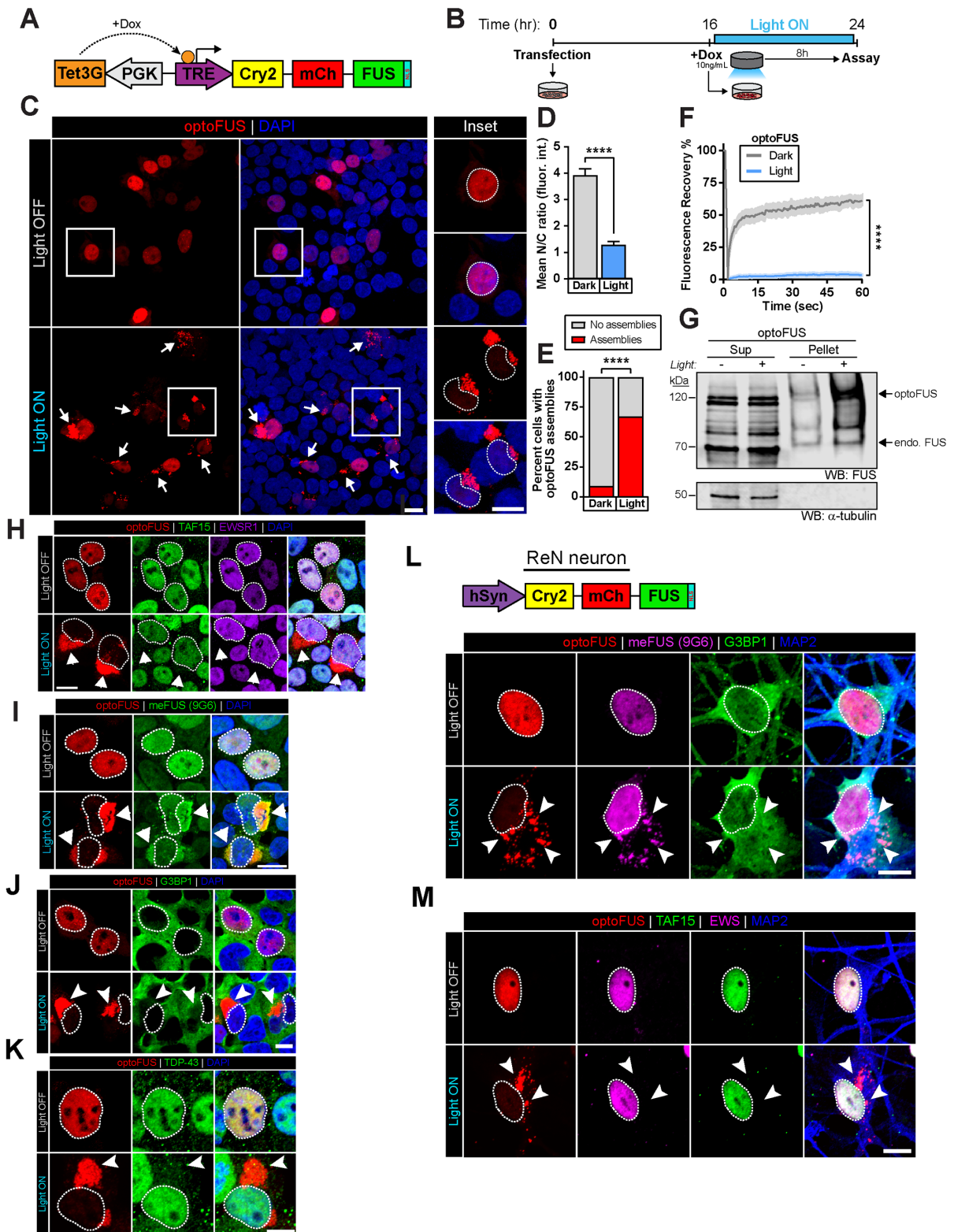
1823
1824
1825

Figure S3. Strong and weak RNA inhibitors engage multiple RNA-binding domains of FUS to antagonize FUS fibrillization. (A) GST-FUS_{4FL} (5 μ M) was incubated with TEV protease in

1826 the presence or absence of the indicated RNA inhibitors or the control C2 RNA (20 μ M) for 0–
1827 100min. At the end of the fibrillization reactions, samples were processed for EM. Bar, 10 μ m.
1828 **(B)** GST-FUS_{4F-L} (5 μ M) was incubated with TEV protease in the presence or absence of weak
1829 RNA inhibitors W1, W2, or W3 or the control C2 RNA (20 μ M) for 0–100min. Fibrillization was
1830 assessed via turbidity. Values represent means \pm SEM (n=3). **(C)** FUS_{4F-L} fibrils (5 μ M monomer)
1831 were treated with water or the indicated RNA (20 μ M). Disaggregation was assessed by turbidity.
1832 Values represent means \pm SEM (n=2-3). **(D)** NMR spectra (left) of FUS₂₆₉₋₄₅₄ without and with
1833 the addition of the indicated RNA show significantly more line broadening by addition of S1 and
1834 S2 RNA inhibitors than C1 or W1, consistent with tighter binding for S1 and S2 compared to C1
1835 and W1. Chemical shift perturbations (right) quantified for these spectra as a function of residue
1836 number show perturbations across the entire FUS sequence for all RNAs, even for C1 and W1
1837 RNAs, suggesting RNA binding across multiple FUS domains. **(E)** FUS_{4C-A} fibrils (5 μ M
1838 monomer) were treated with water or the indicated RNA (20 μ M). Disaggregation was assessed
1839 by turbidity. Values represent means \pm SEM (n=3). **(F)** FUS_{4C-A} fibrils (5 μ M monomer) were
1840 treated with water or the indicated RNA (20 μ M). Disaggregation was assessed by turbidity. The
1841 FUS only curve and FUS+RNA C2 curve were plotted from the same data set as in (E), since
1842 experiments in these two panels were run at the same time. Values represent means \pm SEM (n=3).
1843 **(G)** GST-FUS_{371X} (10 μ M) was incubated with TEV protease at 25°C for 24h with agitation at
1844 1200rpm. At the end of the fibrillization reaction, sample was processed for EM. FUS_{371X} forms
1845 fibrils like WT FUS, although the kinetics are much slower. Bar, 500nm.

1846
1847 Related to **Figure 3**.
1848

Figure S4



1849

1850

1851

Figure S4. An optogenetic model of FUS-ALS pathology. (A) Schematic of the optoFUS construct used in these experiments, in which an N-terminal Cry2olig-mCherry fusion to the full-

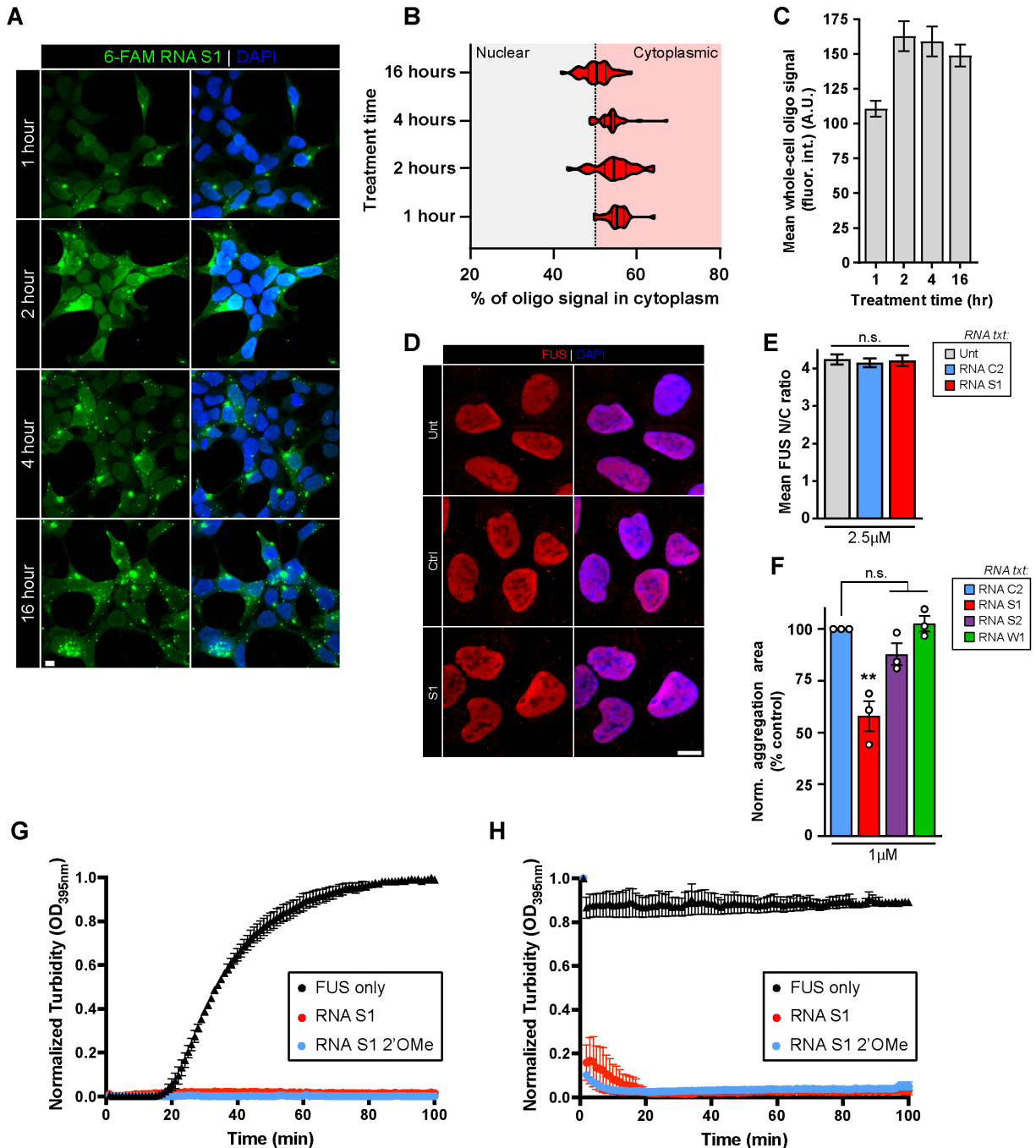
1852 length FUS protein is expressed under the control of the doxycycline-inducible pTRE3G
1853 promoter. **(B)** Light-induction paradigm used to induce optoFUS inclusion formation. **(C)**
1854 Representative images of cells optoFUS-expressing cells exposed to 8h of darkness or light. Cell
1855 nuclei are circled. Bar, 10 μ m. **(D)** Immunofluorescence analysis of optoFUS nuclear/cytoplasmic
1856 signal following light induction protocol. Values represent means \pm SEM. $n=45$ cells per group.
1857 Unpaired Student's t-tests were used to compare across groups, **** $p<0.0001$. **(E)**
1858 Quantification of the percentage of cells containing cytoplasmic optoFUS inclusions following
1859 8h of darkness or light. $n=128-147$ cells per group. Unpaired Student's t-tests were used to
1860 compare across groups. **** $p<0.0001$. **(F)** Fluorescence recovery after photobleaching (FRAP)
1861 analysis of light-induced inclusions or nuclear optoFUS signal in cells kept in darkness. Values
1862 represent means (solid line) \pm SEM (shaded area). $n=15-23$ cells. Two-way ANOVA with Sidak
1863 post-hoc analysis, **** $p<0.0001$. **(G)** Detergent-solubility fractionation of optoFUS cell lysates
1864 collected following 16h of darkness or light. **(H-I)** Immunofluorescence analysis of optoFUS
1865 inclusions for co-localization with (H) FTLD-FUS pathological hallmarks TAF15 (green) and
1866 EWSR1 (purple) or (I) the ALS-FUS-associated methylated FUS antibody 9G6 (green). Cell
1867 nuclei are circled. Bar, 10 μ m. **(J, K)** HEK293 cells expressing optoFUS were exposed to 8h of
1868 blue light stimulation prior to fixation and immunofluorescence analysis of stress granule marker
1869 G3BP1 and ALS-related protein TDP-43. Arrows indicate optoFUS inclusions. Cell nuclei are
1870 circled. Bars, 10 μ m. **(L, M)** Human ReN neurons expressing optoFUS under the control of the
1871 human synapsin promoter (hSyn) were exposed to 72h of blue light stimulation prior to
1872 immunofluorescence analysis of FUS pathological hallmarks. Similar to inclusions formed in
1873 HEK293 cells, optoFUS inclusions in human neurons are positive for methylated FUS (9G6),
1874 negative for stress granule protein G3BP1 and negative for fellow FET family proteins TAF15
1875 and EWSR1, suggesting a closer resemblance to ALS-FUS than FTD-FUS pathology. Arrows
1876 indicate optoFUS inclusions. Cell nuclei are circled. Bars, 10 μ m.

1877

1878 Related to **Figure 5**.

1879

Figure S5



1880
1881
1882
1883
1884
1885
1886
1887

Figure S5. RNA S1 prevents and reverses aberrant phase transitions of FUS in human cells. (A) Representative images of HEK293 cells treated with 2.5 μM of a 6-FAM-labeled RNA S1 for the indicated time periods. Bar, 10 μm. (B) Quantification of percentage of 6-FAM-labeled RNA S1 signal present in the cytoplasm of cells treated for the indicated time periods. $n=50-86$ cells per treatment time. (C) Quantification of mean whole-cell fluorescence intensity of 6-FAM-labeled RNA S1 present within cells treated for the indicated time periods. Values represent means ± SEM. $n=34-47$ cells per treatment time. (D) HEK293 cells were either untreated or

1888 treated with 2.5 μ M of RNA C2 (Ctrl) or RNA S1 for 24h prior to immunofluorescence analysis
1889 of endogenous FUS localization. Bar, 10 μ m. **(E)** Mean nuclear/cytoplasmic ratios of FUS
1890 fluorescence intensity in cells treated with the indicated oligonucleotides. Values represent
1891 means \pm SEM. $n=41-66$ cells per group. One-way ANOVA with Tukey's post hoc test was used to
1892 compare across groups. **(F)** Normalized aggregation area of optoFUS-expressing HEK293 cells
1893 pre-treated with 1 μ M of RNA C2 (Ctrl), RNA S1, RNA S2, or RNA W1 for two hours prior to a
1894 6-hour light activation period. Bars represent means \pm SEM. Data points represent individual
1895 experiments. $n = 3$ individual experiments, 1236-2835 cells across 9 randomized fields-of-view
1896 per experiment. One-way ANOVA with Tukey's post hoc test was used to compare across
1897 groups; **, $p<0.01$. **(G)** GST-FUS (5 μ M) was incubated with TEV protease in the presence or
1898 absence of RNA S1 or 2'OMe-modified RNA S1 analogue (20 μ M) for 0–100min. Fibrillization
1899 was assessed via turbidity. Values represent means \pm SEM ($n=3$). **(H)** Fibrillization reactions
1900 were performed as in (G) for GST-FUS and at the end of the reaction, water, strong inhibitors S1
1901 or S1 analogue (20 μ M) were added to the reaction. Turbidity measurements were taken every
1902 minute to assess the extent of disaggregation. Values represent means \pm SEM ($n=3$).

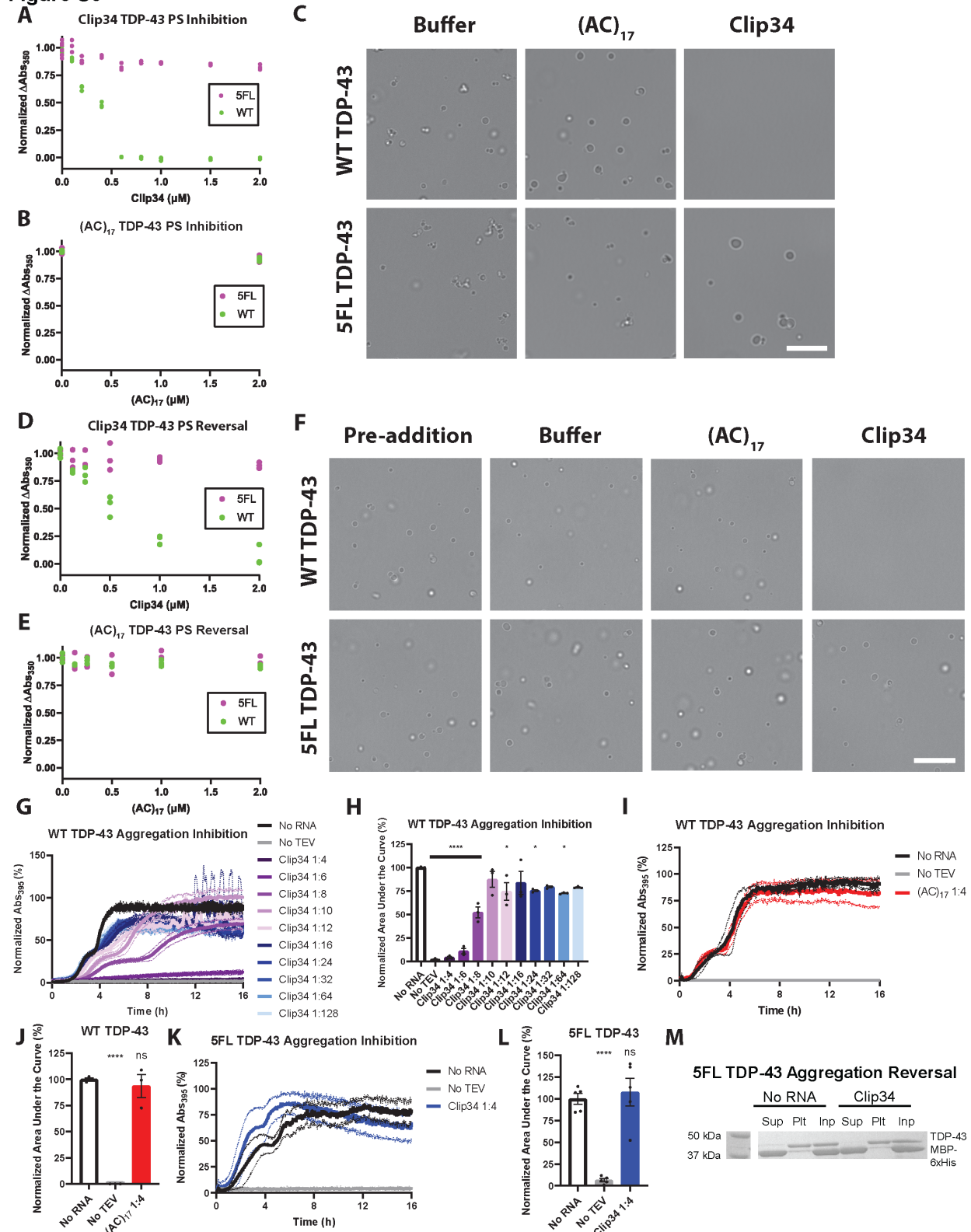
1903

1904 Related to **Figure 5**.

1905

1906

Figure S6



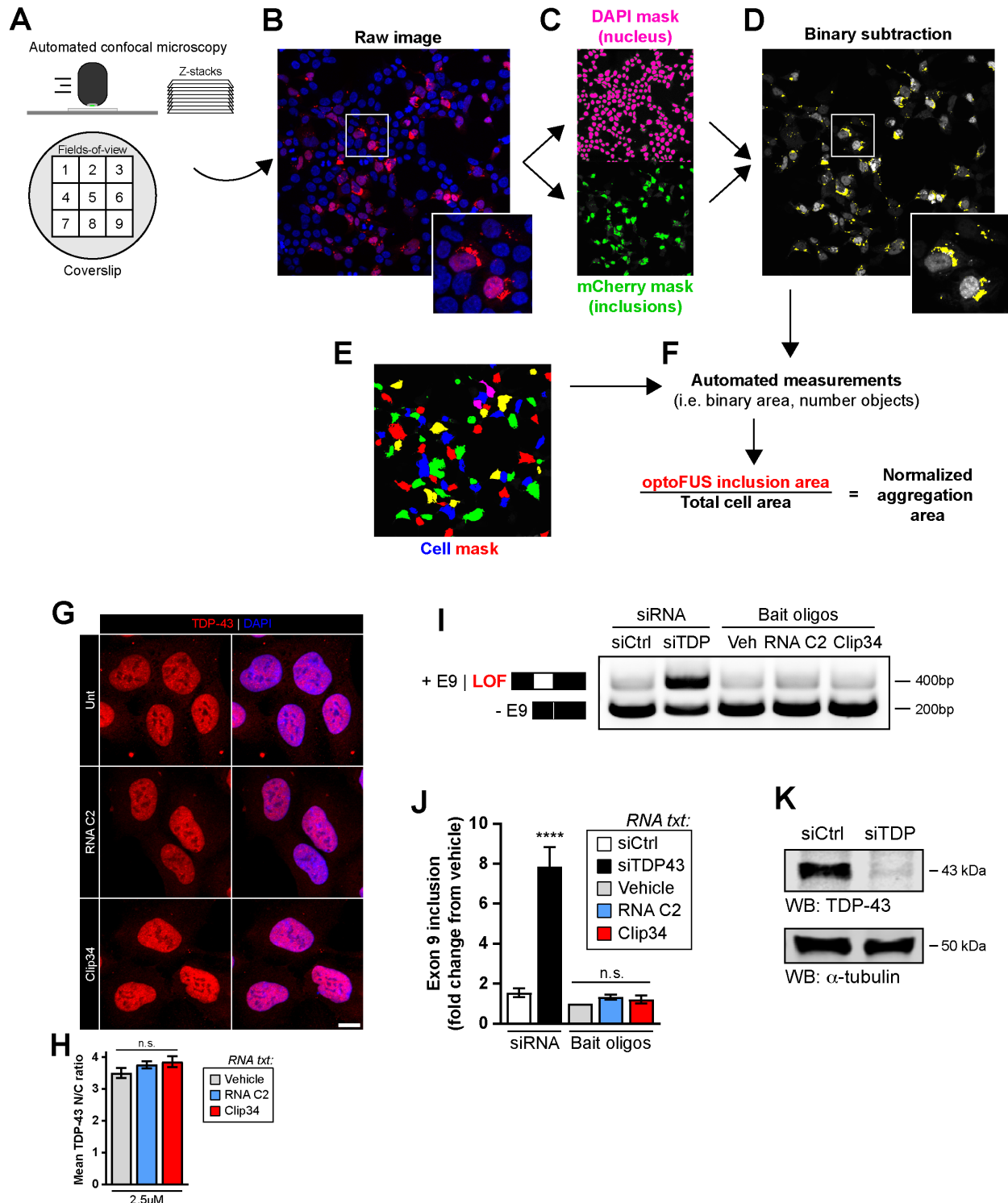
1907
1908
1909
1910

Figure S6. Clip34 directly prevents and reverses aberrant TDP-43 PS. (A, B) TDP-43 or TDP-43^{5FL} (4μM) were incubated with (A) Clip34 (0-2μM) or (B) (AC)₁₇ (0-2μM) for 2h and PS was assessed via turbidity. Individual data points for 3-6 independent trials are plotted for each

1911 RNA concentration. (C) TDP-43 or TDP-43^{5FL} (4 μ M) were incubated with buffer, (AC)₁₇ or
1912 Clip34 (2 μ M) for 2h and PS was assessed via brightfield microscopy. Bar, 10 μ m. (D, E)
1913 Preformed TDP-43 or TDP-43^{5FL} (4 μ M) condensates were incubated with (C) Clip34 (0-2 μ M)
1914 or (D) (AC)₁₇ (0-2 μ M) for 1h and condensate integrity was assessed via turbidity. Individual data
1915 points for 3 independent trials are plotted for each RNA concentration. (F) Preformed TDP-43 or
1916 TDP-43^{5FL} condensates (4 μ M) were incubated with buffer, (AC)₁₇ or Clip34 (2 μ M) for 1h and
1917 condensate integrity was assessed via brightfield microscopy. Bar, 10 μ m. (G) TDP-43 (5 μ M)
1918 was incubated in the presence of the indicated Clip34 concentration as molar ratio RNA:TDP-43.
1919 No TEV protease serves as a negative control. Fibrillization was tracked by turbidity. Values
1920 represent means. Dotted lines of corresponding colors represent \pm SEM (n=3). (H) Area under the
1921 curve data for each replicate quantifies the extent of TDP-43 aggregation in the presence of
1922 Clip34, normalized to the no RNA condition. Values represent means \pm SEM (n=3). One-way
1923 ANOVA comparing to the No RNA condition; Dunnett's multiple comparisons test; ns: p>0.05,
1924 *p adjusted \leq 0.05, and ****p \leq 0.0001. (I) TDP-43 (5 μ M) was incubated in the presence of the
1925 indicated (AC)₁₇ concentration as molar ratio RNA:TDP-43. No TEV protease serves as a
1926 negative control. Fibrillization was tracked by turbidity. Values represent means. Dotted lines of
1927 corresponding colors represent \pm SEM (n=3). (J) Area under the curve data for each replicate
1928 summarized in (I) quantifies the extent of TDP-43 aggregation. Values represent means \pm SEM
1929 (n=3). One-way ANOVA comparing to the No RNA condition; Dunnett's multiple comparisons
1930 test; ns: p>0.05, *p adjusted \leq 0.05, and ****p \leq 0.0001. (K) TDP-43^{5FL} (5 μ M) was incubated in
1931 the presence of the indicated Clip34 concentration as molar ratio RNA:TDP-43. No TEV
1932 protease serves as a negative control. Fibrillization was tracked by turbidity. Values represent
1933 means. Dotted lines of corresponding colors represent \pm SEM (n=5). (L) Area under the curve
1934 data for each replicate summarized in (K) quantifies the extent of TDP-43 aggregation. Values
1935 represent means \pm SEM (n=5). One-way ANOVA comparing to the No RNA condition; Dunnett's
1936 multiple comparisons test; ns: p>0.05, *p adjusted \leq 0.05, and ****p \leq 0.0001. (M) Preformed
1937 TDP-43^{5FL} aggregates (4 μ M) were incubated with buffer or Clip34 (40 μ M) for 16h. Reactions
1938 were processed for sedimentation analysis and the supernatant fraction, pellet fraction, and input
1939 (100%) were fractionated by SDS-PAGE and Coomassie stain. Note that Clip34 is unable to
1940 return TDP-43^{5FL} to the supernatant fraction.

1941
1942 Related to **Figure 7**.

1943



1944
1945
1946
1947
1948
1949

Figure S7. Clip34 does not affect endogenous TDP-43 localization and splicing function.

(A-F) Automatic aggregation analysis workflow. (G) HEK293 cells were left untreated (Unt) or treated with 2.5 μM of the indicated oligonucleotides (RNA C2 or Clip34) for 24h prior to immunofluorescence analysis of endogenous TDP-43 localization. Bar, 10 μm. (H) Mean nuclear/cytoplasmic ratios of TDP-43 fluorescence intensity in cells treated with the indicated

1950 oligonucleotides. Values represent means±SEM. $n=25-39$ cells per group. One-way ANOVA
1951 with Tukey's post-hoc test. **(I)** A CFTR minigene assay was used to assess endogenous TDP-43
1952 splicing function in cells treated with the indicated siRNA (25nM) or RNA oligonucleotides
1953 (2.5µM) for 72h. Top bands indicate loss of TDP-43 splicing function (exon 9 inclusion). TDP-
1954 43 knockdown (siTDP43) was used as a positive control in these assays. **(J)** Quantification of (I).
1955 Values represent means±SEM ($n=2-3$). One-way ANOVA with Tukey's post-hoc test;
1956 **** $p \leq 0.0001$. **(K)** Western blot analysis of HEK293 cells treated with 25nM of non-targeting
1957 (siCtrl) or TDP-43-targeting (siTDP) siRNA to confirm efficient TDP-43 knockdown at the time
1958 points of these experiments.

1959
1960 Related to **Figure 7**.

1961

1962

1963 **Table S1. Motif analysis by Homer shows enriched sequence motifs in the FUS-binding**
 1964 **RNA library.**

Rank	Motif	P-value
1		1e-259
2		1e-209
3		1e-176
4		1e-152
5		1e-149
6		1e-149
7		1e-141
8		1e-122
9		1e-121
10		1e-117
11		1e-115
12		1e-107
13		1e-97

14		1e-89
15		1e-88
16		1e-86
17		1e-85
18		1e-85
19		1e-79
20		1e-79
21		1e-77
22		1e-77
23		1e-76
24		1e-68
25		1e-64
26		1e-59

27	ATTGACGCTC <small>A_{Ac}CGCTC</small>	1e-53
28	CGCTAGCTTC <small>CTTCTAGCTTC</small>	1e-46
29	CAAGATATTC <small>CAAGATATTC</small>	1e-44
30	TAATGCGTAA <small>TAATGCGTAA</small>	1e-40
31	TGAATTATCC	1e-40
32	TCGAACAG <small>TCGAACAG</small>	1e-32
33	CACGATAC <small>GCACGATAC</small>	1e-25
34	GACGCGTC <small>GACGCGTC</small>	1e-19
35	TTGTACAA <small>TTGTACAA</small>	1e-19

36	AACCTTCGTA <small>A A C C T T C G T A</small>	1e-15
37	CGCTGGCATCCA <small>C G C T G G C A T C C C A</small>	1e-14
38	AAAGCGGCGATG <small>A A A G C G G C G A T G</small>	1e-14
39	TATTGATCCGGT <small>T A T T G A T C C G G T</small>	1e-13
40	CTAAGAGTAC <small>C T A A G A G T A C</small>	1e-13
41	TCTGATCGTTGG <small>T C T G A T C G T T G G</small>	1e-12
42	AGCAGGGGCGAC <small>A G C A G G G G C G A C</small>	1e-12

1967
1968

1969 **Table S2: List of RNAs used in this study divided into strong inhibitors, weak inhibitors,**
 1970 **and RNAs with no activity.** Known FUS-binding motifs are highlighted as following: GGUG
 1971 motifs are bolded and marked by underline and GGU motifs are highlighted in red color.
 1972 Secondary structure of the RNA is predicted using M-fold⁸¹. Lowest free energy secondary
 1973 structure of each RNA is shown.
 1974

RNA oligo	Sequence	Length (nts)	Reference	Predicted secondary structure
S1	C.U.A.G.G.A.U.G.G.A. <u>G.G.U.G</u> .G.G.G. A.A.U. <u>G.G.U</u> .A.C	25	In the 3'UTR of the BDNF gene ²⁶	
S2	G.A. <u>G.G.U.G</u> .G.C.U.A.U.G.G.A. <u>G.G.U</u> . <u>G</u> .G.C.U.A.U.G.G.A. <u>G.G.U.G</u> .G.C.U.A. U.G.G.A. <u>G.G.U.G</u> .G.C.U.A.U.G	48	This paper (4 repeats of motif No. 9)	

S3	<p>A.U.U.G.A.G.G.A.G.C.A.G.C.A.G.A.G.A .A.G.U.U.G.G.A.G.U.G.A.A.G.G.C.A.G. A.G.A.G.G.G.G.U.U.A.A.G.G</p>	48	PrD RNA from DNMT3b ²⁷	
S4	<p>A.C.C.A.U.G.A.U.C.A.C.G.A.A.G.G.U.G .G.U.U.U.U.C.C.C.A.G.G.G.C.G.A.G.G. C.U.U.A.</p>	39	snRNA U1 ²⁸	
S5	<p>C.U.C.C.G.G.A.U.G.U.G.C.U.G.A.C.C.C. C.U.G.C.G.A.U.U.U.C.C.C.C.A.A.A.U.G. U.G.G.G.A.A.A.</p>	43	snRNA U1 ²⁸	

S6	<p>A.A.A.A.A.A.A.A.A.A.A.A.A.A.A.A.A.A. A.A.A.A.A.A.A.A.G.U.G.A.A.G.G.C.A.G .A.G.A.G.G.G.G.U.U.A.A.G.G</p>	48	3'-PrD RNA from DNMT3b ²⁷	
S7	<p>G.A.C.U.G.A.A.A.A.A.A.G.G.U.G.G.G.U. U.U.C.U.U.U.U</p>	24	BDNF ²⁶	
S8	<p>A.U.U.G.A.G.G.A.G.C.A.G.C.A.G.A.G.A. .A.G.U.U.G.G.A.A.A.A.A.A.A.A.A.A.A.A. A.A.A.A.A.A.A.A.A.A.A.A.A.A.</p>	48	5'-PrD RNA from DNMT3b ²⁷	

<p>W1</p>	<p>U.C.A.G.A.G.A.C.A.U.C.A.U.C.A.G.A.G .A.C.A.U.C.A</p>	<p>24</p>	<p>This paper (2 repeats of motif No. 1)</p>	
<p>W2</p>	<p>G.A.A.A.A.U.U.A.A.U.G.U.G.U.G.U.G. U.G.U.G.G.A.A.A.A.U.U</p>	<p>28</p>	<p>(UG)₆ RNA²⁵</p>	

W3	U.U.G.U.A.U.U.U.U.G.A.G.C.U.A.G.U.U .U. G.G.U.G .A.U	25	GGUG motif RNA ²⁴	
W4	G.G.U.G .A.G.C.A.C.A.G.A. G.G.U.G .A. G.C.A.C.A.G.A	24	This paper (2 repeats of motif No. 2)	
W5	C.C.A.A.U.C.U.U.C.C.U.U.C.C.A.A.U.C. U.U.C.C.U.U	24	This paper (2 repeats of motif No. 3)	

W6	G.A.U.G.G.A.U.U.C.C.A.G.G.A.U.G.G.A. .U.U.C.C.A.G	24	This paper (2 repeats of motif No. 6)	
W7	A.A.A.C.G.G.U.C.U.G.A.U.A.A.A.C.G.G. .U.C.U.G.A.U	24	This paper (2 repeats of motif No. 7)	
W8	A.A.A.G.C.G.G.C.G.A.U.G.A.A.A.G.C.G. .G.C.G.A.U.G.	24	This paper (2 repeats of motif No. 38)	

W9	U.A.U.U.G.A.U.C.C. G.G.U .U.A.U.U.G.A. .U.C.C. G.G.U .	24	This paper (2 repeats of motif No. 39)	
S2/2	G.A. G.G.U . G .G.C.U.A.U.G.G.A. G.G.U . G .G.C.U.A.U.G.	24	This paper (2 repeats of motif No. 9)	
S2/2 (A-U)	G.U. G.G.U . G .G.C.U.A.U.G.G.A. G.G.U . G .G.C.U.A.U.G.	24	This paper	

<p>W1*2</p>	<p>U.C.A.G.A.G.A.C.A.U.C.A.U.C.A.G.A.G .A.C.A.U.C.A.U.C.A.G.A.G.A.C.A.U.C. A.U.C.A.G.A.G.A.C.A.U.C.A</p>	<p>48</p>	<p>This paper (4 repeats of motif No. 1)</p>	
<p>N1</p>	<p>C.G.C.U.G.G.C.A.U.C.C.A.C.G.C.U.G.G. C.A.U.C.C.A.</p>	<p>24</p>	<p>This paper (2 repeats of motif No. 37)</p>	

N2	A.C.A.G.U.C.C.C.C.C.G.G.A.C.A.G.U.C. C.C.C.C.G.G	24	This paper (2 repeats of motif No. 4)	
N3	A.C.C.G.G.C.G.A.A.C.C.G.G.C.G.A.A.C. C.G.G.C.G.A	24	This paper (2 repeats of motif No. 13)	
N4	C.A.G.U.A.U.U.A.U.U.U.U.C.A.G.U.A.U. .U.A.U.U.U.U	24	This paper (2 repeats of motif No. 15)	

<p>N5</p>	<p>C.C.A.U.C.C.A.G.U.C.U.A.C.C.A.U.C.C. A.G.U.C.U.A.</p>	<p>24</p>	<p>This paper (2 repeats of motif No. 5)</p>	
<p>N6</p>	<p>C.C.A.G.U.C.U.G.G.C.C.C.C.C.A.G.U.C. U.G.G.C.C.C.</p>	<p>24</p>	<p>This paper (2 repeats of motif No. 8)</p>	

Control	U.G.U.A.U.U.U.U.G.A.G.C.U.A.G.U.U.U .G.C.U.G.A.U.	24	C2 RNA ²⁴	
U50	U.U.U.U.U.U.U.U.U.U.U.U.U.U.U.U.U. U.U.U.U.U.U.U.U.U.U.U.U.U.U.U.U.U. U.U.U.U.U.U.U.U.U.U.U.U.U.U.U.U.U.	50	Niaki et al. ³¹	No structure
(AC) ₁₇	A.C.A.C.A.C.A.C.A.C.A.C.A.C.A.C.A.C. A.C.A.C.A.C.A.C.A.C.A.C.A.C.A.C.A.C.	34	This paper	No structure
Clip34	G.A.G.A.G.A.G.C.G.C.G.U.G.C.A.G.A.G .A.C.U.U. G.G.U.G .G.U.G.C.A.U.A.A	34	TDPBP ⁵⁶	
2'OMe - modified RNA S1	mC.mU.mA.mG.mG.mA.mU.mG.mG.mA .mG.mG.mU.mG.mG.mG.mG.mA.mA.m U.mG.mG.mU.mA.mC	24	This paper	
Fl-S1	Fluorescein- C.U.A.G.G.A.U.G.G.A. G.G.U.G .G.G.G. A.A.U. G.G.U.A.C	25	This paper	
Fl-S2	Fluorescein- G.A. G.G.U.G .G.C.U.A.U.G.G.A. G.G.U. G.G.C.U.A.U.G.G.A.G.G.U.G .G.C.U.A. U.G.G.A. G.G.U.G .G.C.U.A.U.G	48	This paper	
Fl-S3	Fluorescein- A.U.U.G.A.G.G.A.G.C.A.G.C.A.G.A.G.A .A.G.U.U.G.G.A.G.U.G.A.A.G.G.C.A.G. A.G.A.G.G. G.G.U.U.A.A.G.G	48	This paper	
Fl-W1	Fluorescein- U.C.A.G.A.G.A.C.A.U.C.A.U.C.A.G.A.G .A.C.A.U.C.A	24	This paper	

1975 **Movie S1. RNA C2 has no effect on FUS droplets.** Preformed GST-FUS droplets (10 μ M
1976 monomer) were spotted onto a coverslip. Movie was taken by DIC microscopy immediately after
1977 RNA C2 (40 μ M) was added to the sample. Bar, 10 μ m.
1978

1979 **Movie S2. RNA S1 dissolves FUS droplets.** Preformed GST-FUS droplets (10 μ M monomer)
1980 were spotted onto a coverslip. Movie was taken by DIC microscopy immediately after RNA S1
1981 (40 μ M) was added to the sample to monitor dissolution of the droplets. Bar, 10 μ m.
1982

1983 **Movie S3. RNA S2 dissolves FUS droplets.** Preformed GST-FUS droplets (10 μ M monomer)
1984 were spotted onto a coverslip. Movie was taken by DIC microscopy immediately after RNA S2
1985 (40 μ M) was added to the sample to monitor dissolution of the droplets. Bar, 10 μ m.
1986

1987 **Movie S4. RNA S3 dissolves FUS droplets.** Preformed GST-FUS droplets (10 μ M monomer)
1988 were spotted onto a coverslip. Movie was taken by DIC microscopy immediately after RNA S3
1989 (40 μ M) was added to the sample to monitor dissolution of the droplets. Bar, 10 μ m.
1990
1991